THERMOREFLECTANCE FOR CONTACTLESS SINTERING CHARACTERIZATION: FROM METAL NANOPARTICLES TO STRETCHABLE CONDUCTORS

MD SAIFUR RAHMAN

A THESIS SUBMITTED TO

THE FACULTY OF GRADUATE STUDIES

IN PARTIAL FULFILLMENT OF THE REQUIREMENTS

FOR THE DEGREE OF

MASTER OF APPLIED SCIENCE

GRADUATE PROGRAM IN

ELECTRICAL ENGINEERING AND COMPUTER SCIENCE

YORK UNIVERSITY, TORONTO, ONTARIO

JUNE 2020

Abstract

Sintering metal nanoparticles is a crucial step to achieve printed conductors. It is important to characterize and monitor nanoparticle sintering for process optimization and control. Here, we demonstrate that frequency-domain thermoreflectance (FDTR), an optical pump-probe technique, can be used for non-contact, non-destructive process monitoring that is compatible with high-throughput printed electronics manufacturing, unlike traditional electrical resistance measurements. The thermal conductivity measured from FDTR agrees well with thermal conductivity calculated using Wiedemann-Franz law from electrical conductivity measurements. Measurement time is reduced to 12 s by choosing a small number of measurement frequencies instead of a full frequency sweep and measuring them simultaneously. A Monte Carlo simulation was performed to predict the possibility of further reducing measurement time. Understanding of the sintering process allows tailoring of materials properties as demonstrated here to create a novel stretchable conductor. Differently sintered layers are combined to achieve a desirable stretchability-conductivity profile.

Acknowledgments

I was lucky enough to meet a great number of amazing people during my Masters. All of their help, whether explicitly or implicitly, propelled me towards the end of my degree. I would have written here about all the help I received and express gratitude to each person individually if space here was not limited.

First and foremost, I would like to express my gratitude and wholehearted thanks to my supervisor, Professor Gerd Grau, for his continued support in each aspect of my graduate life. The works done for this thesis is a testament to the kind guidance I received from him. I have experienced the freedom to explore a bunch of newer ideas while having an expert opinion when needed. I want to offer my gratitude to Dr. Simone Pisana, a great mentor, and an excellent collaborator, who was also in my thesis supervisory committee. In this note, I want to thank his students, Mizanur, Reza, and Shanny, for their relentless help in making the FDTR project work. My kind gratitude is for Dr. Sunny Leung and his students for providing access and training on the machines of his lab.

Lab technologists, Md Amin Haque Talukder, Giancarlo Ayala-Charca, David Marcinkiewicz from both Electrical Engineering and Computer Science and Mechanical Engineering department, were helpful to me. I want to thank them. I also want to thank Magdalena Jaklewicz for her help with the beautiful SEM images. Another friendly face, Shane Guo in the SPARC cleanroom facility, regularly aided with the tools.

I thank my labmates for making the lab environment friendly and enjoyable. Especial thanks to Mohamad Kannan, Paria Naderi, and Fahmida Pervin, with whom I engaged in thoughtful discussion and planning with several experimental and practical problems.

Finally, I am grateful to my family members for supporting me and help me to keep me focused on my goals. Especial thanks to my sisters for their continuous suggestions to support me for these years. Lastly, but most importantly, I want to express gratitude toward my fiancée Saniya. Her constant encouragement, regardless of my failed attempt to my experiments, helped me to keep things in perspective. Her witty puns and comments certainly helped me to stay out of the inevitable grind of graduate life.

Table of Contents

List of figures

1. Introduction

1.1. Printing Electronics

Printed electronics, as the name suggests, is the printing of electronic devices and systems using conventional printing technology as the method of fabrication. The primary goal for printed electronics is to have an on-demand, high-throughput, and additive, hence, material-conservative fabrication paradigm for large-area, low-cost and flexible electronics. Such applications include solar cells, displays, RFID antennas, sensor networks, and wearable healthcare [1]–[3]. Figure 1-1 depicts some applications that are suitable for printed electronics. Another feature that makes printed electronics interesting is that the functionality of the device can be independent of the substrate underneath. This property enables the usage of cheap, flexible, lightweight materials such as paper [4], plastic [2] to be used as substrates.

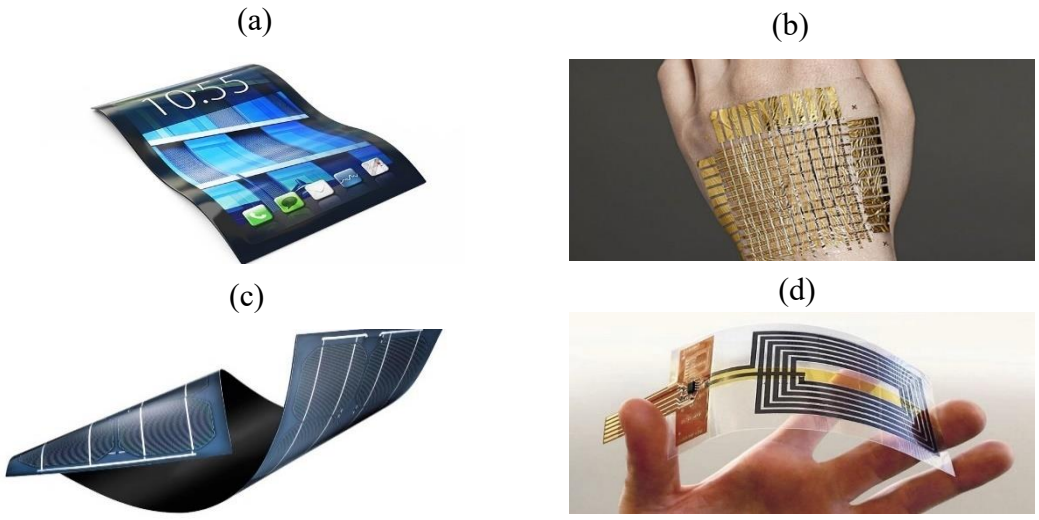

Figure 1-1: Some large-area applications that can benefit from the advantages of printed electronics. (a) Flexible display (www.printedelectronicsnow.com), (b) skin sensor network (www.thenakedscientist.com), (c) flexible solar cell (www.pv-magazine.com), (d) RFID tags (www.medium.com)

Printed technologies have always been used in the graphics arts industry and printing on paper media for large production throughput from the period of the early industrial revolution. Breakthroughs in organic electronics, such as the development of organic conductors and semiconductors led the scientific community to be interested in using the printing process in the

electronics fabrication industry. One of the most important reasons behind this interest is that organic materials can be formulated as printable inks for solution processing. Later, adopting inorganic nanomaterials (nanoparticles, nanowires, nanotubes, etc.) as ink material provides benefits that are far superior to their organic counterparts. These benefits are low batch-to-batch variability, better environmental stability, and superior electrical properties. For instance, the charge mobility of printed transistors with inorganic semiconducting carbon nanotubes can easily exceed 30 $cm^2V^{-1}s^{-1}$whilst the mobility in organic transistors mobility rarely exceeds 10 $cm^2V^{-1}s^{-1}$ [5]. Ink made from oxide-based doped materials is another forerunner in this regard [6][7]. When it comes to choosing conductors, inorganic metal nano/microparticle ink or paste can be a better choice than organic conductive polymers. The reason is that these metallic inks can provide a much higher electrical conductivity (in the range of 10^7 S/m) than that of organic counterparts (10^5 S/m) [8], [9]. However, the downside of these inks is that post-processing such as sintering is needed to transform these liquid inks into a solid form. Unlike organic materials, post-processing of the deposited inorganic nano/micro materials is a crucial step. This step has not only a significant impact on achieving suitable electrical properties, but it also has an essential effect on manufacturing throughput. A faster heating mechanism other than traditional thermal heating can induce the sintering process in a shorter time; hence, the processing time is decreased with higher throughput. Additionally, investigating newer sintering modes and conditions can introduce the ability to use cheap and day-to-day plastic as a substrate. Notably, different sintering modes with selective heating at a faster rate limit the heat propagation to the plastic substrates and do not damage the substrate as compared to traditional sintering methods.

During process development and manufacturing, monitoring of the sintering process to control the quality of sintered metal ink is crucial. In this dissertation, we propose that laser-based thermoreflectance measurements, an optical and contactless probing technique, can be used to determine thermal conductivity as a method of probing sintering stages. Moreover, thermal conductivity can be directly correlated to electrical conductivity values with Wiedemann-Franz law. Thermal conductivity is also an essential property of printed nanoparticle films in its own right. Knowing the change of thermal conductivity as sintering progresses is vital for modeling and optimizing the sintering conditions, especially for novel high-rate alternative sintering techniques such as laser [10] and intense pulsed light (IPL) sintering [11]. It is also critical to know thermal conductivity for applications where overheating can degrade device performance, such as

high-current circuits as well as for thermal devices. Finally, a novel method of fabricating a stretchable conductor is presented by modifying the sintering parameters as a technology demonstration of this thesis.

The choice of printing methods for this thesis is discussed by comparing the advantages and disadvantages of different printing methods in the following section. The physics of sintering and the current trend of sintering methods that are applicable for printed electronics are described in the next section. An overview of the state-of-the-art of non-contact evaluation of sintering stages is presented in the following section. Finally, an overview of the thesis is given.

1.2. Printing Techniques: Overview and Comparison

Many different printing techniques have been proposed for realizing printed electronics. While most of them offer low-cost and large-area electronics when compared to traditional vacuum-processed electronics, each printing technique has its own advantages and disadvantages that are worthy of discussion. One broad parameter that is used to categorize the printing techniques is the usage of a mask/template. The mask-less printing techniques are often called digital printing methods as they offer the advantage of changing the pattern on the fly. In general, the pattern to be printed via these methods is digitally stored in a computer, for example, as relative coordinate points. A nozzle follows the predetermined pattern, moves relative to the substrate, and jets/extrudes materials in the desired locations. Such printing techniques include inkjet printing, extrusion printing, and aerosol jet printing. Printing that depends on a template is known as non-digital printing. Screen printing, flexography, offset, and gravure are prominent examples of such printing methods. The details of such printing might vary from printer to printer, but the principle stays the same: a pattern or stencil is in contact with the substrate while delivering the patterned ink onto the substrate.

1.2.1. Template-Based Printing

These methods are traditionally used in graphics printing on paper, where a roll is used to generate patterned materials via a hard stencil or recessed/raised cells on the roll. In general, template or contact-based printing offers superior fidelity due to no involvement of jetting from a nozzle. These methods show a great promise in fabricating electronic thin-films at an extremely high throughput [12]. Here, manufacturing throughput (in $m^2\ s^{-1}$) is the product of web width and

printing speed. These manufacturing methods work with a roll that facilitates a large web width several meters wide and have high printing speed.[13]. Screen printing is one example of template-based printing, in which ink is pushed through a screen of woven material (for example, steel mesh) onto the substrate with a squeegee. The mesh holds a stencil that defines the pattern. Dimensional scaling with screen printing is problematic. If one wants to have a smaller feature size, a smaller opening on the mesh is required. This substantially limits the usage of high viscosity inks, which is needed for good pattern definition in screen printing [14]. Flexography, gravure, and offset printing all use a patterned inked roll (created either through mechanical processes or surface modification) to deliver ink material to the substrate. Flexography uses a roll with elevated features that are inked from an anilox roller. Conversely, the gravure printer's roll consists of individual engraved cells, pixelating the original pattern. In this case, these cells are loaded with the ink material, which is then transferred to the substrate. In offset, the roller has both the pattern and non-patterned area in the same plane, and patterning is done through the difference in surface energy. In general, a tight window of ink viscosity, albeit more flexible than inkjet printing (discussed in the next section), works with these roll-to-roll methods, resulting in restrictions in material selection and ink formulation. Additionally, each time a new design is adopted, a unique mask must be made. Because of the high cost of making the mask, these methods are not suitable for small batch production.

1.2.2. Digital Printing Methods

In contrast to template-based printing, digital printing methods use an electronic design file of the pattern. As these files can easily be altered, the pattern can be varied more flexibly than in template-based printing. **Error! Reference source not found.** depicts illustrations of three p rominent digital printing methods, inkjet, aerosol jet, and extrusion printing. Inkjet printing is one of the well-known printing methods with reasonable throughput and resolution. It refers to a printing method in which individual droplets are controlled to jet out through a nozzle. The print-head ejects in a drop-on-demand manner. Drop propelling is done via a piezoelectric transducer creating pressure to eject a droplet from the nozzle. The nozzle is then moved relative to the substrate to write a pattern. Proper jetting depends on the rheological properties of the designed ink. Research has focused on ink designing to remove any non-idealities such as suppressing satellite droplet formation and nozzle clogging due to solvent evaporation [15]–[17]. Upon

impinging on the substrate, these droplets spread on the substrate due to a combination of drop momentum and flow caused by surface tension [18]. Depending on the spacing between deposited droplets, substrate wettability, substrate temperature, and drop placement strategy, complex shapes with optimal printed morphology can be achieved [19]. A large number of nozzles can be used in unison, covering a large area of the web at once to obtain good throughput. Inkjet printing has the advantage of superior control over the droplet volume and density and accurate spatial positioning.

Conversely, aerosol jet printing has less control over the jetting volume and positioning because of the random nature of the high speed atomized liquid droplets, i.e., the aerosol. These aerosols, being created pneumatically or ultrasonically, are carried via an air stream to a nozzle that creates aerodynamically focused jetting. Less accurate positioning of aerosols leads to a phenomenon known as "ink overspray" [20]. The workable ink viscosity window is typically large (0.7-2500 mPa.s) for this printing method, a much bigger range than inkjet printable inks (5-30 mPa.s) [21]. The lateral resolution of printed lines is much finer with aerosol jet printing (~ 10 μm) compared to inkjet printing (≥ 20 μm) [22][23]. The primary limitations with downscaling feature resolution with inkjet are clogging in small nozzle orifices and drop placement accuracy [24]. Aerosol jet requires costly printing apparatus with a complicated ink tuning process [25].

Extrusion printing, also known as direct writing, is a promising digital printing method for printed electronics. This method combines the advantages of inkjet printing and screen printing. Pressurized ink is continuously delivered through a scanned nozzle to the substrate. It also has the ability to change the pattern on the fly with considerable flexibility in ink material, be it viscosity (100 - $3x10^5$ mPa.s) or compositional flexibility [26]. With extrusion printing, depending on the nozzle orifices' diameter, the printed feature's resolution can be as low as 2 μm [27], although it is typically much larger on the order of 100 μm. Despite having a relatively low throughput compared to the roll-to-roll based printing methods, the digital printing methods are very efficient in a small batch or research prototype production. Among these methods, inkjet and extrusion printing stand out because of their low-cost and matured techniques with a plethora of commercially available inks. In this thesis, they are used extensively for fabrication purposes.

After printing, post-processing steps such as drying, and sintering are crucial and have significant effects on the quality of the finished products. Moreover, adopting alternative sintering methods, such as electromagnetic waves rather than heat, allows sintering time to be reduced. The next

section is dedicated to sintering mechanisms in different printable inks, followed by a discussion on viable alternative sintering techniques.

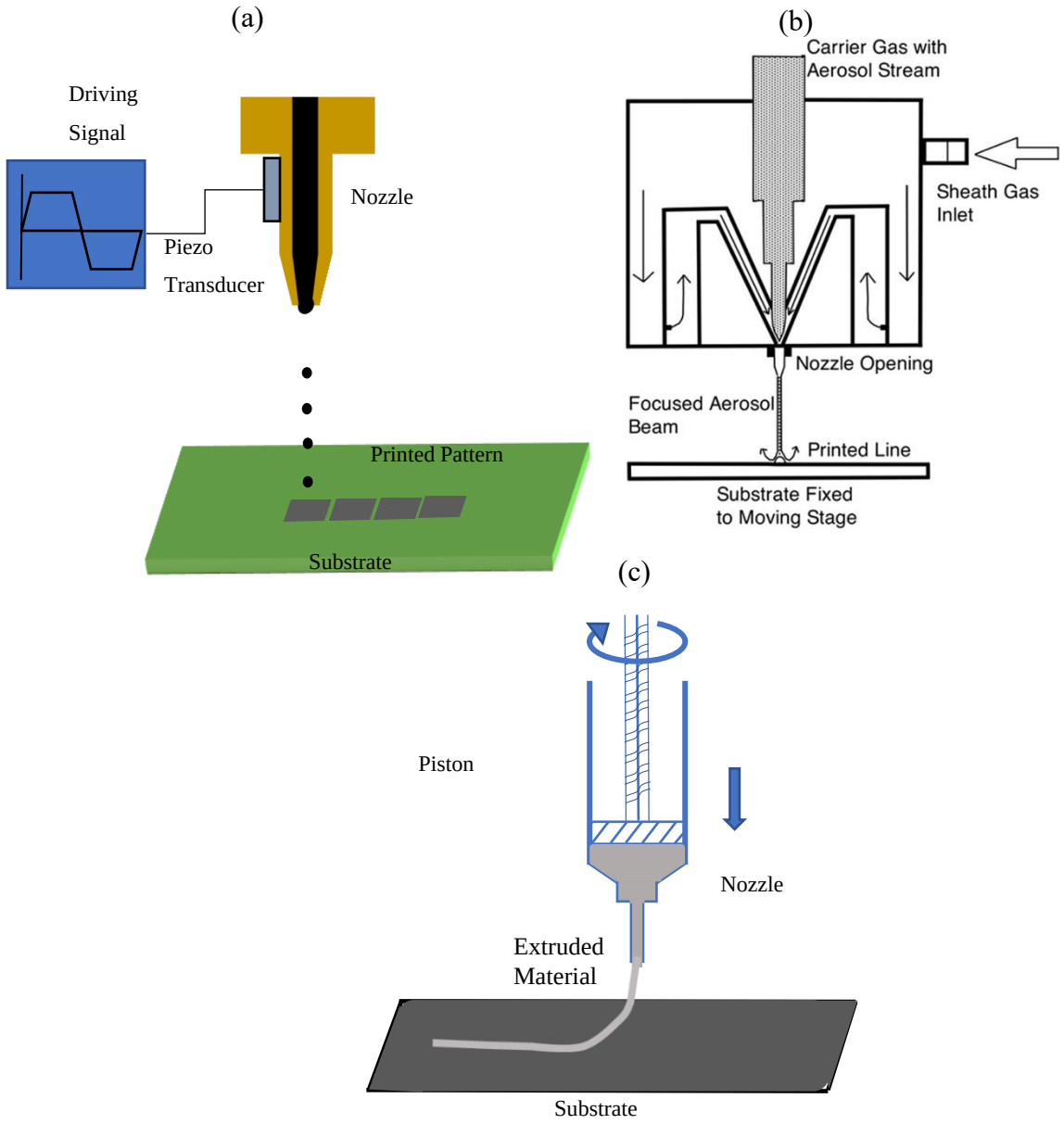

Figure 1-2: Examples of digital printing methods. (a) Inkjet printing, a periodic electronic signal deforms a piezo transducer to jet ink through a nozzle. (b) Aerosol jet printing, an atomizer creates aerosols which are focused aerodynamically via a sheath gas flow. Reprinted with permission from ([20]). Copyright (2013) American Chemical Society (c) Extrusion printing, a piston controlled via a software-driven-screw pushes out viscous ink.

1.3. Sintering Metallic Ink for Printed Electronics

Fabricating well-defined and highly electrically conductive metal features on non-ideal substrates such as plastic and paper is a crucial step to realize printed electronic devices. Different kinds of materials have been developed to achieve prolonged shelf life, optimized rheological parameters for printing, desired printed morphology, and low post-processing temperature. The development of fast, efficient, and low-cost post-processing steps such as sintering technologies for these materials are essential for making printed electronics viable for industrial scale. A brief overview of different metallic inks' sintering behavior followed by alternative sintering methods is provided below.

1.3.1. Sintering Mechanism

Sintering is a process by which the printed ink material converts to its solid form and obtains desirable electronic properties. Usually, this process requires heat to be transferred to these materials during the sintering process. To understand the sintering process, understanding the ink composition in liquid form is crucial. There are different ink modalities with their relative advantages and disadvantages. Only the metallic ink types that are suitable for inkjet and extrusion printing, followed by their sintering mechanism, will be discussed.

Metallic inks usually comprise of a noble metal such as gold (Au) [28] or silver (Ag) [9], mainly to avoid long-term oxidation and oxidation during post-processing. Ag is more frequently used because its electrical conductivity is highest among all metals, and it is also cheaper than Au. Currently, copper (Cu) based inks are gaining popularity because of the low-cost raw material [29]. However, as this material is much more prone to oxidation than Ag or Au, post-processing needs to be carefully controlled, such as in a reducing or vacuum environment [29].

Metal precursor inks are one of the prime candidates for printing metallic traces. It is a particle-free ink; thus, no aggregation occurs during storage or printing. They come in two categories, metal-organic decomposition (MOD) ink or metallic salt ink consisting of their respective precursor with a suitable solvent [30]. Metals are present in their respective oxidized form, which is also very stable. Typical metal loading can only reach up to 30%. This is not desirable in high-speed, highly scaled manufacturing processes as multiple runs of printings might be needed to obtain a set thickness of the material. Both of these inks need a specific temperature to be reduced

to its elemental form. For the case of MOD ink, the complex decomposes, and the ligands help these metal cations to reduce to its elemental metal form whilst the ligands oxidize [21]. The displaced ligands are evaporated and leave separated metal NPs as a printed layer. The same train of events occurs for metallic salt inks, except no complex is involved - the salt decomposes to a layer of metal NPs with residues that also leave the printed layer at a very high temperature of 300-500°C [31]. Figure 1-3(a) shows the step-by-step processes of reduction of metal ions to the formation of metal nanoparticles for MOD and metallic salt-based inks. These naked NPs go through a sintering process, which will be discussed after the description of the formulation of direct NP based ink.

Metal nanoparticle-based inks contain metal particles of a size below 100 nm with metal mass loading of 20-70%. The reduced size of nanoparticles is preferential due to its effect on reduced melting point, which, in turn, makes the melting, one stage of the sintering process, easier. However, reduced size nanoparticles tend to agglomerate and cause nozzle clogging and non-ideal printing. To prevent this, these nanoparticles are coated and stabilized with amphiphilic polymers like polyvinylpyrrolidone (PVP) or low molar mass compounds that are anchored to the metal surface with functionalities like amine or thiol [21]. Figure 1-3(b) represents one typical example of a metallic nanoparticle-based ink solution that shows protective ligands surroundings the NPs. These coating agents cause steric or electrostatic repulsion between these dispersed nanoparticles [32]. Compared to the previously discussed MOD and salt ink, the NP ink already has the elemental form of metal. However, these coating agents act as an insulating agent; hence, no conductive pathways for electrons. Temperature close to 200°C can decompose these capping materials to leave the nanoparticles unprotected. Although complete detachment of these materials is desirable for high electrical conductivity, Ingham et al.[33] and Volkman et al.[34] showed that even the disordering of these materials surrounding metal particles, let alone the full detachment, can cause the onset of sintering.

The bare nanoparticles from all these inks go through a series of events to coalesce and form necks with neighboring nanoparticles. This way of crystal growth is named as aggregative growth, which involves two or more crystallites to form an even larger crystallite [35]. Sometimes in literature, the definition of coalescing is limited only to the neck-forming event between two or more particles. Aggregative growth then takes over and controls the growth and orientation of these crystallites [34]. This type of growth leads to multiple domains of materials having different

crystallographic directions. Figure 1-3(c) (i) exhibits such kind of crystal growth. Furthermore, a unique process happens when two nanoparticles with a distinguishable diameter are close to each other. This process is called Ostwald Ripening, in which the larger particles grow even larger at the expense of the smaller diameter particles. The smaller particle's higher surface energy is the primary driver to cause this phenomenon. Ostwald ripening helps them to reach a thermodynamically stable state by minimizing surface energy. It is noticeable that this sintering phenomenon does not rely on complete melting of these particles, rather it is based on surface melting and diffusion of atoms from the smaller particles to the larger particles [21]. With this process of crystal growth, usually, a larger particle emerges with a lower number of grain boundaries. Figure 1-3 (c)(ii) shows the Ostwald ripening process with crystallites having a single domain of crystallographic direction.

Unlike costly metallic nanoparticle inks, metallic flake inks are the ideal candidates for extrusion printing because of its cost-effective compositional chemistry. Unlike nanoparticle ink, usually, mechanical means such as milling are used to create flakes from spherical particles [36], which then become the filler of a polymer matrix for a flake ink. Because of micron-scale flake size, the chance of agglomeration is reasonably low. Therefore, the need for complex chemistry to protect these flakes from agglomeration is also low. However, organic lubricants such as oleic/hexanoic acid are used to cover the flake surface to prevent any agglomeration altogether while dispersing them into a polymeric resin with a suitable solvent [37]. When exposed to heat or other energy sources, the solvent with these organic lubricants is removed. This causes the flakes to be in close contact with each other and forms a percolation pathway for electronic conduction. No surface energy-driven sintering phenomenon happens as a sintering process.

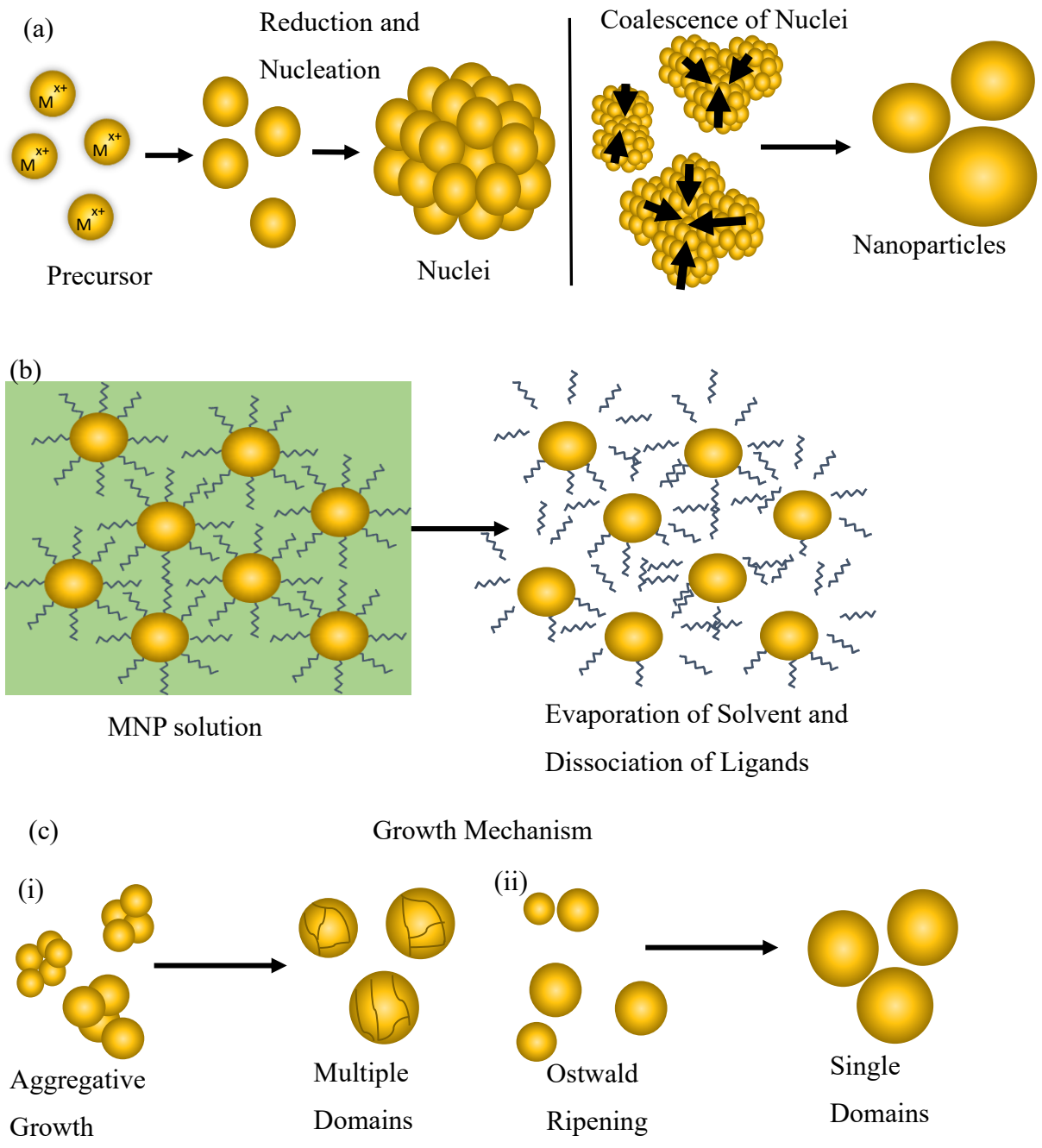

Figure 1-3: Sintering mechanism for different metal ink. (a) MOD or metallic salt-based inks reduce to their elemental form and then nucleate. These nuclei coalesce and form nanoparticles. (b) Metal nanoparticle-based inks already contain nanoparticles, separated by organic ligands. The sintering process starts with the disassociation of ligands, leaving the nanoparticles exposed. (c) (i) The aggregative growth of nanoparticles comes from coalescing of neighboring nanoparticles, often leading to multiple domains. (ii) Ostwald ripening, a surface energy-driven growth through

which bigger particles engulf smaller ones and become even bigger. This growth leads to single domain nanoparticles.

1.3.2. Alternative Sintering Technologies

The most used sintering method is thermal sintering via a hotplate or oven baking. The heat is conducted through the substrate and reaches the intended material that resides on top of the substrate. In printed electronics, the use of cheap plastic substrates is prevalent with the goals of substrate independent electrical performance, flexible, ubiquitous, and low-cost electronics. However, these cheap plastic substrates are mainly polymers with low glass transition temperature, around 150°C or even lower [29]. These polymers fall into the "glassy" state, which is a viscous/rubbery state when the sintering temperature crosses the glass transition temperature. Permanent damage to the structural integrity of the substrate is a very likely event if these plastics remain in the rubbery state for a long time. The printed layer will follow the structural deformations of the underlying substrates, which can cause deteriorated electrical and mechanical properties. If the temperature is kept low not to expose these substrates beyond their glass transition temperature, then the sintering process can take more time and generally results in lower electrical conductivity compared to metals with high-temperature sintering. This compromise between time, performance and protecting the substrate results in the need of long sintering time on the order of many minutes or even hours, which renders the thermal sintering techniques incompatible with high-throughput industrial processes. Alternative sintering technology with fast sintering dynamics and compatibility with low-cost plastic and paper substrates are of high commercial interest. Particularly, sintering techniques that are non-contact in nature require less time for post-processing and selectively heat up the printed materials without heating the substrate are highly sought for commercial purposes [30][38].

1.3.2.1. Plasma Sintering

Plasma Sintering is a process in which as-deposited materials are exposed to an ionized gas stream containing excited ions/neutral for sintering purposes. Mainly, reducing plasma (using hydrogen gas) or inert (e.g., argon gas) plasma is used. The reductive hydrogen plasma forms hydrate with the oxygen and nitrogen of $AgNO_3$ ink, which are released from the printed film, leaving behind an elemental metal layer [39]. The same ink was sintered using an argon plasma where NO_3^-

species are decomposed by the highly energetic argon ion bombardment [40]. In one case, oxidizing plasma (using oxygen as carrier gas) is used to remove the stabilizing PVP polymeric shell of Cu nanoparticles [41]. This removal of PVP can be explained with the chain scission/cleavage where the polymeric backbone is fragmented by active species and is quickly evaporated because of their new lower molar mass [42]. Cu oxide, inherently not conductive, is produced as well due to this kind of plasma exposure. So, a reductive hydrogen plasma was also applied to reduce these oxides to metallic Cu. Plasma sintering causes the onset of sintering by removing the chemical barriers between the particles of the ink. As the particles are bare after plasma exposure, the actual sintering process, i.e., coalescing happens spontaneously, as mentioned in section 1.3.1. Due to no continuous energy delivered to the sample, the thermodynamic drive to induce other particle growth mechanisms is not present except coalescing, giving rise to not-fully sintered layers.

Moreover, the excited species from the plasma can only penetrate and sinter the top few layers of deposited materials and leave the bottom layers unsintered/under-sintered. This effect is known as the skin effect [29]. Therefore, the electrical conductivity of plasma sintered material would be sub-par compared to other sintering mechanisms if measures such as long plasma exposure, two-step plasma are not taken. [29]. Figure 1-4 shows a typical setup for a plasma sintering chamber with the usual “skin effect” in the surface morphology images.

Plasma sintering demonstrates a low-temperature, non-contact method of sintering that is highly applicable for thermosensitive substrates. Due to the need of a low-pressure environment for plasma, using plasma sintering in an R2R processing environment is a challenge. Usually, it takes few seconds for the sintering process; however, to get a homogenously sintered layer, the materials are exposed to the plasma for a longer time so that active species can sufficiently sinter the bottom layers as well. This increased processing time is a hindrance to adopting this sintering technology for commercial purposes.

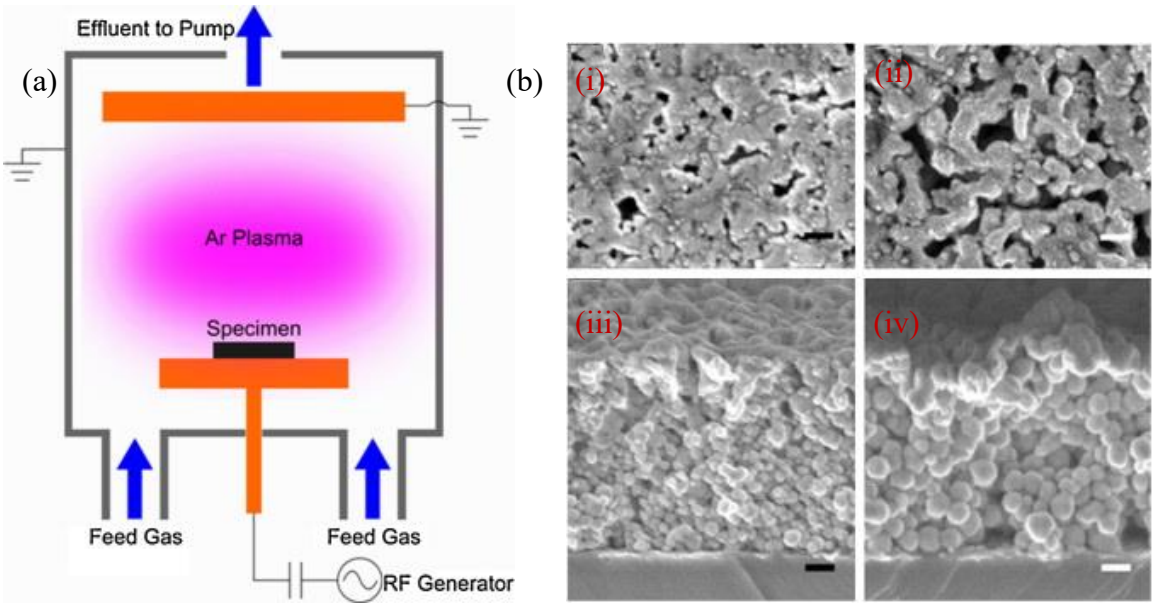

Figure 1-4: (a) A RF plasma sintering setup, argon (Ar) plasma is used; AgNp film rests on an RF-powered electrode. (b) Scanning Electron Microscope (SEM) top and cross-sectional visualization of plasma sintered AgNP films: of 23 and 77 nm AgNP films, (i, ii) top view and (iii, iv) cross-sectional view. It clearly shows the top few layers are more sintered than the bottom layers, demonstrating the skin effect. The scale bars are 100 nm [43]. Copyright © 2014 Elsevier B.V. All rights reserved.

1.3.2.2. Photonic Sintering

Photonic sintering uses an electromagnetic (EM) radiation ranging from ultra-violet (UV) to infra-red (IR) to heat the printed ink selectively using the photothermal effect. This mode of sintering is getting attention due to its promise of only heating the metallic ink and affecting the thermally sensitive substrate as little as possible. One of the apparent prerequisites to achieve such selectivity is to have a significant difference in the optical properties of the metallic ink and the substrate. For the employed EM wavelength range, the deposited ink needs to be very absorptive, whereas the substrates such as polymer foil or glass are to be transparent or reflective in this wavelength range. Conveniently enough, due to the charge transfer kinetics for transitional metal complexes in the MOD inks and having strong plasmon resonance for NP, the visible part of the EM spectrum is absorbed in both cases. This selective absorption can lead to localized heating, only for the printed materials. Figure 1-5 (a) and (c) show the normalized absorption spectra of commonly used substrates and nanomaterials. It is noticeable that, except polyimide, these substrates' absorption

spectra hardly overlap with the metallic nanoparticle spectrum. Depending on the generation of the EM wave and form of radiation, photonic sintering can be divided into four categories: Infrared (IR), ultraviolet (UV), intense pulsed light (IPL), and laser sintering.

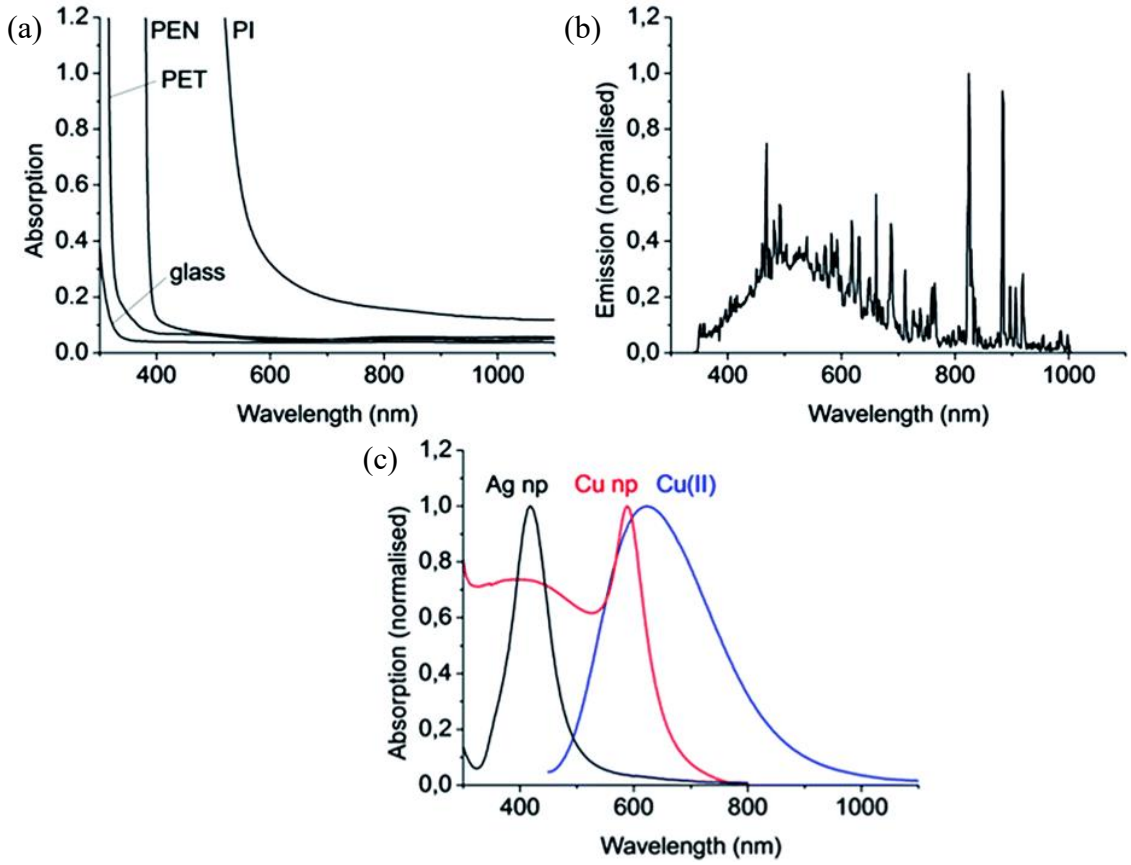

Figure 1-5: (a) Normalised UV-vis absorption spectra of commonly used substrates. (b) The normalized emission spectrum of a Xenon lamp used for intense flashlight sintering. (c) UV-vis absorption spectra of commonly used nanomaterials for printed electronics. Reproduced from Ref. [30] with permission from The Royal Society of Chemistry.

Infrared sintering uses continuous irradiation with an EM wave with a wavelength of 700-15000 nm for sintering purposes. Irradiation with such long-wavelength causes fast heating and raises the substrate (glass and paper) temperature to 180-210°C [44]. This increased temperature in the substrate surface means that heating is not as selective. Instead, it is comparable to thermal heating. Cherrington et al. used near-infrared (NIR) range EM waves to sinter NP to 10% conductivity of the bulk metal while using a commonly used polymeric substrate, polyethylene terephthalate (PET). It is shown that the PET substrate is less susceptible to this irradiation, and hence less

thermal damage to the substrate occurs [45]. However, to achieve better conductivity (more than 10% of bulk), a long time of continuous exposure is needed with the IR lamp. It will eventually damage the substrate. In general, IR sintering is suitable for R2R processing because of its fast sintering process. However, due to high thermal stress, only substrates with high-temperature resistance can be compatible with the process. Using the ultraviolet region of the spectrum (100 nm to 400 nm) for direct sintering of nanoparticles is not commonly used. MOD inks such as Ag neodecanoate, silver(I)-2-[2-(2-methoxyethoxy)ethoxy]acetate etc. show a strong absorption band below 300 nm [29]. This absorption can lead to the formation of nanoparticles, but the rest of the sintering processes can not continue with just UV light sintering. A combination of UV irradiation with chemical and thermal sintering to achieve better electrical conductivity has been reported in the literature [21]. Moreover, traditional conductive inks do not have strong absorption in the UV range. This sintering method is still in its early stages of development.

Conversely, laser sintering technology achieved a great deal of development as a sintering process for metallic inks. This sintering method exploits the properties of the laser, that is, focused light beam and having a desired wavelength matched with the respective absorption of the ink. Here, NP based inks are the primary choice of material for achieving selective heating. It is because the NPs have an intense absorption spectrum that can be matched with the laser's wavelength. NP based inks absorb the laser irradiation in the targeted area, and the photothermal effect causes heating up and eventually sintering due to elevated temperature, well above 200°C [46] [47]. Laser sintering is usually a swift process if the power output, scanning velocity, and absorption spectra of a laser source are optimized and matched according to the material to be sintered. Figure 1-6 shows an illustration of patterning high resolution printed lines with the help of the laser sintering process. Materials with no laser exposure remain unsintered and can be washed with a suitable solvent, leaving a fine sintered line [48]. However, the fast heating process gives rise to the formation of uneven and porous surfaces, a phenomenon due to the fast volume reduction of metallic particles and the fast volatilization of organic materials [21].

Furthermore, Maekawa et al. showed that the matching absorption spectrum could provide a speedy sintering process at the expense of a thick skin conductive layer and less conductive and adhesive bottom layer [49]. They further proposed that using a laser with a wavelength that does not match the metallic ink's absorption wavelength causes a heat generation at the material-substrate interface and creates a smoother grain growth with excellent adhesion. Nevertheless, this

can only be possible if the glass transition temperature is higher than the elevated temperature. Another issue with laser sintering is its employment for large-area sintering and hence, large-area electronics. Though having a small micrometer range spot size is conducive for generating a fine sintered line, for the same reason, the laser needs to be scanned in a large number of passes to cover the intended area [29].

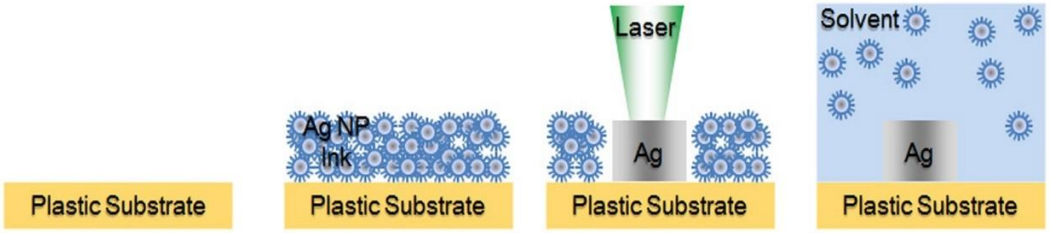

Figure 1-6: High-resolution patterning with selective laser sintering of AgNP on polymer substrates. A solvent removes the residual unsintered ink. Reproduced with permission from the Public Library of Science (PLOS) [48].

Unlike laser sintering, where one wavelength is used, intense pulsed light sintering (IPL) uses the entire visible spectrum to convey heat to the targeted material. Compared to laser, IPL sintering is more energy-efficient, converting 30% of the electrical power to radiation. Figure 1-5 (b) indicates the Xenon lamp's, a typical white light emitter, emission spectrum. The commonly used PET and polyethylene naphthalate (PEN) foils have minimal spectral overlap with the emission of the Xenon lamp, whereas metallic nanoparticles overlap considerably with the lamp emission. However, the generated heat from the photothermal process will reach the substrate, which acts as a heat sink. The duration of irradiation/pulse length (t_{pulse}) needs to be small, to minimize this heat propagation from the material to the substrate. It needs to be much smaller than the time it takes the heat to reach equilibrium (τ_{foil}) between the substrate and ink [30]. In this way, heat will not accumulate, and the substrate-ink interface will cool down after the illumination has ceased. Also, the time for reaching the thermal equilibrium for the ink (τ_{ink}) needs to be smaller than the pulse length. The following equation describes this relation [50]:

$$\tau_{ink} \ll t_{pulse} \ll \tau_{foil} \qquad \text{Eq. 0.1}$$

Here, τ_{ink} and τ_{foil} can be determined via the following equations:

$$\tau_{ink} = \frac{c_{ink} x_{ink}^2 \rho_{ink}}{4k_{ink}} \quad \text{Eq. 0.2}$$

$$\tau_{foil} = \frac{c_{foil} x_{foil}^2 \rho_{foil}}{4k_{foil}} \quad \text{Eq. 0.3}$$

Here, c, ρ, x and k are the specific heat capacities, mass densities, layer thicknesses, and thermal conductivities of each material. Other than pulse duration, different exposing parameters such as pulse shape, frequency, and pulse energy density also need to be considered depending on the ink/substrate combination. This parametric optimization plays a crucial role in final conductivity [30]. For example, if high energy density and high flashing frequency are employed together, often, this results in severe overheating and sample damage. However, increasing the pulse number with the optimized condition, such as mild energy density with low frequency (leads to longer processing time), will be beneficial to the final conductivity with much lower sample damage [38], [51]. Overall, IPL sintering shows some significant advantages over other photonic sintering methods for being able to sinter rapidly, selectively, and process a large area efficiently. Figure 1-7 shows an IPL sintering setup, where the Xenon lamp's light is concentrated through a reflector to sinter the printed materials.

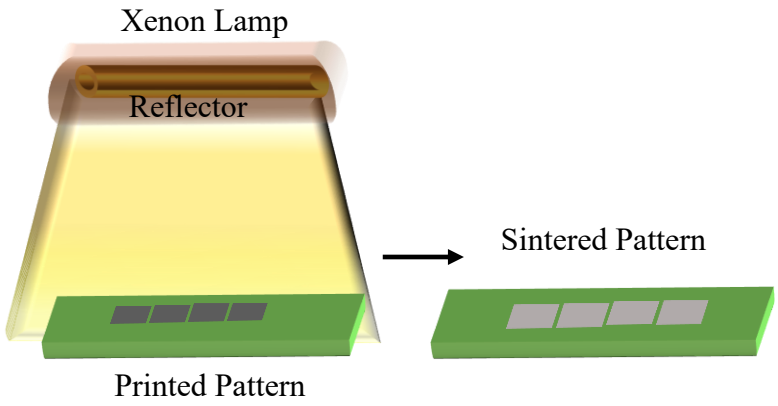

Figure 1-7: An IPL sintering setup with a stroboscopic Xenon lamp and a reflector. The lamp reaches and covers a large area for large-area sintering.

The next section will discuss different methods of monitoring the sintering by measuring changes in the properties of materials that are being sintered and characterize the sintered products for a production line.

1.4. Characterization of Sintered Metal

Different measurement methods can be classified into two categories: contact and non-contact methods. One easy and obvious contact method is to measure electrical conductivity to investigate different stages of sintering [52], [53]. This has the advantage of directly measuring the property that is most important for most printed metal nanoparticle applications. However, it requires dedicated contacts to be fabricated or probes that can scratch the material and takes time to align. Dilatometry is another contact method that determines length or volume as a function of temperature. During the sintering process, dilatometry can sense only one-dimensional length changes because of shrinkage (thickness in the case of thin films). Typically, the length scale of printed metallic traces would be too small for this method, requiring that the material be appropriately prepared for quantification [54]. Overall, contact methods suffer from their destructive nature and complicated setup for an automated production line.

Non-contact evaluation of the sintering process is gaining interest because of its ability to keep the test material intact while monitoring the sintering steps. Additionally, it has the potential for in-line and real-time monitoring. There are numerous non-contact methods for sintering process evaluation for metal additive manufacturing (AM), especially in powder metallurgy. These methods include ultrasonic/acoustic measurement, optical tomography, electromagnetic, and eddy current techniques [55]. Generally, these methods are employed for in-line detection of defects and porosity during/after the sintering. None of these techniques have been applied in the field of printed electronics, which uses different material chemistries, different substrates, smaller particle sizes, thinner films, and smaller feature sizes than powder metallurgy. Recently, millimeter-wave imaging and terahertz (THz) time-domain spectroscopy (TDS) has been used for non-contact characterization in printed electronics utilizing the non-destructive nature of THz radiation. THz imaging has been used to characterize printed ink based on black carbon [56]. This approach was not compatible with high-yield production lines because of its time-consuming nature and complicated data processing for the effective extraction of conductive properties. A simpler and faster method of characterizing with THz TDS was developed by Zhuldybina et al., exploiting the distinctive THz range signal generated by printed V-shaped antennas [57]. Although this is a facile characterization method by monitoring these antennas' transmission, it needs an extra antenna pattern to be printed side by side with the original features of interest. Zenou et al.[58] monitored the changes in spectral reflectivity of a metal nanoparticle ink during sintering as a possible non-

contact method. However, this method can only qualitatively differentiate between the sintered and the non-sintered state. The changes in reflectance between both states are so abrupt that the reflectivity versus resistivity graph could not discern any gradual changes from the non-sintered state to the sintered state. Another optical technique was demonstrated by Cherrington et al. using colorimetry but suffers from scatter in the data [45]. Abbel et al. have demonstrated a method where an embedded temperature probe is used to monitor the temperature rise in a metallic ink during flash sintering [46]. Examining the temperature rise as well as the duration of the temperature exposure, one can indirectly monitor the process; however, this does not generate direct information about the desired changes in material properties during sintering.

In this thesis, we investigate the viability of the frequency-domain thermoreflectance (FDTR) method, a pump-probe laser-based non-contact technique for measuring thermal conductivity, for examining the different phases of sintering. The next section will be dedicated to the background theory and detection principle of this method.

1.4.1. Frequency-Domain Thermoreflectance (FDTR)

There has been significant development in the area of characterizing heat transport due to the significance of the thermal properties of different materials in a variety of applications. Broadly, there are two categories of these characterization techniques. These are steady-state methods and transient methods. In steady-state techniques, thermal properties are measured by establishing a time-independent temperature difference; hence, steady heat flow, on materials. Despite having a relatively straightforward mathematical model for measured data processing, these techniques are mostly used for bulk materials. However, one of these methods, Raman optothermal technique, is promising due to the success of measuring the thermal conductivity of single-layer graphene [59]. This technique is not viable for the typically used metals in printed electronics, i.e., silver, gold, copper, as they do not exhibit any optical phonon and hence no Raman spectral features to detect [60]. Moreover, substrate-induced or interfacial effects on thermal transport are overlooked, as this method requires the sample to be suspended [61]. In the case of transient methods, the studied signals are changing with time due to the continuous exposure with a periodic heat source. Prominent examples include the 3ω method, time-domain thermoreflectance (TDTR), and FDTR [62]. All these methods can be applied to the measurement of bulk as well as thin-film materials. For the 3ω method, the main shortcoming is that the modulation frequency is limited at around

100 kHz. Therefore, there the ability to measure heat transport in shallower depth is limited as the thermal penetration length decreases with increasing modulation frequency. The following equation shows the relation

$$l = \sqrt{\frac{k}{\pi C f}} \qquad \text{Eq. 0.4}$$

Here, *k* is the thermal conductivity, *C* is the volumetric heat capacity, *l* is the thermal penetration depth, and *f* is the modulation frequency. Another limitation is that the 3w is a contact method and requires microfabricating heater/thermometer lines over an insulator. FDTR and TDTR are both based on the principle of transient thermoreflectance. Figure 1-8 shows an illustration of the FDTR method. This setup uses a pump laser to induce a periodic temperature change on the sample surface that affects the refractive index of the material, and hence the reflectivity follows the same period. It must be assured that the change in reflectivity due to the change in temperature should be linear, and the change in temperature should also be low such that the linear approximation can be kept. The following equation, approximated to first order, relates the relative change in reflectivity to the temperature change [63]. Here, c_{TR} denotes the thermoreflectance coefficient, *R* is the reflectance (fraction of power reflected from the sample surface) and *T* is the surface temperature.

$$\frac{\Delta R}{R} = \left(\frac{1}{R}\frac{\partial R}{\partial T}\right)\Delta T = c_{TR}\Delta T \qquad \text{Eq. 0.5}$$

Due to this periodic change of reflectivity, the reflected probe signal has a periodicity with the same frequency but a lag in phase relative to the incoming heat flux from the pump laser. This phase lag depends on the thermal conductivity of the measured material and is used to extract the thermal conductivity. Unknown thermal properties of the sample are extracted by minimizing the error between the phase data and an analytical solution to the heat diffusion equation.

The fundamental difference between FDTR and TDTR is that TDTR measures the probe signal's time delay compared to the probe laser's, whereas FDTR measures the phase lag between the pump

and probe sinusoidal signals. Moreover, TDTR employs ultrafast pulse lasers as pump and probe, whereas FDTR uses continuous laser source. The primary advantage of FDTR over TDTR is the simplicity of the setup and its straightforward implementation for FDTR. FDTR does not require an ultrafast laser, electro-optic modulator, and long mechanical delay stages. For both cases, the measured responses are fit into the solution of the diffusive heat equation to extract the thermal properties.

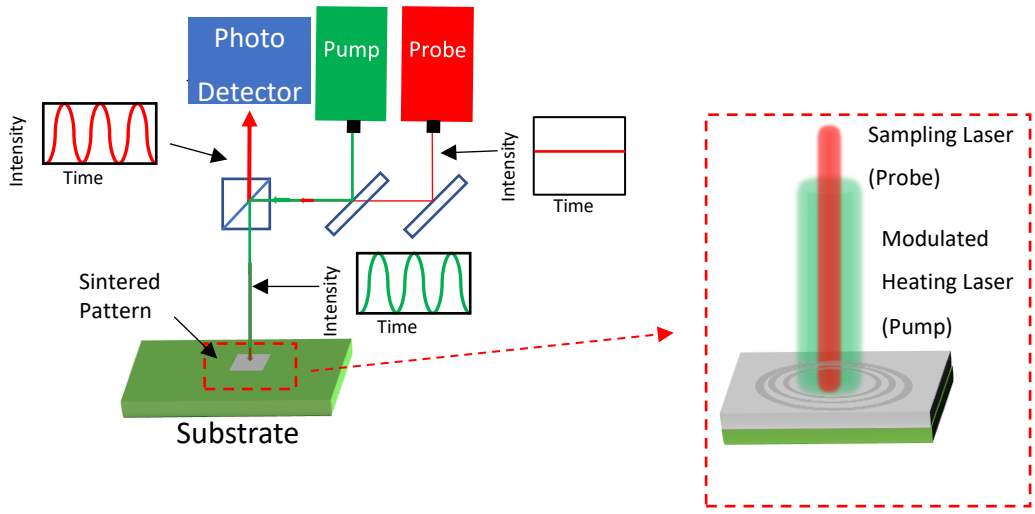

Figure 1-8: Frequency-domain thermoreflectance method: A modulated pump laser periodically heats up the sample surface whereby a probe laser samples the phase lag between the surface temperature and incoming heat flux. The probe laser's intensity is modulated upon reflection due to the change in reflectance from the change in temperature. The inset shows two laser co-axially impinging on the same spot; the pump laser produces heat flux that spreads periodically throughout the surface, whereas the probe samples the response.

The electrical conductivity can be correlated with in-plane thermal conductivity using the Wiedemann-Franz law. The law is stated in the following equation.

$$\sigma = \frac{1}{\rho} = \frac{k}{L * T} \qquad \text{Eq. 1.6}$$

Here k is thermal conductivity, σ is electrical conductivity from sheet resistance, T is room temperature, and L is the Lorentz number, C, which is $2.37*10^{-8}$ $W\Omega/K^2$ for silver. This allows

thermal conductivity values from FDTR to be verified with electrical measurements. More importantly, FDTR results can be converted to electrical conductivity for the characterization of sintered nanoparticle conductors.

The characterization of the sintering process can lead to the exploration of different mechanical/electrical properties of differently sintered material. In this thesis, one application for such sintering optimization is explored. A novel method of fabricating stretchable conductors is shown in which different sintering optimizations for different layers of metallic flake ink are done. The next section is dedicated to different methods of fabricating stretchable electrodes, followed by a brief description of the methodology of the proposed fabrication method.

1.5. Stretchable Conductors

Highly conductive yet naturally stretchable conductors are a crucial enabler for flexible and stretchable electronics. The domain of flexible conductors has seen remarkable advancements due to the increasing need for real-time health care monitoring [64], wearable displays [65], organic solar cells [66], tactile sensors [67], stretchable optoelectronics [68], and smart textiles [69]. In particular, the interest in using traditional printing techniques for the manufacturing of such conductors is growing due to the added benefits of scalability and low-cost fabrication.

The goal is to introduce flexibility (ability to bend and twist to have conformation with curvilinear surfaces) and the capability of maintaining a conductive network under large strains as well as the ability to restore properties after releasing strain [70]. One common approach is to fabricate a stretchable conductor with conventional conductive materials with special structural designs or topographical features to dissipate the strain. Representative examples include out of plane buckling [71], serpentine-shaped [72], kirigami-patterned [73] or micro-cracked topography [74] with conductive features of gold [10], aluminum [75], and indium tin oxide [76] on stretchable elastomeric substrates. Unfortunately, these strategies always ultimately suffer from cracks owing to the rigidity of the abovementioned conventional materials [77][78]. Moreover, they often do not use rapid, low-cost manufacturing processes such as printing [79] with the metal deposition requiring cleanroom lithography and sputtering. Another approach uses microfluidics, replacing wires with filled microchannels of liquid metals [80]. This is promising but needs costly liquid metal such as Gallium-Indium or Gallium-Indium-Tin. Besides, it requires several steps of soft

lithography to create these micro-channels, which renders this method difficult to employ in large-area integration [15]. Forming internal periodic and deformable pores [81], [82] can be an alternative to minimize the stress applied to the materials. Mainly vacuum deposition processes are used, and the material cannot be used as a printable fluid. Another extensively researched solution is conductive nanocomposites comprising of conductive fillers in an elastomeric matrix. The polymeric matrix maintains the elasticity while acquiring the electrical properties of the embedded filler. Various fillers have been studied, such as carbon derived materials including carbon nanotubes (CNT) [83], graphene flakes [84], conducting polymers [85] as well as metallic nanowires [86], nanosheets [87], and nanoparticles [88]. Whichever conductive fillers are used, a percolation network is always created. A downside of such nanomaterials is generally the high cost. Another downside is that the non-linear mechanical properties (viscoelasticity, hysteresis, creep) of such substrates directly influences the electric characteristics of the percolated phase.

For fabrication of stretchable electrodes, printing-based methods have attracted significant attention due to the advantages of inherent compatibility with flexible substrates, low cost, rapid prototyping, and manufacturing scalability. The printing of stretchable interconnects is still in the development stage, with several research groups putting efforts into this area. Tabatabai et al. demonstrated microcontact printing of liquid metal, e.g., Gallium-Indium alloy on an Ecoflex substrate [89]. The print-head carrying the functional ink is in direct contact with the substrate. The variation of resistance of such material while stretching is relatively low, $\Delta R/R0=170\%$ with 100% strain [90]. However, the contact printing of such material is a very time-consuming process; each time the print-head needs to deposit a droplet of Eutectic Gallium-Indium (EGaIn), it goes to a container filled with EGaIn to pick one droplet and then deposit it onto the substrate [25]. Moreover, the natural oxidation of EGaIn makes it challenging to deposit smaller droplets; hence, a low resolution is obtained (linewidth is close to 400 μm). Extrusion-based printing of EGaIn is also gaining attraction due to the potential 2.5D or 3D interconnection printing that enables integration with 3D objects [91]–[93]. Overall, extrusion-based methods for printing EGaIn suffer difficulties in increasing the printing speed and print resolution at the same time due to the poor printability of such material [94]. Other than liquid metals, the most common material for printing of stretchable conductors is high aspect ratio filler based/embedded composites with a few exceptions of spherical nanoparticle filler based inks [28][96]. Spherical nanoparticles are a poor filler for stretchable electrodes as contact points are limited to adjacent filler material owing to

their spherical shape. Thus, the reported value for the maximum strain is typically limited to 30%-40% [25]. Inkjet printing is used in numerous ways for fabricating stretchable electrodes with silver nanowires [30][31]. However, to avoid nozzle clogging, often a sonication-induced scission step is performed to decrease the nanowires' length, which, in turn, reduces the efficacy of the nanowire's (NW) network while stretching. As a result, the stretchability of inkjet-printed silver nanowire electrodes does not surpass 75% strain. Aerosol jet printing is also used to fabricate stretchable electrodes with silver nanowires [99]. However, this process requires a costly printing apparatus with a complicated ink tuning process [25]. Carbon-based ink with high aspect ratio filler such as single-walled carbon nanotubes or graphene is used as a material for contact printing such as screen printing [100] and gravure printing [101]. Material wise, these inks suffer from low conductivity (typically below 100 S/cm) even though they have superior stretchability (sometimes up to 400% of strain). These contact printing methods need a mask or stencil with less flexibility in changing the pattern and added cost.

For extrusion printing, conductive paste, fillers with a high aspect ratio, and an elastomeric matrix are the primary choices of materials. Ahn et al. realized stretchable silver interconnects with an ink-based on spherically shaped silver nanoparticles using micro-extrusion enabled omnidirectional printing [27]. It involves a pre-strained spring that supports a straight line printed onto it. As the ink is nonbrittle, the straight line assumes an out-of-plane serpentine shape after the removal of the spring. Though this micro-extrusion can enable very fine features (~2 μm linewidth), the maximum stretchability is at best 25% strain.

In this thesis, a stretchable conductor is demonstrated by printing micrometer-sized metal flake ink to form co-planar serpentine-like features with an extrusion printer and then encasing them between two polydimethylsiloxanes (PDMS) layers. Thermal curing is typically used to improve the conductivity of such materials. However, the stretchability of these traces decreases with thermal curing. To solve this problem, we demonstrate here a hybrid structure, one fully sintered and one partially sintered feature on top of each other, with improved overall stretchability (up to 120% strain) and conductivity ($4.74*10^4$ S/cm) compared with one single trace. Similar synergistic improvement of both the stretchability and conductivity in a hybrid structure has been reported in literature combining two distinct materials with different stretchability-conductivity profiles. Graphene has been combined with metal nanowires [102], and sintered metal nanoparticles have been combined with liquid metal [103]. With our approach, the fabrication method is simple to

implement and scalable, the material is a relatively low cost, and only a single material is needed. As cracks or breaks in the high conductivity trace occur, rather than losing conductivity, the low conductivity pattern bridges those gaps and maintains the circuit's effectiveness with minimal impact on the overall conductivity.

1.6. Thesis Organization

In this thesis, a new contactless and fast characterization method based on measuring thermal conductivity is proposed and established for printed metal nanoparticle films. First, this method is shown to be viable for conventional thermally sintered films that are fabricated with spin coating. Then, this method is further explored for rapid sintering methods, such as laser sintering and intense pulse light sintering. Finally, as a technology demonstration, a novel fabrication method for stretchable electrodes is shown in which a favorable stretchability-conductivity profile is obtained through sintering optimization.

This thesis consists of five chapters. In chapter 2, the viability of using FDTR as a sintering characterizing tool is explored on a spin-coated printable metal nanoparticle film. Monitoring the thermal conductivity evolution can classify the different stages of sintering with a good correlation with measured electrical conductivity values. A version of this chapter has been published as a conference paper: M. S. Rahman, M. Rahman, S. Pisana, and G. Grau, “Effect of Sintering Conditions on the Thermal Properties of Printable Metal Nanoparticle Ink Studied by Thermoreflectance,” Proc. SPIE 11089, Nanoengineering: Fabrication, Properties, Optics, Thin Films, and Devices XVI, 110890U, pp. 1-7, SPIE Optics + Photonics, San Diego, CA, 2019. doi: 10.1117/12.2529763

In chapter 3, the same characterizing tool is employed for high-throughput printed electronics manufacturing. Conductive features are inkjet-printed, which is one of the most common printing methods for printed electronics, using the same metal nanoparticle ink that is characterized in the second chapter. These printed features are sintered with fast sintering tools, namely laser and intense pulsed light (IPL) sintering. By appropriately choosing the FDTR pump frequencies with the highest sensitivity and calibrating the time constant of the lock-in amplifier used in the setup, we can measure thermal conductivity in a fraction of the traditional measurement time. This speeds up the measurements considerably and makes thermoreflectance a viable characterization technique for high-throughput manufacturing. Finally, a prediction model based on Monte Carlo

simulation is executed to predict a further decrease of the measurement time. A version of this chapter has been submitted as a journal paper: M. S. Rahman, M. Shahzadeh, M. Rahman, S. Pisana and G. Grau, “High-Speed Contactless Sintering Characterization for Printed Electronics by Frequency-Domain Thermoreflectance.”

In the 4th chapter, a method to fabricate highly conductive stretchable interconnects is demonstrated by using an extrusion printer with metal flake as the conductive material. The material’s conductivity increases as the sintering temperature is increased whilst stretchability decreases. To achieve both low resistance and excellent stretchability, we vertically stack two similar serpentine patterns that were sintered at different temperatures leading to two different stretchability-conductivity profiles. While the less sintered line contributes stretchability at the cost of lower conductivity, the more sintered line contributes conductivity with less stretchability. This synergism creates an overall good conductivity vs. stretchability profile. A version of this chapter has been published as a journal paper: M. S. Rahman and G. Grau, “Direct Writing of Stretchable Metal Flake Conductors: Improved Stretchability and Conductivity by Combining Differently Sintered Materials,” Flexible and Printed Electronics, 2020. doi: 10.1088/2058-8585/ab8f22

In the 5th chapter, the main findings of this thesis are summarized, and an outlook with potential future directions is provided.

2. Effect of Sintering Conditions on the Thermal Properties of Printable Metal Nanoparticle Ink Studied by Thermoreflectance[1]

2.1. Introduction

Metal nanoparticle inks are promising to fabricate conductors for low-cost, printed electronics. Low electrical resistivity can be achieved by nanoparticle sintering. The thermal properties of metal nanoparticle thin films have not been studied extensively but can yield significant insights for the optimization of the sintering conditions. For example, in laser sintering, monitoring the changes in thermal conductivity over different stages of the process can help to estimate the local temperature as well as the electrical conductivity of the film. In this work, we use frequency-domain thermoreflectance (FDTR) to measure these properties in a silver nanoparticle thin film, which was thermally sintered ex-situ. The film is fabricated by spin-coating a commercial printable silver ink with monodispersed 35 nm silver nanoparticles surrounded by a ligand. Using frequency-domain thermoreflectance, we measured the thermal conductivity of the thin film by modulating the heat flux over a wide range of frequencies up to 50 MHz. An increase of thermal conductivity with increasing sintering temperature is observed up to a sintering temperature of 155°C, as measured by thermoreflectance or inferred through the Wiedemann-Franz law based on electrical conductivity measurements. Thermal boundary conductance between the silver film and the underlying glass substrate also increases up to 22 $MWm^{-2}K^{-1}$ with increasing sintering temperature. The results are corroborated with material characterization by Scanning Electron Microscopy (SEM) and Energy Dispersive X-ray Spectroscopy (EDS). The thermal and electrical properties are correlated throughout the different stages of sintering. For unsintered films, thermoreflectance gives more accurate values of thermal conductivity because it measures thermal conduction by both electrons and phonons. The Wiedemann-Franz law underestimates the thermal conductivity by 50% in the unsintered case, which is problematic for modeling and optimization of the sintering process. In the sintered state, thermoreflectance and electrical conductivity measurements are in good agreement, as the contribution to heat transport is dominated by

[1]. This chapter has been published in "Effect of sintering conditions on the thermal properties of printable metal nanoparticle ink studied by thermoreflectance" Proc. SPIE 11089, Nanoengineering: Fabrication, Properties, Optics, Thin Films, and Devices XVI, 110890U (2019) with contributions from co-authors M. Rahman, S. Pisana, and G. Grau.

electrons. In short, the thermoreflectance metrology can be used as a non-contact method to determine film conductivity, both thermal and electrical, during manufacturing processes involving nanoparticle inks.

2.2. Fabrication

Nanoparticle films are fabricated on glass using a commercial silver nanoparticle ink (ANP DGP 40LT-15C). The particle diameter is 35 nm, and the primary solvent is triethylene glycol monoethyl ether (TGME). To form a uniform thin film with thickness 80 ±15 nm, first, the glass substrate was plasma cleaned, and then spin coating is used with spin speed 2000 RPM for 60 s.

The prepared films are subjected to a drying step at a temperature of 35°C on a hotplate before the sintering. The films are sintered on a hotplate at different temperatures ranging from 45°C to 185°C. Both the drying step and low-temperature sintering (45°C) continues until the solvent is dried off. Usually, these steps take around 5-6 hours. The high-temperature sintering (65-185°C) is carried out for 30 minutes. Figure 2-1 shows a summary of the fabrication process.

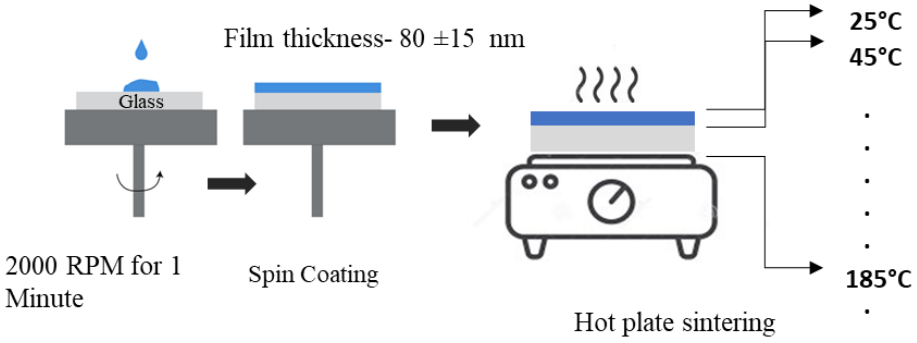

Figure 2-1: Sample Fabrication; thin films are created on plasma exposed glass via spin coating. Several samples are fabricated with different sintering temperatures.

2.3. Characterization

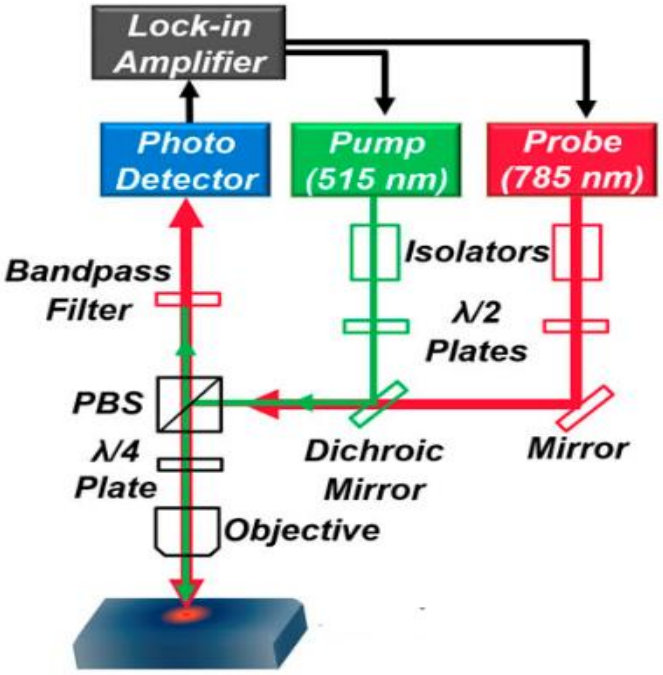

Figure 2-2: FDTR setup; a pump laser periodically heats up a spot, and a probe laser is reflected from this spot with an additional thermal phase. The mirrors and objective are used to guide and focus the beams. A bandpass filter and photodetector are used to collect the reflected probe signal and convert it to an electrical signal.

Figure 2-2 shows a schematic diagram of our FDTR experimental setup. This setup is based on two continuous-wave Omicron A350 lasers, operating as a pump (515 nm) and another as a probe (785 nm) laser. Typically, a metallic layer is used on top of the sample's surface with a high thermoreflectance signal at the probe laser's wavelength. This layer acts as both the thermometer and heater and is referred to as a transducer. However, the addition of this transducer layer complicates the sample preparation and lowers sensitivity to the measurement of high diffusivity materials such as thin metal films. Here, the silver MNPs are directly used as a transducer and material being tested; this is made possible by silver having a sufficiently strong thermoreflectance coefficient at the probe wavelength and having no other layer in the sample that can absorb the pump light. The pump laser is modulated through an analog signal using a Lock-in Amplifier (Zurich Instruments HF2LI), and the probe laser remains unmodulated. A 40X (Olympus RMS40X) objective is used to focus the pump laser onto the sample. This objective decreases the laser spot size. The $1/e^2$ radius of the laser spot on the sample is approximately 1.25 μm. The root-

mean-square (RMS) surface roughness is about 10 nm for this metallic nanoparticle ink (see Figure 2-3). For the 1.25 μm spot size, the roughness is insignificant to distort the reflected signal. For significant (micron-sized) topographical changes or any pores on the surface of the sample, a live optical image feed was used to look at the surface and avoid micron-sized pores or non-idealities on the surface. However, more generally, the FDTR technique relies on the phase difference between the pump and the probe laser, not signal amplitude. As long as reflectivity is large enough to obtain a sufficiently large signal, the result does not depend directly on the value of reflectivity. Therefore, any change in reflectivity due to the nanometer scale surface roughness does not impact the measurement result.

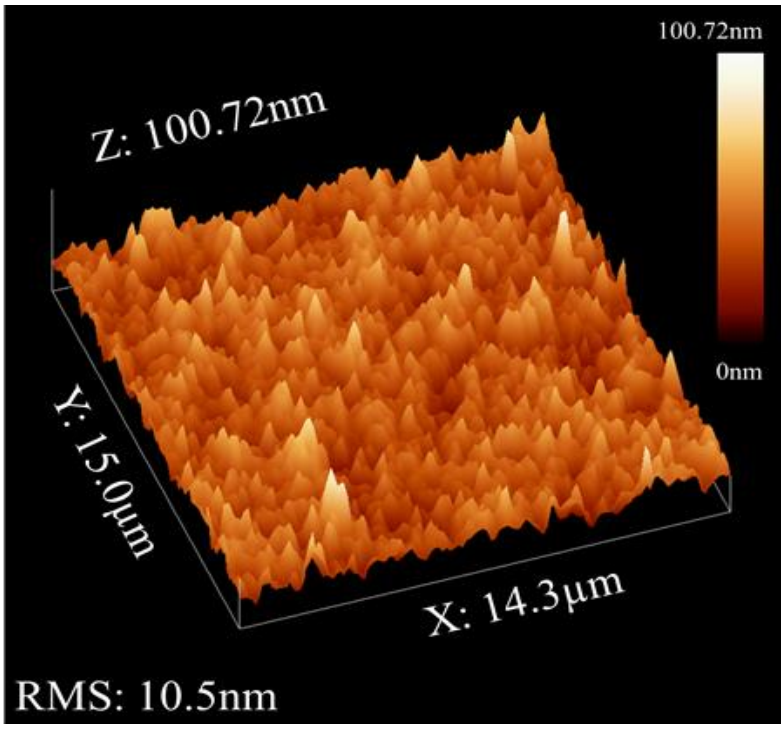

Figure 2-3: Atomic force microscopy (AFM) image of the silver ink used in this study. The root-mean-square (RMS) surface roughness is about 10.5 nm.

This reduction allows a higher intensity thermoreflectance signal because of the increase in surface temperature oscillations and thus allows detection over a wide range of frequencies. Two optical isolators (Con-Optics M711A and M712B) are used for both beams to prevent back reflections into the lasers to prevent destabilizing of the laser source due to back reflections. A polarizing beam splitter (PBS) (Thorlabs PBS 251) is employed to pass vertically polarized pump and probe beams toward the sample followed by another circular polarization of these beams by the quarter-wave

plate (QWP) and focused on top of the sample. When the reflected pump and probe beams travel back through the QWP, the circularly polarized light is converted again into horizontally polarized light, and the PBS redirects both beams toward the photodetector (Thorlabs PDA8A). Two optical bandpass filters working at 515 nm and 785 nm are used to separate the pump and probe beams before these beams reach the photodetector. Due to the absorption of the modulated pump beam, the periodic heat flux causes the surface temperature to change periodically at the modulation frequency, but with an additional thermal phase $\theta_{thermal}$. Two measurements are carried out to isolate this thermal phase from other experimental contributions to the phase signal, as is common in FDTR measurements. The first measurement, referred to as thermal measurement, is carried out measuring the probe beam ($\theta_1 = \theta_{thermal} + \theta_{optical} + \theta_{electrical} + \theta_{reference}$). The second measurement is a reference measurement measuring just the pump beam ($\theta_2 = \theta_{optical} + \theta_{electrical} + \theta_{reference}$). As both beams travel the same distance electrically and optically, $\theta_{thermal} = \theta_1 - \theta_2$. To prevent laser sintering by the pump beam and altering the properties of the nanoparticle film, the laser power is kept small (~100 µW); selected such that the DC temperature rise at the surface is limited to 30°C. The measured thermal phase is fit to a model based on the Fourier Law to obtain the thermal conductivity of the thin film.

The four-point probe method is used to measure electrical sheet resistance (Keithley SMU 2450 Source Meter with SP4 Four Point Head). The sheet resistance is then converted to resistivity with the film thickness measured with an optical profilometer (Contour G.T., Bruker) using the following equation 2.1. Here, R_s and t are the sheet resistance and film thickness.

$$\rho = R_s * t \qquad \text{Eq-2.1}$$

Electrical conductivity is correlated with thermal conductivity using the Wiedemann-Franz law, according to equation1.6 1.6. A Field Emission Gun Scanning Electron Microscope (FEG-SEM, Fisher Quanta 3D) is used for capturing images in the nanometer range and studying the surface morphology of the films at different stages of the sintering process. The same equipment is used to examine the elemental composition of the films by Energy Dispersive X-ray Spectroscopy (EDS). Single point, as well as a large area, for both sintered and unsintered films, are analyzed.

2.4. Results and Discussion

The electrical conductivity increases as the sintering temperature increases from room temperature. Figure 2-4 shows the change. From 35 to 145°C, it monotonically increases from $7.36*10^5$ S/m to $1.869*10^7$ S/m. The sheet resistance exhibits the opposite trend, declining from 16.56 Ω/sq to 0.87 Ω/sq. Beyond 145°C, the increase in electrical conductivity is minimal, remaining close to the value of 145°C. At 185°C, there is a decline in electrical conductivity. The highest electrical conductivity was found to be $2.235*10^7$ S/m for films sintered at 175°C, which is 35.5% of the electrical conductivity of bulk silver.

Figure 2-5 shows the thermal phase vs. frequency plot for a film sintered at 85°C. This is a typical example to show, in general, how well the diffusive thermal model [104] fits the measured data. Figure 2-6 shows in-plane thermal conductivity from FDTR measurements and thermal conductivity calculated from electrical conductivity using the Wiedemann-Franz law with respect to different sintering temperatures. For both measurements, thermal conductivity saturates with sintering temperature. The slope of conductivity with temperature is initially modest up to 125°C sintering.

A jump of 48W/m.K is observed when the sintering temperature is increased from 125°C to 145°C. This is the temperature window when grains start to grow larger via neck formation, as discussed later with the aid of SEM images. After 145°C, any increment of sintering temperature does not affect the thermal conductivity significantly. Both FDTR and thermal conductivity from electrical conductivity follows the same trend as sintering temperature increases, although a gap of 5.6-13 W/m.K. is always present between them. This occurs because the FDTR measurement is a direct thermal measurement, which includes both phononic and electronic heat transport. In contrast, the Wiedemann-Franz law only accounts for electronic contributions. Figure 2-7 shows the change of the phononic contribution of heat transport with sintering temperature increase. In the case of films sintered at low temperatures (35°C to 105°C), that gap, i.e., the phononic contribution is around 5.6-10.61 W/m.K, whereas, this increases to 12-13 W/m.K for films sintered at high temperatures (125°C to 185°C). It is expected that the phononic contribution would increase as sintering progresses. Larger grain size and correspondingly larger mean free path before phonons scatter at grain boundaries result in a larger phononic contribution to thermal conductivity. To explain this behavior in detail, we investigated the surface morphology using SEM. Overall, the phononic contribution as a fraction of overall thermal conductivity decreases with increasing sintering

temperature as the electronic contribution increases. This means that at high sintering temperatures, thermal conductivity can be used to predict electrical conductivity and FDTR can be used to determine the sintering state of nanoparticle films.

Figure 2-8 shows the evolution of thermal boundary conductance at the Ag/glass interface. As the sintering progresses, particles lose their polymeric shells and create a stronger interfacial bond with the substrate than the unsintered cases. These phenomena facilitate thermal conduction across this interface.

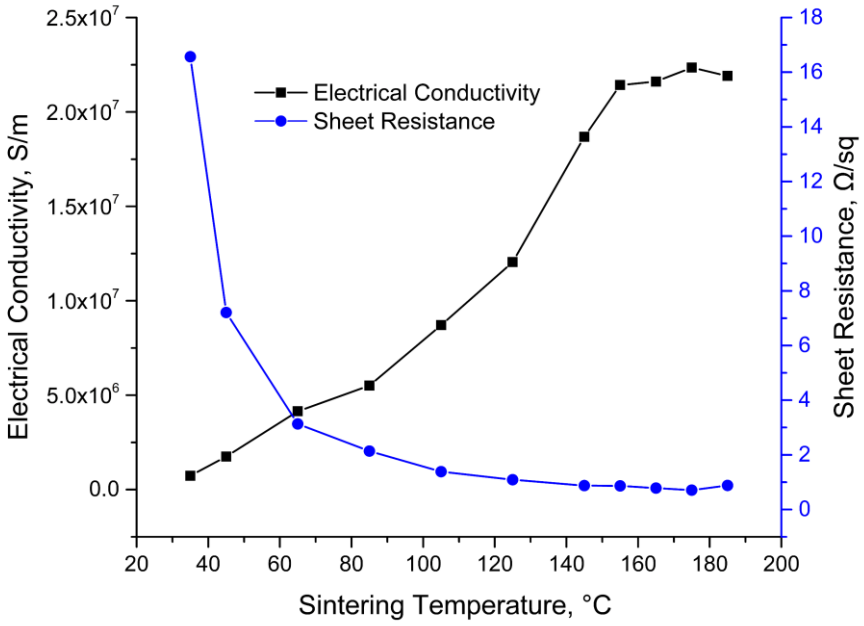

Figure 2-4: Change of the electrical conductivity and sheet resistance as a function of sintering temperature. Films become more conductive with increasing sintering temperature

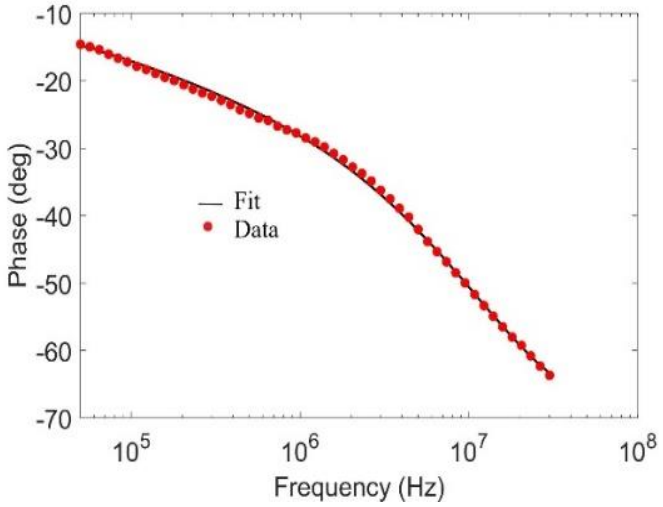

Figure 2-5: A representative example of the measured thermal phase. The solid line represents fit using a diffusive thermal model illustrating good agreement between fit and measured data

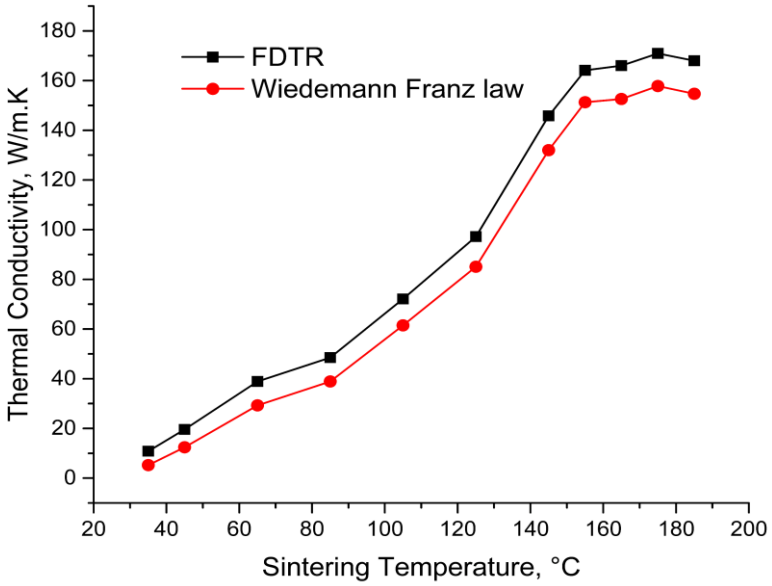

Figure 2-6: Thermal conductivity after sintering at different temperatures measured using FDTR and calculated from electrical conductivity using Wiedemann-Franz law.

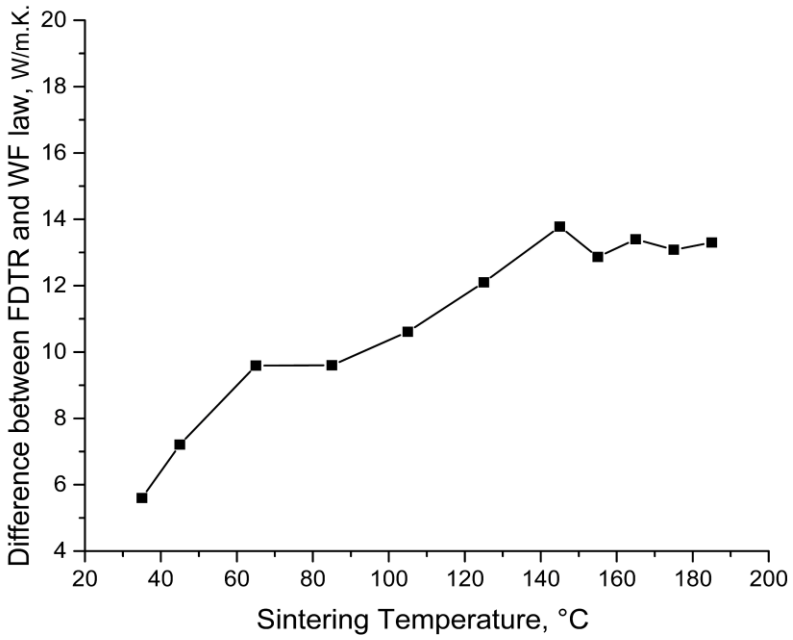

Figure 2-7: Difference between two measurements, i.e., phononic contribution to heat transport vs. sintering temperature. The phononic contribution increases with sintering temperature.

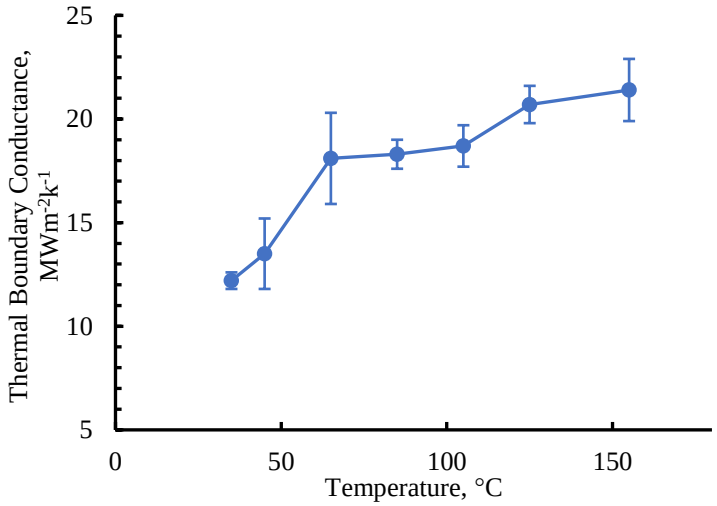

Figure 2-8: Thermal boundary conductance (TBC) across the silver/glass interface as a function of sintering temperature.

Figure 2-9 shows SEM images of the film surface for different sintering temperatures. Up to 85°C, there is no visible change in the size of the grains. Conductivity still rises with sintering temperature because the efficacy of the ligands encapsulating the nanoparticles decreases. Ligand disassociation and transformation to amorphous carbon start to happen, which exposes the

nanoparticles to their neighboring nanoparticles. The extent of this contact increases with sintering temperature, as has been observed before [34]. At 105°C, the onset of neck formation occurs, necks form between some nanoparticles. At this temperature, the phononic contribution starts to increase because of decreased scattering. During the next stage, at 125°C, the grain shape is not spherical anymore, they assume an elongated form. Beyond 145°C, individual grains are hardly visible in SEM. Nanoparticles have coalesced together and formed larger grains. The number of pores increases due to smaller grains merging together because of Ostwald ripening [105]. The formation of a semi-continuous film with no visible grains explains the jump of thermal conductivity from 125°C to 145°C.

After 145°C, the film morphology remains the same, so did the measured values of thermal conductivity. However, at 185°C, the number of pores and their size further increases due to excessive sintering. This affects both thermal and electrical conductivity measurements, which decline slightly. It can be concluded that a safe temperature range for fully sintering this ink is from 155°C to 175°C. The best thermal conductivity of 170.9 W/m.K. is found at 175°C, 40% of the thermal conductivity of bulk silver.

EDS reveals the fraction of different elements present in the spot radius of a few micrometers as well as a 1mm X 1mm area of the sample. The unsintered film contains carbon and silver. Contributions from the underlying glass substrate such as sodium, magnesium, silicon, potassium, calcium, and oxygen are ignored. After sintering, the carbon content is reduced to zero in the small spot size measurement. This signifies that the carbon-containing ligand chains are mostly removed by sintering at 165°C. When a large area (1mm X 1mm) is measured by elemental analysis, a trace amount of carbon is still found. This means, even at a high sintering temperature, ligands are not entirely removed, which has been observed before [34].

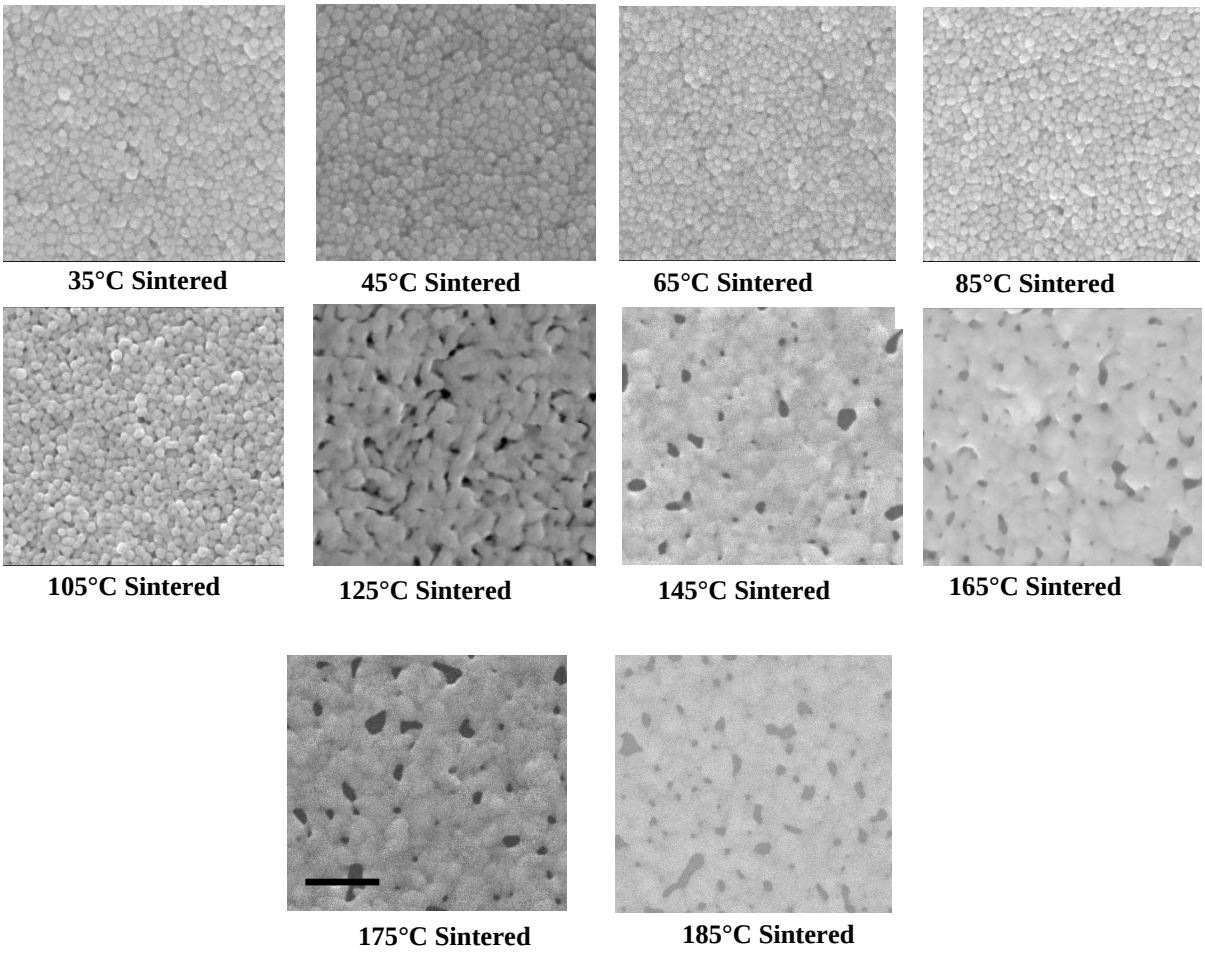

Figure 2-9: SEM images of films sintered at different temperatures. One can clearly observe unsintered individual nanoparticles for films treated at low temperatures up to 85°C. Above this temperature, nanoparticles merge together, and grains grow. Eventually, excessive grain growth leads to voids in the film, which is very visible at 185°C. The scale bar represents 500 nm.

2.5. Conclusion

The thermal conductivity of solution-processed silver nanoparticle films is measured using frequency-domain thermoreflectance without the need for additional steps such as deposition of a transducer layer. We demonstrate that FDTR measurements can be used to determine the sintering state of nanoparticle films. FDTR results are correlated with electrical conductivity measurements. Films sintered at high temperatures exhibit good agreement between the two methods. Therefore, FDTR can be used as a non-contact measurement technique to monitor conductivity in printed electronics manufacturing. Unsintered films exhibit poor agreement between thermal conductivity

measured directly using FDTR and indirectly from electrical conductivity using the Wiedemann-Franz law. The Wiedemann-Franz law underestimates thermal conductivity because phonons contribute significantly to thermal conductivity in the unsintered state. In the future, thermal conductivity measured using FDTR could be used to improve modeling accuracy for optimization of the sintering process. Furthermore, rapid sintering processes can be characterized by FDTR measuring the thermal conductivity, as discussed in the next chapter.

3. High-Speed Contactless Sintering Characterization for Printed Electronics by Frequency-Domain Thermoreflectance[2]

3.1. Introduction

While research has been enabling high-speed roll-to-roll processing in printed electronics by adopting fast sintering methods, there are a few studies on fast and non-contact methods for quality control of the sintered metals. In this chapter, an indirect and non-contact method of characterizing sintered metal nanoparticles is proposed by measuring thermal conductivity by FDTR. Two fast sintering techniques, i.e., laser sintering and IPL sintering, are applied to inkjet printed features. For both cases, different sintering stages are identified and measured thermal conductivity values correlate well with the measured electrical conductivity through the Wiedemann-Franz law. Then, the measurement time is significantly reduced to 12 s by appropriately choosing six FDTR pump frequencies with the highest sensitivity and taking all the selected frequency-vs-phase data points at once. In this way, the measurement time decreases considerably, and thermoreflectance becomes a suitable characterization technique for high-throughput manufacturing. A Monte Carlo based prediction was performed to observe the effect of shorter measurement time on phase noise, and a much faster measurement configuration is proposed with an acceptable uncertainty in measurement. Our results demonstrate a simple approach for high-speed non-contact characterization of metal nanoparticle conductors with the combination of high-speed printing and high-speed sintering for low-cost electronics manufacturing. Figure 3-1 demonstrates the envisioned high-speed in-line monitoring with FDTR. IPL sintering is shown as an example.

[2] Section 3.3 of this chapter is submitted as a journal with the title of "High-Speed Contactless Sintering Characterization for Printed Electronics by Frequency-Domain Thermoreflectance", with contributions from co-authors M. Shahzadeh, M. Rahman, S. Pisana, and G. Grau. This section will also be presented at the 20th IEEE International Conference on Nanotechnology, Montreal, 2020.

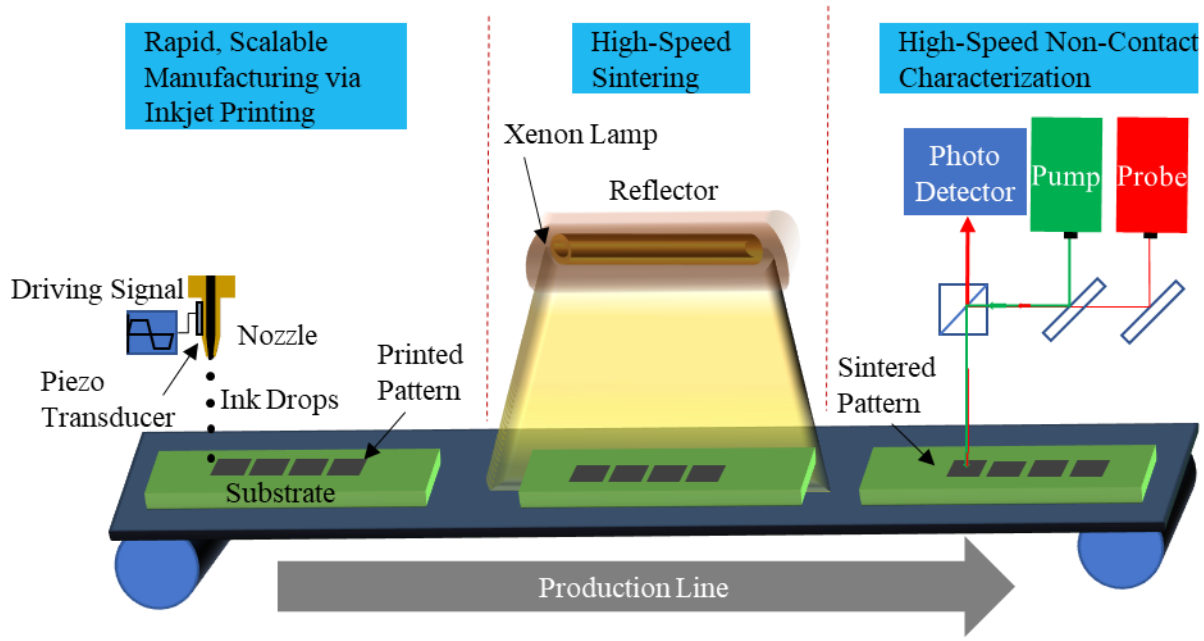

Figure 3-1: Illustration of a potential roll-to-roll production line. First, metal nanoparticle features are deposited and patterned with a scalable and fast fabrication method: drop-on-demand inkjet printing. A voltage waveform drives the piezo actuator, connected to the nozzle, to eject ink droplets. The movement of the substrate relative to the nozzle creates the pattern of droplets on the substrate. In the second step, a Xenon lamp provides ultrafast flash light sintering using the photothermal effect. In the third step, a non-contact, optical pump-probe measurement characterizes the sintered features in terms of thermal conductivity. This value can be used to make decisions on the quality of sintering.

3.2. Laser Sintering Monitoring With FDTR

Continuous-wave laser sintering [48] [10] [58] is an emerging sintering method that has potential in high throughput manufacturing. Moreover, it can potentially be used for sintering on plastic substrates if one optimizes the sintering parameters carefully. Such laser sintering is executed here on the same materials that are used above but using square features fabricated with inkjet printing.

An initial experiment was performed to find out how well the heat is localized in the film with respect to the laser beam diameter, which is 1.5mm. The final sample dimensions are fabricated according to the sintered area (laser exposed area) that is found in this experiment. A spin-coated film with a thickness of approximately 74 nm is exposed to three different laser conditions, that is, three different exposure times with the same power. Figure 3-2 shows the change of sheet

resistance as a function of position from one end of the laser spot to the other. Decreased sheet resistance resulting from the laser exposure exhibits an inverse hat structure, where the bottom center of the hat denotes the lowest resistance, coinciding with the laser spot's center. Moreover, these resulting shapes from the laser exposure also reveal the Gaussian shape of the laser fluence on the samples. Beyond the bottom of these hat shapes, the sharp rise of the resistance reveals the laser spot's reach. One can see that with increasing exposure time, the laser affected area is also increased. Even with the most prolonged exposure, the overall affected area is limited to 2000 μm diameter. Specifically, the resistance does not change significantly surrounding the very center, up to 1000 μm. Therefore, for laser sintering of printed features, the dimensions of the fabricated patterns are chosen as 1000 μmX 1000 μm.

A custom-built inkjet printer with a nozzle of 60 μm diameter (MJ-ATP-01-60-8MX, Microfab Technologies, Inc., Plano, TX) is used to jet and deposit 16 square-shaped features. The nozzle is scanned in a raster motion (each line starts with the same X position) to deposit inks. These features are printed with the previously specified dimension. The ink's viscosity is in the range of 15-17 mPa.s, and a trapezoidal bipolar waveform of 56 V peak-to-peak was applied to the nozzle's piezoelectric actuator to achieve stable jetting. Figure 3-3 represents two cases of laser sintering, sample (a) is low laser power sintered with 5 mW for 70 s and sample (b) is high power sintered with 37 mW for the same time.

Two sintering parameters, laser power and exposure time, are varied. Four different laser powers, from 5 mW to 37 mW with four different exposure times, from 40 s to 70 s, are used for the sintering. Figure 3-4 shows the trend of electrical conductivity change with laser power and exposure time. It can be noticed that, for all exposure times, with increasing laser power from 5 mW to 25 mW, the electrical conductivity also increases.

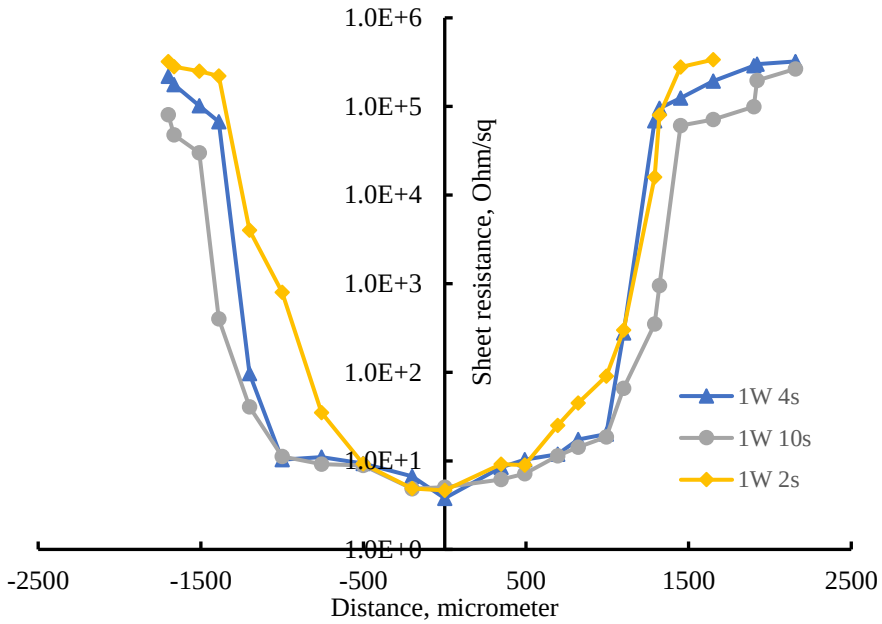

Figure 3-2: Sheet resistance evolution is correlated with laser spot position. Sheet resistance has the lowest value at the center of the laser spot. Resistance values increase at the spot's periphery, denoting a heat localization around the laser spot.

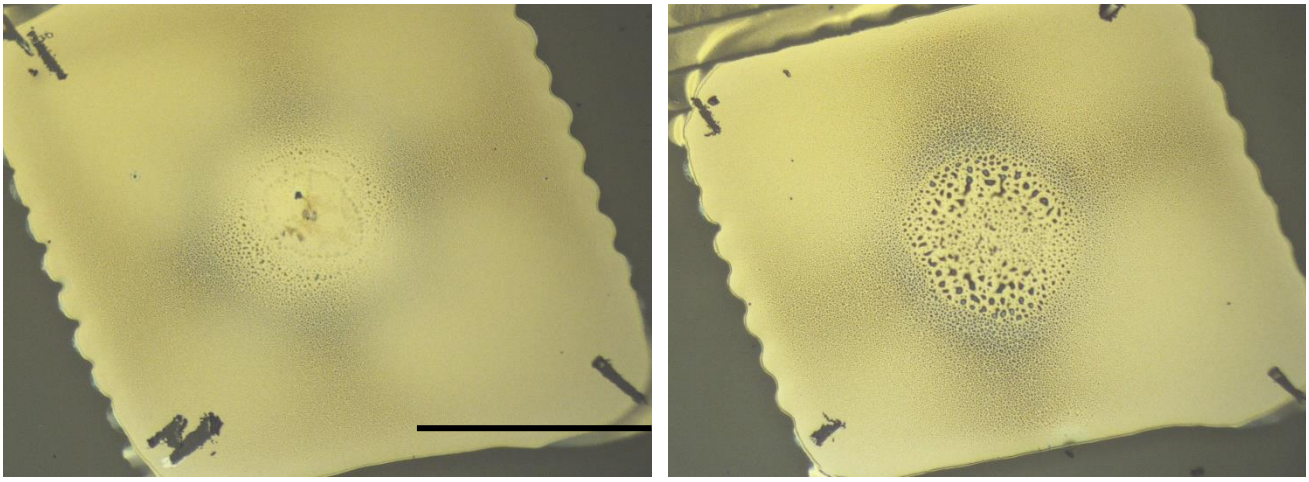

(a)

(b)

Figure 3-3: Optical micrographs of representative examples of laser-sintered features. (a) is exposed to lower laser power (5 mW) than (b), which is exposed to 37 mW. The higher laser power sintering causes much more porosity than the lower laser power. The scale bar represents 500µm.

Electrical conductivity does not cross $6*10^6$ S/m with 5 mW of sintering, at all values of exposure time. 25 mW laser power for 60 s of sintering provides the highest electrical conductivity, $9.5*10^6$ S/m. At 37 mW laser power, the electrical conductivity falls sharply, becomes even lower than that of the lowest power's conductivity. Three different stages of sintering can be identified from this graph in terms of electrical conductivity. One is the under-sintered case with 5mW (for all sintering times), the moderately sintered case with 25 mW and 60 s of sintering time, and over-sintered case with 37 mW (for all sintering times). Three distinctive cases of these three sintering stages are taken, and FDTR was used to measure their thermal conductivity. These thermal conductivity values are compared against the thermal conductivity values measured from Wiedemann-Franz (WF) law, using equation 1.6. Figure 3-5 shows the in-plane thermal conductivity from FDTR measurements and thermal conductivity calculated using the WF law. A reasonable correlation and a general trend between the two measurements can be observed. Again, the best agreement is found for more sintered samples. The highest thermal conductivity value found is 15% of the previously reported value with thermal sintering. Further optimization of the laser sintering parameters such as laser power, sintering time, and energy density per area could likely improve conductivity further.

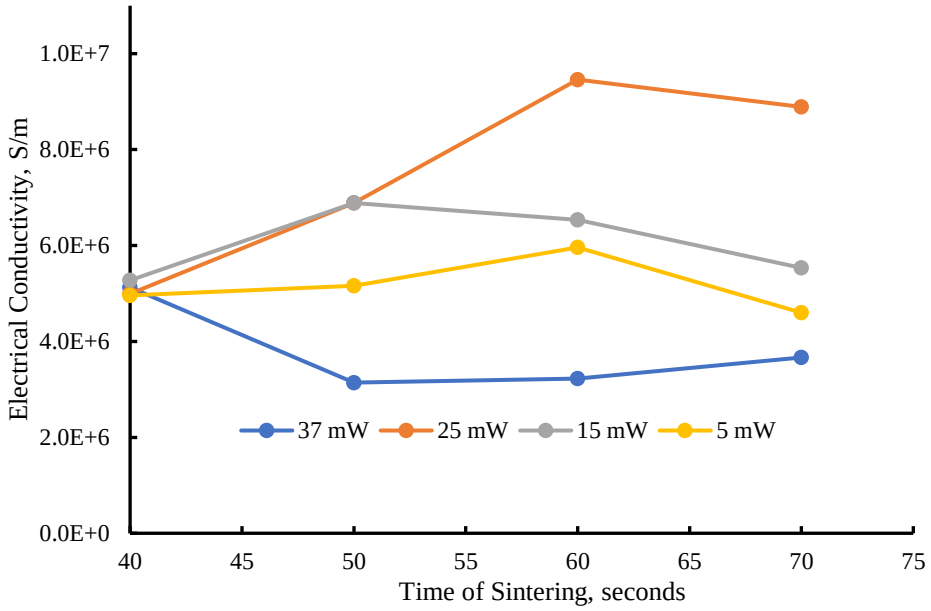

Figure 3-4: Change of electrical conductivity as a function of laser power and exposure time.

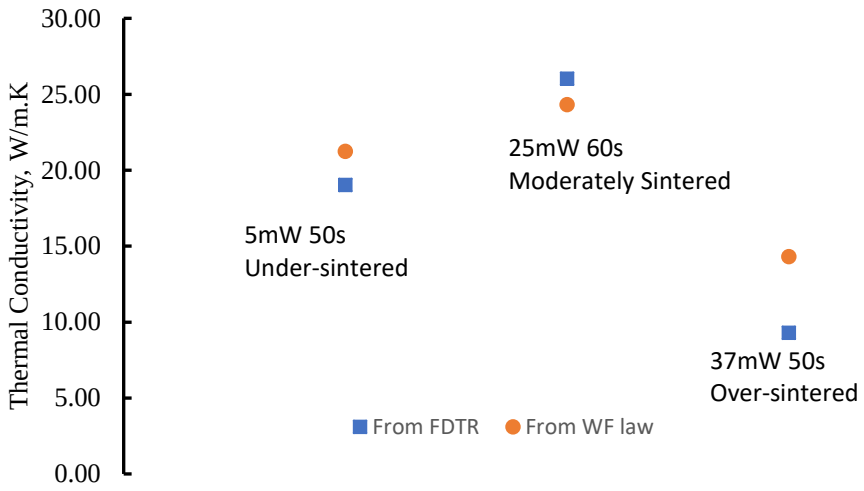

Figure 3-5: Thermal conductivity after sintering at different laser parameters measured using FDTR and calculated from electrical conductivity using Wiedemann-Franz law.

3.3. IPL Sintering With FDTR

IPL is one of the fast sintering techniques that enables the usage of cheap plastic substrates. FDTR characterization is successfully integrated with the IPL sintered metal nanoparticle film as well. Initially, we demonstrate the compatibility of these different fabrication methods with FDTR using a full frequency sweep. The extracted in-plane thermal conductivity agrees well with other measures of sintering, namely electrical conductivity, and surface morphology. This measurement was used as a baseline measurement. However, a full frequency sweep takes around six and a half minutes in total, which is not desirable to be used in high-throughput manufacturing. This is overcome by selecting a subset of six frequencies to perform the measurement on. This reduces measurement time without significantly sacrificing the goodness of fit of the thermal model to the measured data. Additionally, these six frequency data points can be measured simultaneously by including all frequency components in the pump amplitude modulation and demodulating all frequencies concurrently. By implementing these two strategies together, the measurement could be performed in 12 seconds while increasing uncertainty relative to the baseline by 5%. This increases the compatibility of this method with a high-throughput manufacturing environment. Finally, a Monte Carlo Simulation was performed to predict limitations on further improvements in measurement time by the contribution of added phase noise. This simulates the effect of lower

integration time of the lock-in amplifier, which would result in much faster measurement but also increases phase noise. This estimates the propagation of introduced random noise to the properties derived from the analysis of FDTR data [61]. It is shown that the measurement time can be cut down to hundreds of milliseconds and still be within 3.5% of the baseline value.

3.3.1. Fabrication and Post Processing by IPL Sintering

The same manufacturing setup is used as before to print square-shaped features, except the printing is done following an inward spiral filling rather than raster scanning. The prepared films are subjected to a drying step at a temperature of 50°C for 2 hours before performing intense pulsed light sintering (X-1100, XENON Corporation, Wilmington, MA). We sintered dried films with different IPL parameters to monitor the progression of electrical conductivity with these parameters. All sintering steps are done at room temperature and under ambient conditions. We control the pulse fluence (energy density, J/cm^2 per pulse) by changing the capacitor bank voltage driving the Xenon lamp while keeping the pulse width constant (4.5 ms). Various values of pulse fluence are used, ranging from zero to 7.3 J/cm^2 to monitor their effect on electrical conductivity. The effect of pulse count is also studied at fixed pulse fluence and pulse width. For all IPL sintering experiments, the samples were placed ~1 inch away from the lamp surface.

3.3.2. Characterization with FDTR Using Full Frequency Sweep

Adopting the inward filling method provides well-defined squares with minimal corner-rounding printed with a negligible coffee ring effect, ensuring the uniformity of the material deposition. Figure 3-6**Error! Reference source not found.** (a) shows the shape of printed squares on the glass. The thickness of these squares is 650 ±120 nm. A typical thickness profile is shown in Figure 3-6**Error! Reference source not found.** (b). The thickness variation in a single rectangle is within 10% of its average value. This uncertainty in thickness is sufficiently small to reliably extract thermal properties from FDTR results where the thickness is a parameter in the analytical FDTR model

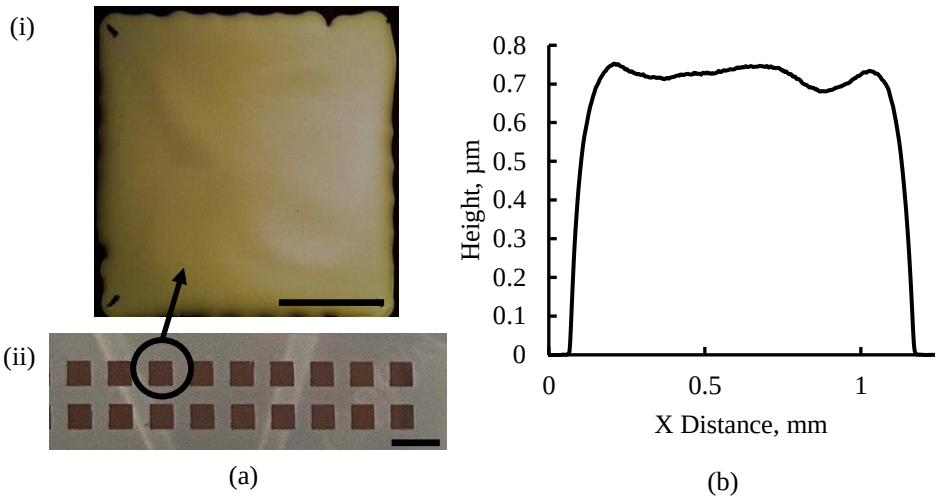

Figure 3-6: a) (i) Zoomed in optical micrograph of one of the printed squares, the scale bar represents 250 µm (ii) An array of printed squares, the scale bar represents 2 mm. b) A representative example of a height profile of a printed square.

The electrical conductivity increases as the pulse fluence, i.e., energy density per pulse, is increased, as shown in Figure 3-7 (a). Here, the number of pulses is fixed to 30 so that the effect of pulse fluence on electrical conduction can be observed. From 2.8 J/cm^2 to 5.91 J/cm^2, the electrical conductivity increases proportionally from 5.47*10^6 to 1.99*10^7 S/m. At 7.26 J/cm^2, there is a decline in electrical conductivity due to over-sintering, later confirmed through SEM images. Figure 3-7 (b) represents the effect of the number of pulses as well as total energy density on the electrical conductivity. In this case, the pulse fluence was kept constant at 5.91 J/cm^2. Total energy density is calculated by multiplying the pulse number with the pulse fluence. The highest electrical conductivity, 2.26*10^7 S/m, is found when the sample is subjected to 45 pulses. This value is 35% of the bulk silver conductivity, matching our previous results using thermal sintering [9].

The measured phase signal's sensitivity in response to the in- and out-of-plane thermal conductivity (k_r and k_z respectively) is shown in Figure 3-9 (a). We fit for both parameters in the thermal model. From the sensitivity plot, one can see that the phase sensitivity for k_r is larger than for k_z. Generally, we obtain k_z values that are larger than k_r and close to bulk silver pointing to an anisotropy in the film. However, due to the low sensitivity to k_z, the outcome of the fit for k_r, the desired output of these experiments, does not depend significantly on whether k_z is a fitting parameter or assumed constant at the bulk silver value. Within the frequency range considered, a

higher modulation frequency results in a higher sensitivity. However, at higher frequencies, the measurement noise increases too. Therefore, the measurement is limited up to 10 MHz. The results are somewhat sensitive to all other thermophysical parameters of the system as inputs to the fit such as optical spot size, volumetric heat capacities of the film and the substrate, thermal conductivity of the substrate, and thickness of the substrate and film (see Figure 3-8 (b)for sensitivity plot and Figure 3-8 (c) for effect on uncertainty). Notably, the sensitivities (except for the spot size) are much lower than the sensitivity to the in-plane thermal conductivity of the silver film. Additionally, in a manufacturing setting, they should be assumed to be constant and known beforehand. All other thermophysical parameters of the system, such as optical spot size, volumetric heat capacities of film and substrate, and k for the substrate, are assumed to be constant and known. Although we show the sensitivity to k_r and k_z individually, the film is assumed to be isotropic, and only one parameter is fit.

A typical experimental phase vs. modulation frequency plot with the analytical fit for a silver nanoparticle/glass sample is shown in Figure 3-9 (a). This represents the goodness of the fit between the measured and fitted values. Figure 3-9 (b) shows the in-plane thermal conductivity from FDTR measurements and thermal conductivity calculated from electrical conductivity using the Wiedemann-Franz law with respect to pulse fluence. For both measurements, thermal conductivity shows the highest value, 144.5 W/m.K, at around 5.91 J/cm^2 and decays down at 7.3 J/cm^2. Figure 3-9 (c) shows the thermal conductivity from FTDR and converted from Wiedemann-Franz law with pulse count as well as total energy density. Again, electrical measurements and FDTR agree well.

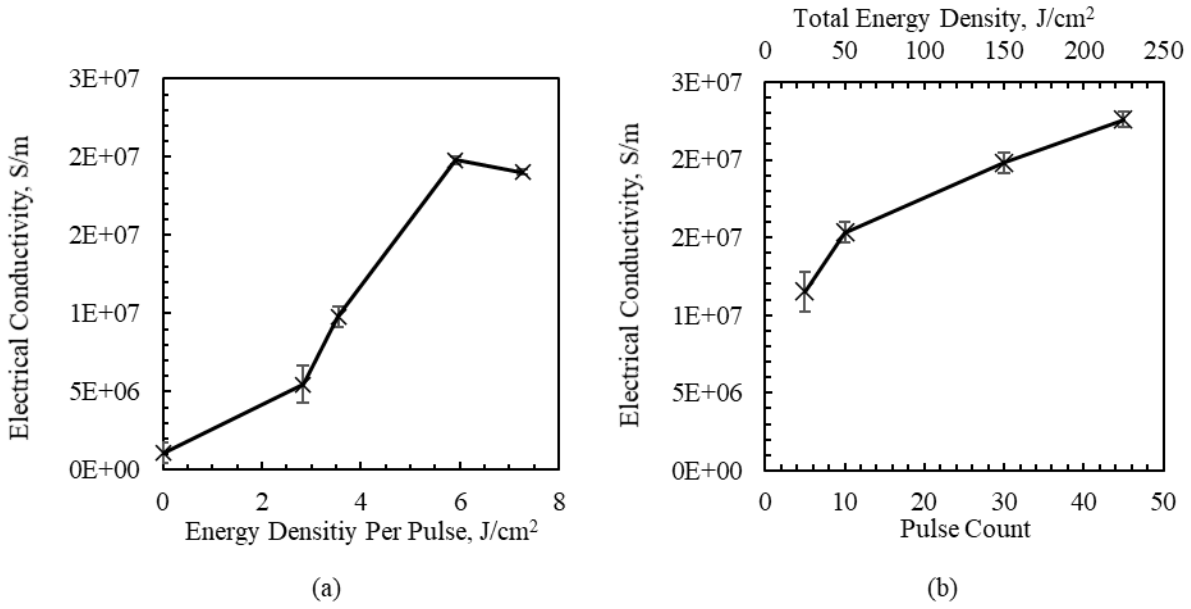

Figure 3-7: (a) Change in electrical conductivity as a function of pulse fluence. Films become more conductive with increasing fluence until over-sintering occurs. Pulse count was kept constant at 30. (b) Electrical conductivity after IPL sintering increases with increasing pulse count with the same pulse fluence (5.91 J/cm^2). The secondary axis shows the total energy density with increasing pulse count.

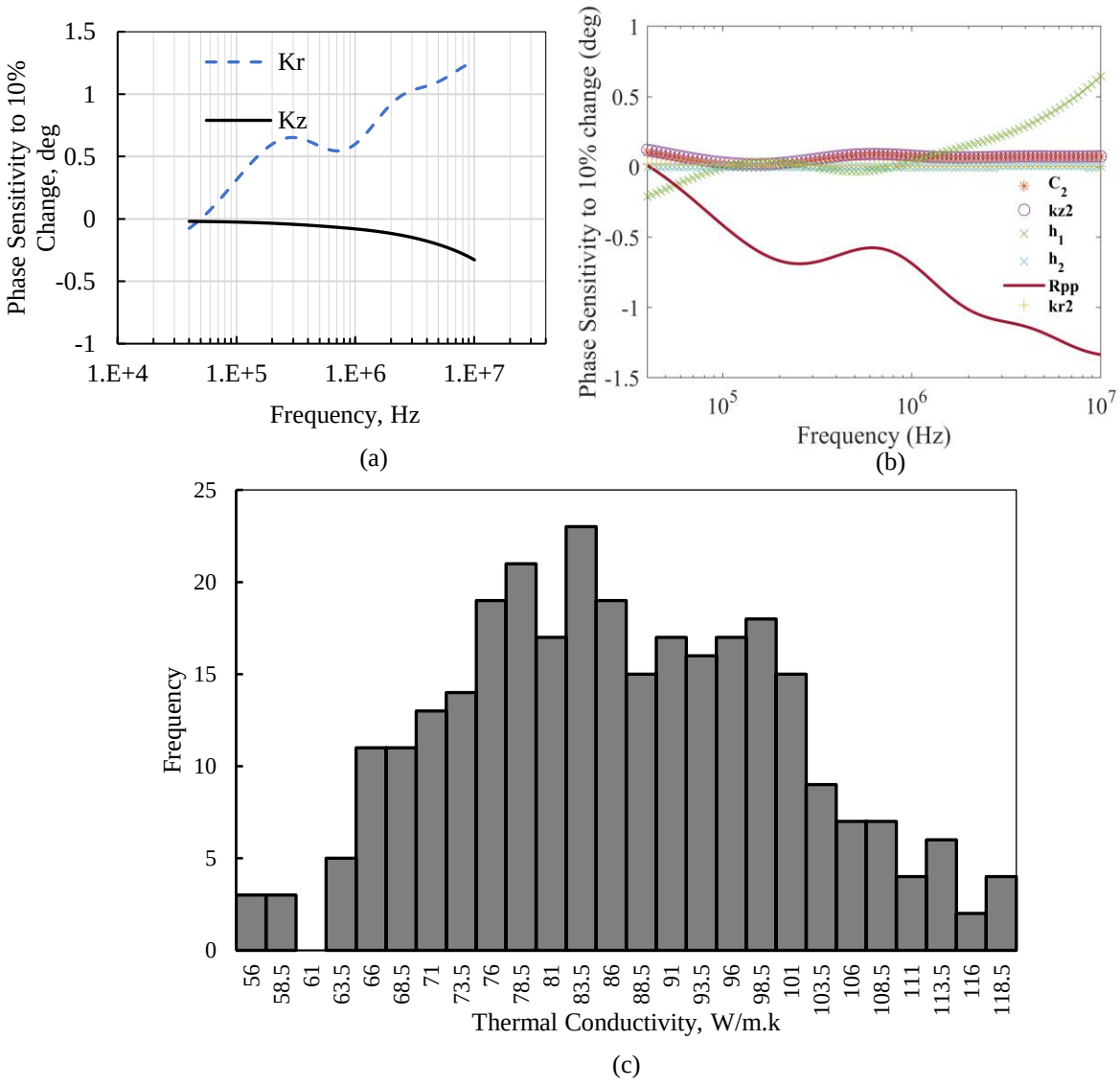

Figure 3-8: (a) The sensitivity of the measured thermal phase to the in-plane and out of plane thermal conductivity. (b) The sensitivity of the measured thermal phase to the thermal properties of glass such as in-plane (kr2) and out of plane thermal conductivity (kz2), heat capacity (C_2), spot size of pump laser (Rpp), thickness of glass (h2) and thickness of the silver film (h1). (c) Histogram from Monte Carlo analysis of 300 fits for intermediate thermal conductivity sample with 10% error in substrate and film parameters: glass in-plane and out of plane thermal conductivity, heat capacity, spot size of pump laser, thickness of glass and thickness of the silver film.

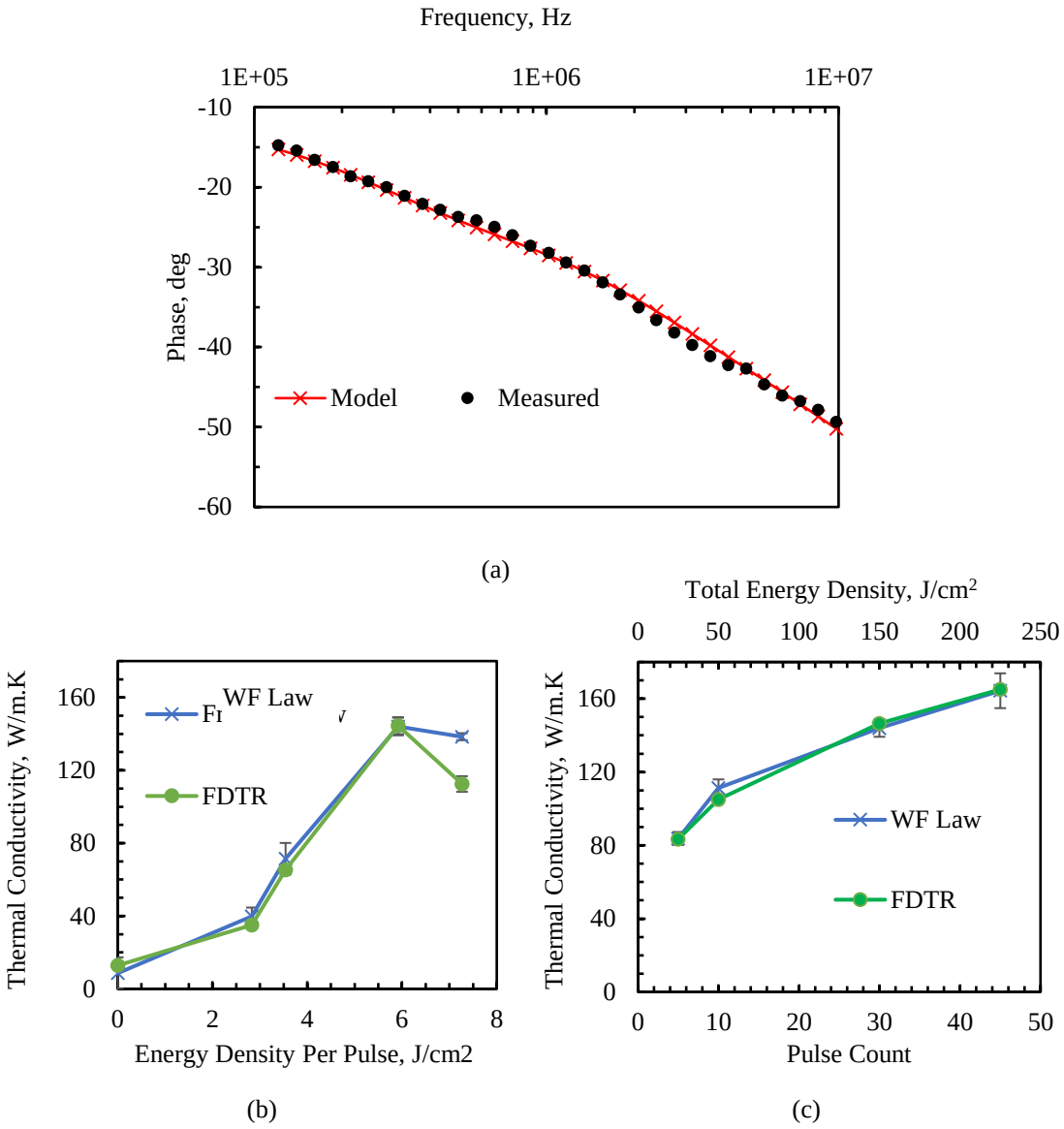

Figure 3-9: (a) A representative example of the thermal phase vs. frequency plot of measured FDTR data and fitted through analytical modeling, representing a good agreement between fit and measured data. (b) Thermal conductivity after IPL sintering at different values of pulse fluence measured using FDTR and calculated from electrical conductivity using Wiedemann-Franz law. (c) Effect of pulse count on thermal conductivity from FDTR and Wiedemann-Franz law. The highest thermal conductivity is found at 45 pulses.

Figure 3-10 shows the surface morphology SEM images of films for different values of pulse fluence. Figure 3-10 (a) shows a representative example of an under-sintered case. The individual

grains are visible with less contact with neighboring nanoparticles. In the well-sintered case (Figure 3-10 (b)), the grain shapes are not spherical, and long necks have grown. A noticeable percolation network for carrier transport is established; hence, the highest thermal conductivity is found. However, with a high fluence such as 7.3 J/cm^2, both the number and the size of pores increase due to excessive sintering (Figure 3-10 (c)). This phenomenon can be explained with excessive aggregative growth, leading to non-uniform particle distribution with more voids in the inter-particle network [106]. The effect of such over-sintering is evident in the declining thermal and electrical conductivity values. The increasing pore size can also affect the film's heat capacity, which is a parameter of the thermal model. We fit the thermal model for heat capacity and in-plane thermal conductivity for an over-sintered film, which is highly porous and, therefore, the worst case. With an excellent fit, volumetric heat capacity was found to be 2.35*10^6 J/m^3.K, which is close to the otherwise assumed bulk value for silver of 2.5*10^6 J/m^3.K, and thermal conductivity decreased by about 4%.

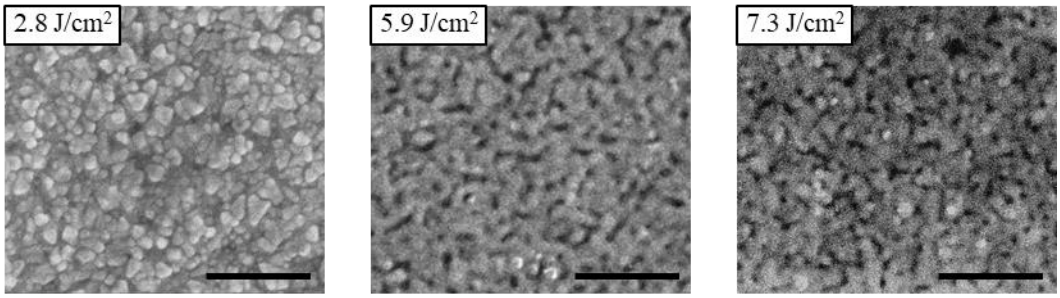

Figure 3-10: SEM images of the surface morphology for different sintering conditions with different values of pulse fluence and the same pulse count (30). Scale bar represents 500 nm. (a) Individual grains are visible as the sample was under-sintered at low pulse fluence (2.8 J/cm^2). (b) Well-sintered samples with a moderate pulse fluence (5.9 J/cm^2), exhibiting a well-defined percolation network. (c) Slightly over-sintered case with increased number of pores with increased pore size at high pulse fluence (7.3 J/cm^2).

3.3.3. FDTR Characterization with a Small Number of Data Points

Next, we performed an experiment where fewer frequency-vs-phase data points are taken, and the same analytical model was fitted to this measured data. The rationale behind this experiment is that the fewer data points are experimentally measured, the lower the time for each measurement will be. Unlike the previous measurement, where each measurement serially captured 32 frequency-vs-phase data points, only six points are taken now. Moreover, a multi-frequency lock-in amplifier (Zurich Instruments HF2LI) simultaneously modulates the pump signal with these six frequencies, and hence all the points are measured at the same time. In this way, the characterization time was lowered to 12 seconds, whereas the full frequency sweep would take more than six minutes. Figure 3-11 (a) shows that the computed data from the diffusive thermal model fits these six measured frequency data points well. Figure 3-11 (b) shows the measurement uncertainty determined from a Monte Carlo simulation with a phase error of 1 degree for different numbers of frequency data points. With a decreased number of frequency points (which are the number of modulator/demodulator modules running at once), the uncertainty in measuring thermal conductivity in three differently sintered materials tends to increase. From thirty-two to six frequency data points the uncertainty only increases from about 2% to about 5%. Below six frequencies, which is the maximum number in our system, the uncertainty increases further and there exists a trade-off between measurement uncertainty and number of modulators. Figure 3-11 (c) shows the comparison of two experiments with respect to their phase values. The two experiments were taken on different spots on the same sample, one with the full frequency sweep and one with only six datapoints. A small discrepancy can be observed but the fitted in-plane thermal conductivity agreed within 5% (87.2 W/m.K for six-point measurement, 83.6 W/m.K for full modulation frequency sweep). This attests to the viability of using just six frequencies as well as the repeatability of the inkjet printing and IPL sintering processes. The remaining discrepancy between the measurements can generally be attributed to spatial variability of the samples and increased measurement uncertainty with fewer frequency data points (see Figure 3-11 (b)). In short, by sacrificing a small amount of accuracy in the measured thermal conductivity, the whole characterization time can be cut down to seconds.

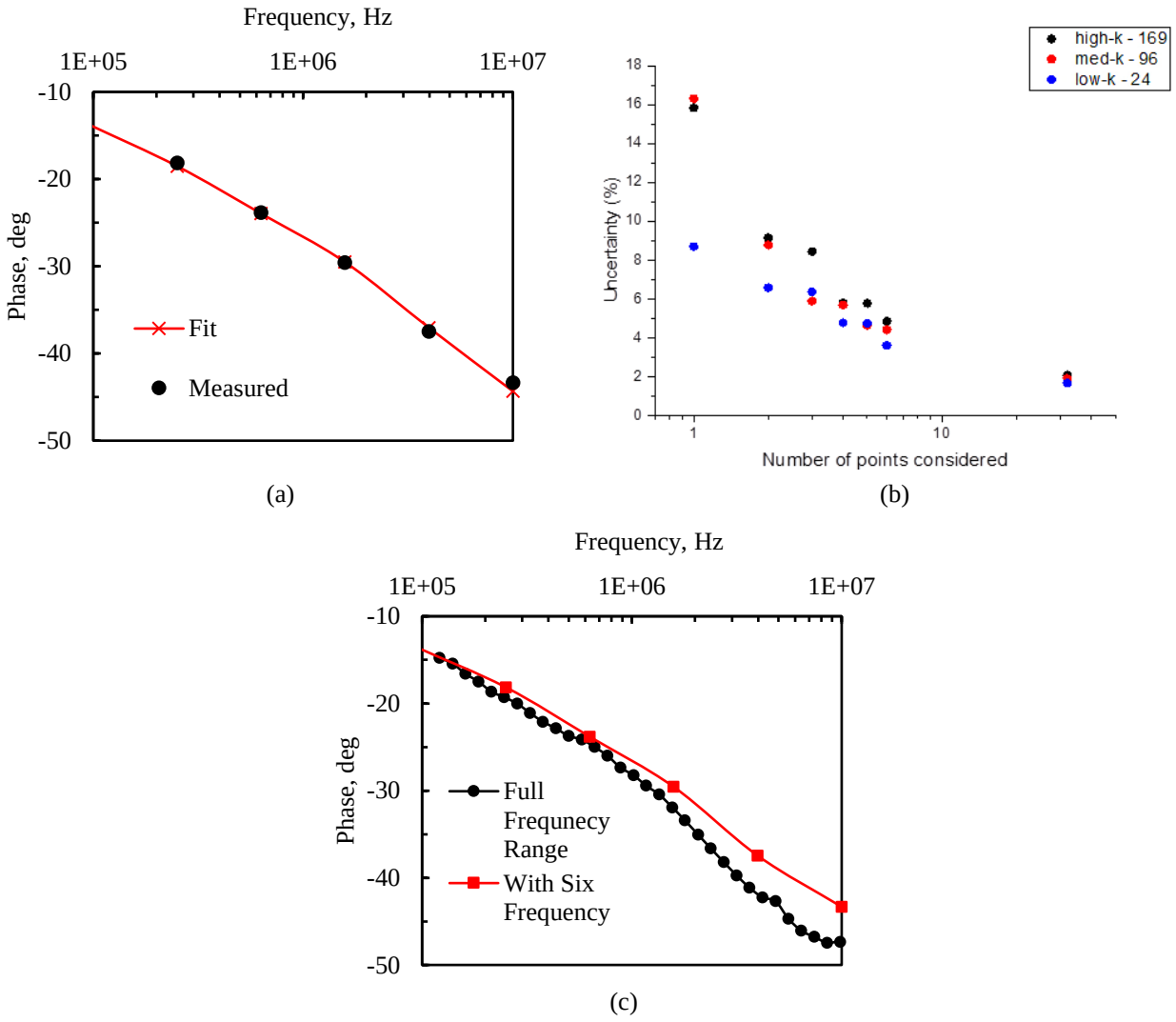

Figure 3-11: (a) Comparison of the thermal phase data from the measurement and the analytical fit. The solid line represents the analytical solution with the diffusive thermal modeling, that fits the measured values well. (b) Effect of the number of frequency data points on the measurement uncertainty for samples with different thermal conductivity. Uncertainty has an inverse relationship with the number of frequency data points considered. (c) Comparison of the phase data between two experiments on different sample locations, one is with the full frequency range, which takes longer than the other having only six frequencies measured simultaneously.

3.3.4. Prediction of Faster Measurement

A lock-in amplifier always poses a trade-off between improved accuracy with longer integration time versus a faster measurement. The integration time corresponds to the inverse of the bandwidth of the low-pass filter in the lock-in amplifier, which is used to exclude higher frequency components of the signal, such as noise. The lower the integration time, the shorter the lock-in amplifier takes to complete the measurement. The total experimental measurement time of 12 s uses an effective integration time of 3 s (averaging over 10 measurements each with integration time 0.3 s). Before taking the measurement, we wait another 3 s for the measurement to settle. This 6 s procedure is repeated to make a reference measurement to null the other unwanted phase contributions. This is a conservative approach and the measurement time can likely be reduced by reducing the time to wait for the measurement to settle as well as the time for the reference measurement, which has a larger signal to noise ratio than the actual measurement. However, the most direct approach to reduce measurement time is by reducing the integration time, but this also results in noisier data. Therefore, the extracted thermal conductivity from such data will be more uncertain.

Here, a Monte Carlo computational approach is employed to calculate the measurement uncertainty by introducing phase noise to existing FDTR data and observing the trend of the deterioration in the fitted thermal conductivity values with increased noise. The more noise we can afford within an acceptable tolerance level, the shorter the integration time we can use, and the faster the measurement becomes. A static phase measurement at different modulation frequencies for different lock-in integration times was conducted. The measurement shows that the distribution of phase noise values is mainly a normal distribution. We used these values to determine the phase noise at different frequencies and integration times. Figure 3-12 (a) shows this experiment's results with four different frequencies ranging from 160 kHz to 10 MHz. From the sensitivity plot in Figure 3-8 (a), it can be concluded that the highest sensitivity is at higher frequencies, but these data points tend to also be noisier than low frequencies. The phase noise dependence on frequency was modeled by fitting a power law of the form $y=a*x^b$ for each of the three studied integration times. This model is used to predict the effect of phase noise on thermal conductivity measurements with different integration times. The noise is significantly reduced when integration time is increased from 0.02 s to 0.3 s. However, beyond 0.3 s other noise sources dominate that cannot be removed by averaging on this time-scale, such as laser phase instability. Therefore, the

phase noise vs frequency characteristics are very similar for 0.3 s and 2 s integration time. Three different samples with three different thermal conductivities are taken, and frequency-dependent random noise for different integration times is added to their respective experimental phase values. Figure 3-12 (b-c) represents such an example. In Figure 3-12 (b), the analytical model is fit to the phase data obtained from a typical full frequency sweep. Figure 3-12 (c) represents such a fit to the same dataset with an addition of frequency-dependent random phase noise for 0.3 s integration time. Such cases of random noise addition and fitting to the data were done for 100 independent iterations to provide statistical significance. The statistical variation of the extracted thermal conductivity values represents to what extent the noise affects the deduced thermal conductivity. Figure 3-12 (d) shows a representative histogram of 100 fits for samples with high thermal conductivity. The standard deviation of this histogram represents the uncertainty of extracted thermal conductivity associated with the phase noise, compared to the baseline measurement, where 32 points are used to fit the FDTR curve. The same procedure is applied for three different samples with a low, mid, and high value of thermal conductivity. Figure 3-12 (e-f) shows a summary of the complete analysis. Figure 3-12 (e) represents the uncertainty in thermal conductivity values with a full set of 32 data points with added noise as a function of integration time. Here, adding these noise values would typically cause a 2.1% variation with respect to the baseline FDTR measurement for 2 s and 0.3 s integration time, which exhibit very similar noise. For 0.02 s, the uncertainty increases to about 10.5% on average. Since the largest noise occurs for high frequencies, this can be somewhat mitigated by limiting the frequency range to 3 MHz (24 frequency data points), reducing uncertainty to 9.3% for 0.02 s integration time. Figure 3-12 (f) shows the same graph using only six logarithmically spaced points of the FDTR curve. It is noted that these six points can be measured simultaneously. This added noise causes uncertainty of 5.7% with respect to the baseline FTDR measurement for 2 s and 0.3 s integration time. For 0.02 s, the uncertainty increases to about 27.9% on average. Again, this can be reduced to 19.9% by limiting the maximum frequency to 3 MHz using six logarithmically spaced frequencies, but this level of uncertainty may still not be acceptable depending on the application. However, measurements can be made in one shot over six frequencies with an integration time of 300 ms. This would ideally cut down the measurement time to be some hundreds of milliseconds, and the extracted value would be within 3.5% of the baseline measurement by limiting the maximum frequency to 3 MHz.

This minimization of measurement time could be acceptable for process monitoring on an industrial scale.

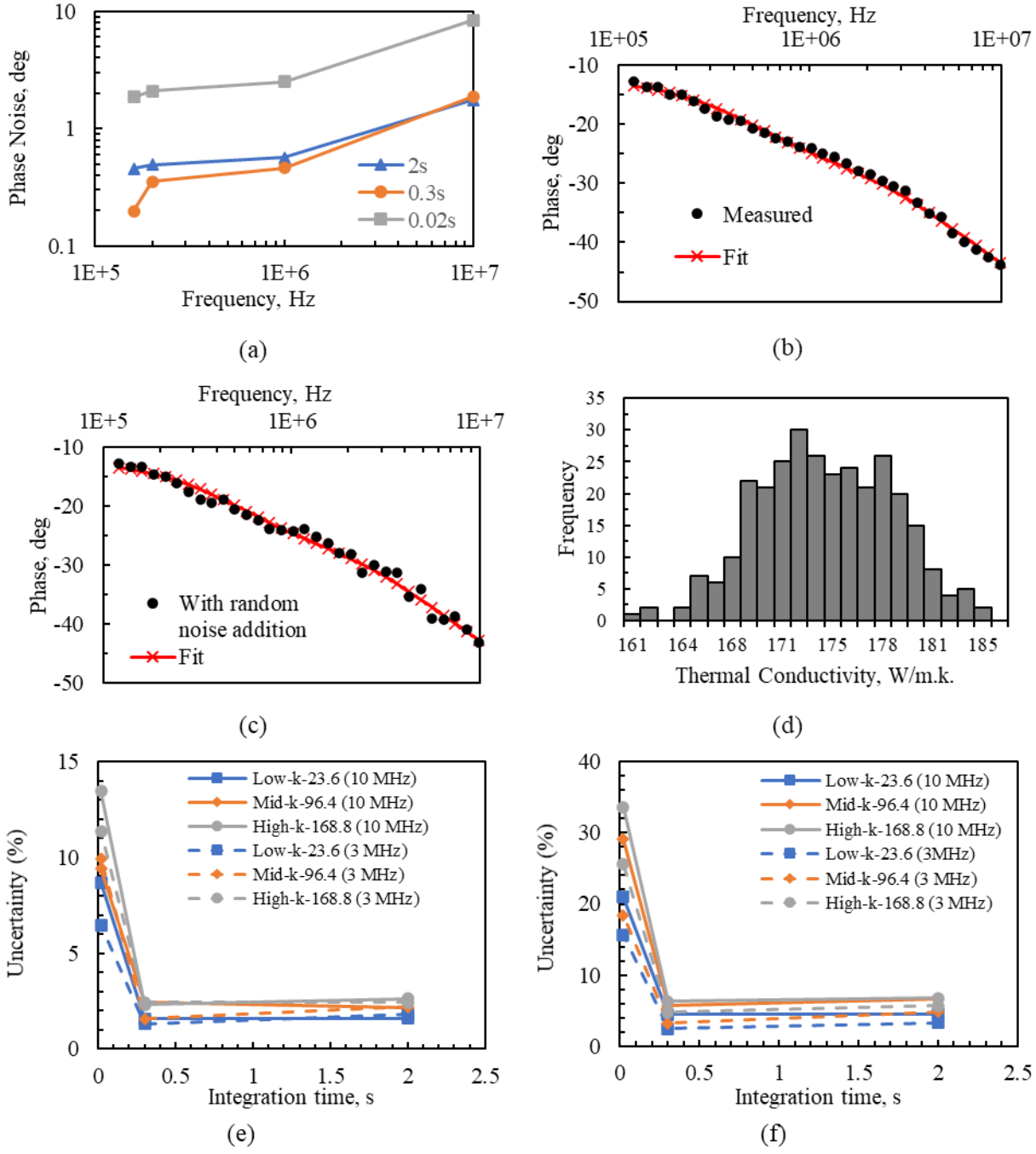

Figure 3-12: (a) Standard deviation (noise) of static measurements of phase at different modulation frequencies for different lock-in integration times. (b) Analytical model fits to the measured data of a sample with high thermal conductivity. This used 32 frequency points, which is considered as

the baseline measurement. (c) Frequency-dependent phase noise for 0.3 s integration time is added randomly to the same phase data and is fitted using the same thermal model. (d) Histogram of 300 fits for high thermal conductivity samples and 0.3 s integration time; mean and standard deviation of this distribution indicates the conductivity variations as a result of these noise addition. (e) Calculation of uncertainty of the thermal conductivity using all 32 points of the FDTR curve while adding frequency-dependent noise values up to 10 MHz and 24 points up to 3 MHz. (f) Same calculation of uncertainty using only six frequency points that are logarithmically spaced on the FTDR curve up to 10 MHz and 3 MHz.

3.4. Conclusion

To conclude, a novel, non-contact characterization, and process monitoring technique is demonstrated for printed electronics based on thermoreflectance. Different stages of intense pulsed light sintering of inkjet-printed metal nanoparticle patterns can be distinguished. The method measures thermal conductivity, which can be used to quantify electrical conductivity. Furthermore, the compatibility of this method with high-throughput production is shown by reducing measurement time to 12 seconds using only six frequency data points that are measured simultaneously. Future quantitative study could determine the spatial variability within printed rectangles. A predictive model based on Monte Carlo simulation is proposed to cut down the measurement time even further to hundreds of milliseconds with an acceptable error in measurement of 3.5% by reducing the integration time of the lock-in amplifier. Future experimental work using a smaller integration time combined with a small number of frequency data points could be undertaken to confirm the prediction.

4. Direct Writing of Stretchable Metal Flake Conductors[3]

4.1. Introduction

Stretchable and flexible electronics with elastic interconnects are critical for electronics to be compatible with wearable applications. Especially, fabricating such interconnects with printing technology promises rapid, low-cost, and mass manufacturing. Here, a novel direct-write manufacturing process is presented for a stretchable conductor using an extrusion printer and a micrometer size silver flake ink as the conductive material without expensive nanomaterials. Conductivity increases as the sintering temperature is increased but at the cost of limited stretchability. To overcome this trade-off, we place one mildly sintered line on top of a fully sintered line to create a hybrid serpentine feature. These two lines of a hybrid feature have two different stretchability-conductivity profiles, synergistically improving both the stretchability and conductivity. With this method, a maximum stretchability of 120% strain is obtained with a minimal change in resistance by a factor of 2.8. This stretchable conductor can endure more than 250 cycles of stretching and releasing under 40% strain. The aggregate electrical conductivity is in the range of $4.74*10^4$ S/cm, which is far superior to any carbon filler based printable composites.

4.2. Zigzag Lines and Effect of Angle on Stretchability

There are several ways of inducing stretchability by adopting a specific structure for inherently rigid materials. Among them, the co-planar structure on an elastomeric substrate that is designed to concentrate and release the stress is preferred for 2D printing techniques. The reason is that the other ways of improving stretchability, such as kirigami patterned, out-of-plane buckling, etc. need a printing technique with Z-axis layer deposition capability. Therefore, we fabricated zigzag lines and embedded them in an elastomeric matrix for introducing stretchability with a printable metallic ink, which is brittle in nature after being sintered. Different zigzag lines are fabricated, and their stretchability is tested and studied with the help of the optical microscope images.

Zigzag features were printed with a commercial extrusion printable silver flake ink (flexible conductor 2, Voltera Inc.) with a flake size of 3-7 μm. This ink contains as the major solvent

[3] Section 4.3 of this chapter has been published as "Direct writing of stretchable metal flake conductors: improved stretchability and conductivity by combining differently sintered materials," Flexible and Printed Electronics, 2020 with contributions from co-author G. Grau.[112]

diethylene glycol monoethyl ether acetate with mineral spirits to tune the ink's viscosity. The viscosity of the ink is in the acceptable range for extrusion printing. A commercial extrusion printer based on screw motion dispensing (Voltera V1) is used for printing zigzag lines with a nozzle size of 100 μm.

For each zigzag angle, the extrusion printer prints two zigzag lines parallelly on top of PFOTS (Trichloro(1H,1H,2H,2H-perfluorooctyl) silane) treated hydrophobic glass. Two adhesive copper (Cu) tape pieces are placed on opposite sides of the substrate to be used as electrodes during electrical measurements. Two pads are also printed on both ends of the zigzag lines. These pads are placed in such a way that they are also in contact with the Cu foil electrodes. After printing, degassed PDMS solution (Sylgard 184, silicone, base to curing agent ratio 10:1) is spin-coated on top of the glass substrate. The thickness of the PDMS layer is maintained at around 150 μmwith a spin speed of 500 RPM and spin time 30 seconds. For the thickness profile, the spin coating recipe of reference [107] is followed. PDMS deposition is followed by thermal curing at 120°C for 30 minutes to cure both the PDMS and metallic ink. In this way, the sintered metallic traces are embedded into the top layers of the PDMS surface, ensuring that the deformation of the PDMS affects the printed patterns equally.

Different angles between the arms of zigzag are studied to compare the effect of the number of troughs and crests per unit length of line on stretchability. The smaller the angle, the higher the amount of zigzagging in the same length. The uniaxial strain was measured using a 3D printed mechanical stage combined with a micromanipulator. Figure 4-1(a) and**Error! Reference source not found.**(b) represent the designed and the actual realization of this designed structure accordingly.

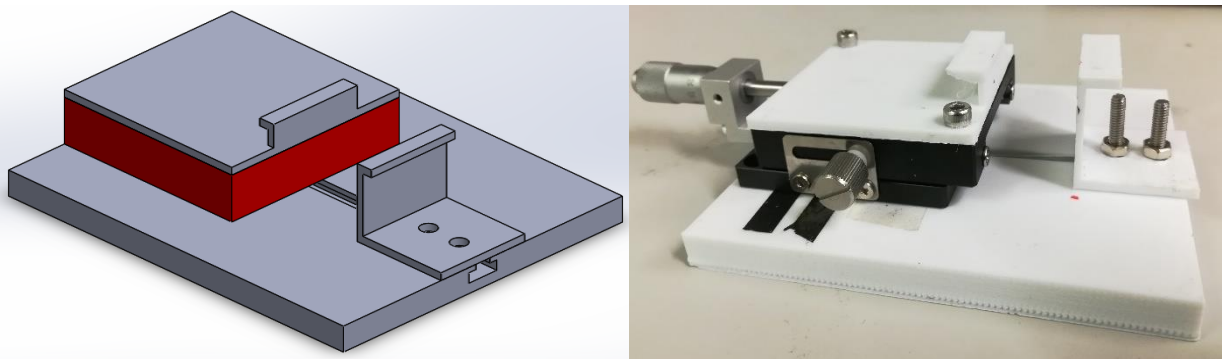

(a) (b)

Figure 4-1: (a) The designed structure of the mechanical stage for strain test. The red part is replaced with the micromanipulator, which is used to measure the strain. (b) 3D printed realization of the same design. Two arms are extended intentionally so that a firm gripping on the samples can be done with clips. One arm is stationary, and the other one is moved relative to the stationary one to create the uniaxial strain on the sample.

Zigzag patterns with different angles, ranging from 60° to 120°, are fabricated, keeping a constant arm length of 1 mm. Figure 4-2 shows the designed patterns and images of the actual printed patterns. It is noticeable that all of the features exhibit corner rounding with more deposited at the peaks and valleys. The steeper the angle is, the thicker these peaks and valleys become, and the more circular they become with decreased arm length. The printer follows the designed angles with approximately 18° of offset to the specified value.

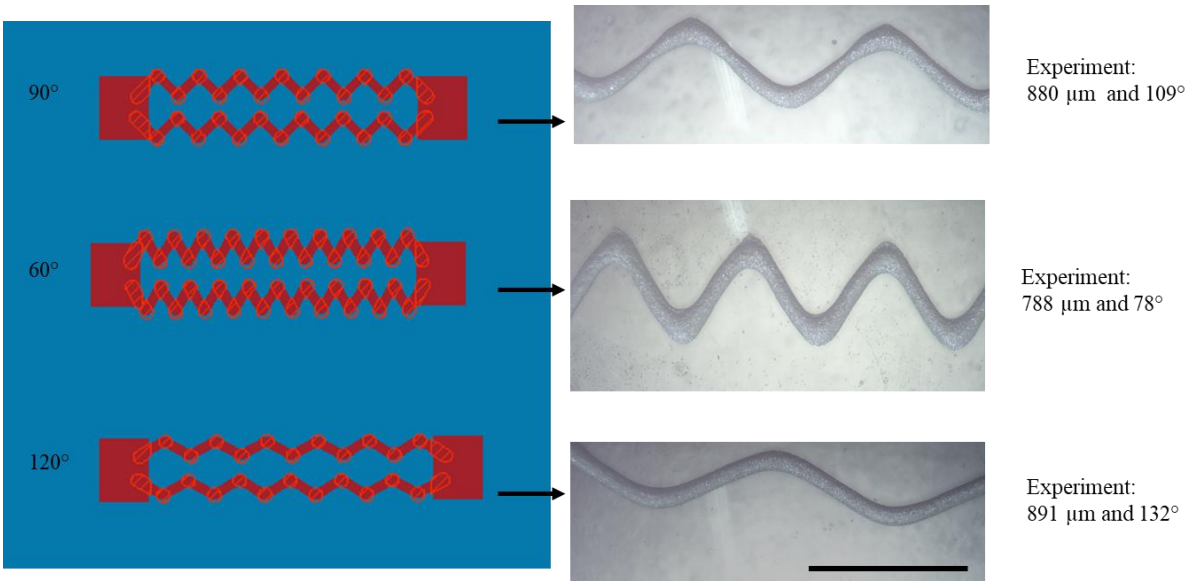

Figure 4-2: Zigzag patterns with various angles are designed (left) and fabricated (right) with a constant designed arm length. As the angles become steeper, the printed arm length decreases due to corner rounding. Scale bar represents 780 µm.

These patterns are then tested under uniaxial strain. Figure 4-3 shows a comparison between their stretchability properties. Zigzag with 120° and 90° between the arms behave similarly, they both break down with infinite resistance at 5% strain. However, the zigzag pattern with 60° has a maximum strain of 10%. The reason behind this improvement lies in the increased number of zigzag patterns per unit length compared to the 90° and 120° cases. This finding matches with a previous study [108], where improvement of stretchability is shown by increasing the frequency of the peaks and valleys.

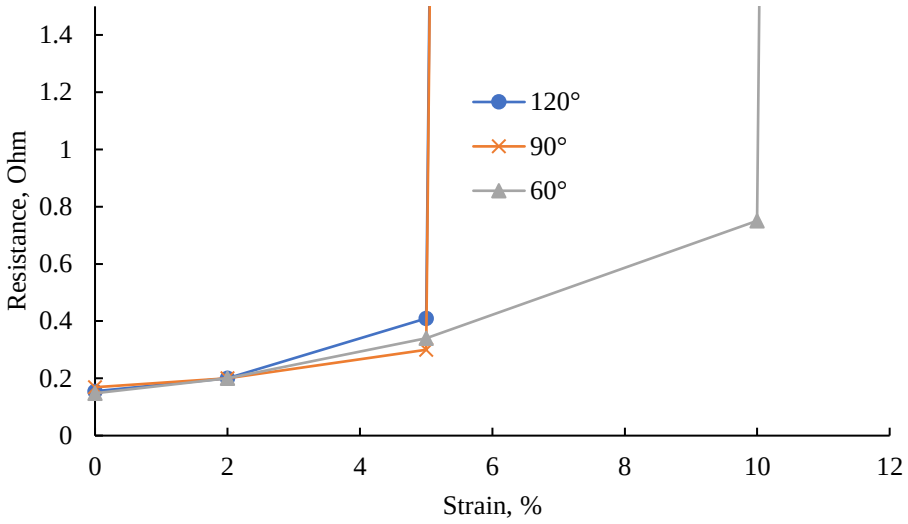

Figure 4-3: Resistance change as a function of strain. The vertical line denotes the maximum strain where the resistance becomes infinite.

In the next section, a novel fabrication method is presented with an extrusion printer to print stretchable electrodes. Instead of zigzag lines, sinusoidal tortuousness is realized as the corner can have a larger radius to reduce stress concentration that arises while stretching. The printed electrode has two layers with two different stretchability-conductivity profiles. One has low stretchability and high conductivity, and the other has the opposite profile, high stretchability, and low conductivity. Both of the layers are fabricated from the same metallic ink, which is sintered at two different temperatures. The top, less conductive, yet more stretchable line provides anti-fatigue support when the bottom line with the higher conductivity fails. Combining two layers provides a facile and low-cost route for fabricating stretchable conductors.

4.3. Effect of Sintering in Stretchability of Serpentines

Serpentine features were printed on top of PDMS with another commercial screen-printable silver flake ink (Creative Materials 120-07) with a filler flake size of 5-20 μm in a thermoplastic polyurethane matrix. The same extrusion printer, as in section 4.2, is used for printing serpentine lines with a nozzle size of 220 μm. A 0.5 mm thick layer of PDMS was deposited on hydrophobic glass using blade coating with a glass spacer. Before the thermal curing of the PDMS, two copper foil pieces are placed on opposite sides of the substrate to be used as electrodes during electrical measurements. Figure 4-4 describes the whole process, from fabricating the PDMS layer to printing on top of it.

For comparing the stretchability and conductivity, several samples were prepared with a single serpentine feature sintered at different temperatures, ranging from 30°C to 140°C for 1 hour. After printing, the same blade coating method was used to deposit another PDMS layer (1 mm thick) on top of the printed layer. We found that with increasing sintering temperature, the conductivity is increased while the stretchability is decreased. With this information, we fabricated hybrid traces consisting of two parallel layers, one mildly sintered and one fully sintered printed line. For fabricating such traces, the first printed trace remains in the printer and is sintered fully with the built-in hot plate of the printer at 140°C for 60 minutes. Then, the next pattern, which is identical to the bottom pattern, is printed on top of the fully sintered line. Two different temperatures for the thermal curing of the top lines were studied, 40°C and 60°C. The same blade coating method as before, was used to encase the printed layer with the second layer of PDMS.

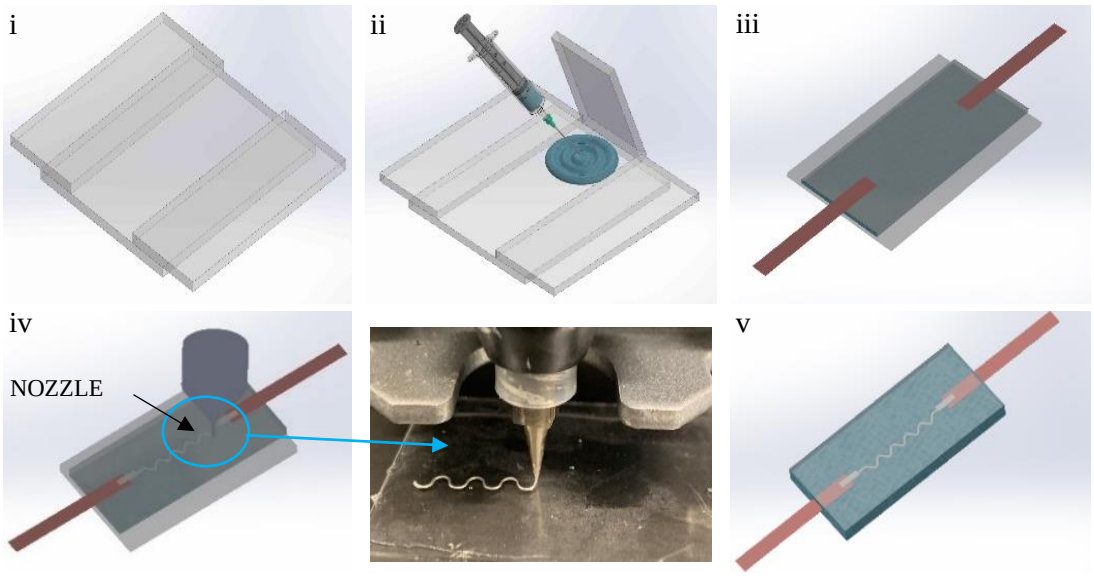

Figure 4-4: Fabrication method for one single serpentine line: (i-ii) Blade coating to deposit a 0.5 mm thick PDMS layer on hydrophobic glass. (iii) Two Cu tapes are placed on opposite sides of the cured PDMS layer. (iv) Serpentine lines with contact pads are printed on top of the PDMS. The marked area shows a photograph of the extrusion printer printing through a nozzle with an inner diameter of 220 μm. (v) Encasing with a second PDMS layer is also performed with the same blade coating method before releasing the sample from the glass.

For tensile testing, dumbbell-shaped specimens were fabricated to improve the gripping of the ends of the sample. A 3D printed die, a negative of the preferred shape, is used to cut out dumbbell-shaped specimens after encasing with the second PDMS layer. Finally, the entire stack is released from the glass holder for mechanical testing. Figure 4-5(a-c) depicts the process of producing the dumbbell-shaped specimen.

For measuring the electrical resistance of the serpentine lines, a digital multimeter (Keithley, 2100 series) was used. Conductivity was calculated from the height profiles of these lines, which was measured using stylus profilometry (Alpha-Step D-500, KLA-Tencor). The static uniaxial strain was measured using the same 3D printed mechanical stage, as described in Figure 4-1. The dynamic strain cycle was measured with a Dynamic Mechanical Analyzer (TA instrument, DHR3 with DMA Module). The surface morphology of the silver was studied for different sintering conditions using a Field Emission Gun Scanning Electron Microscope (FEG-SEM, Fisher Quanta 3D).

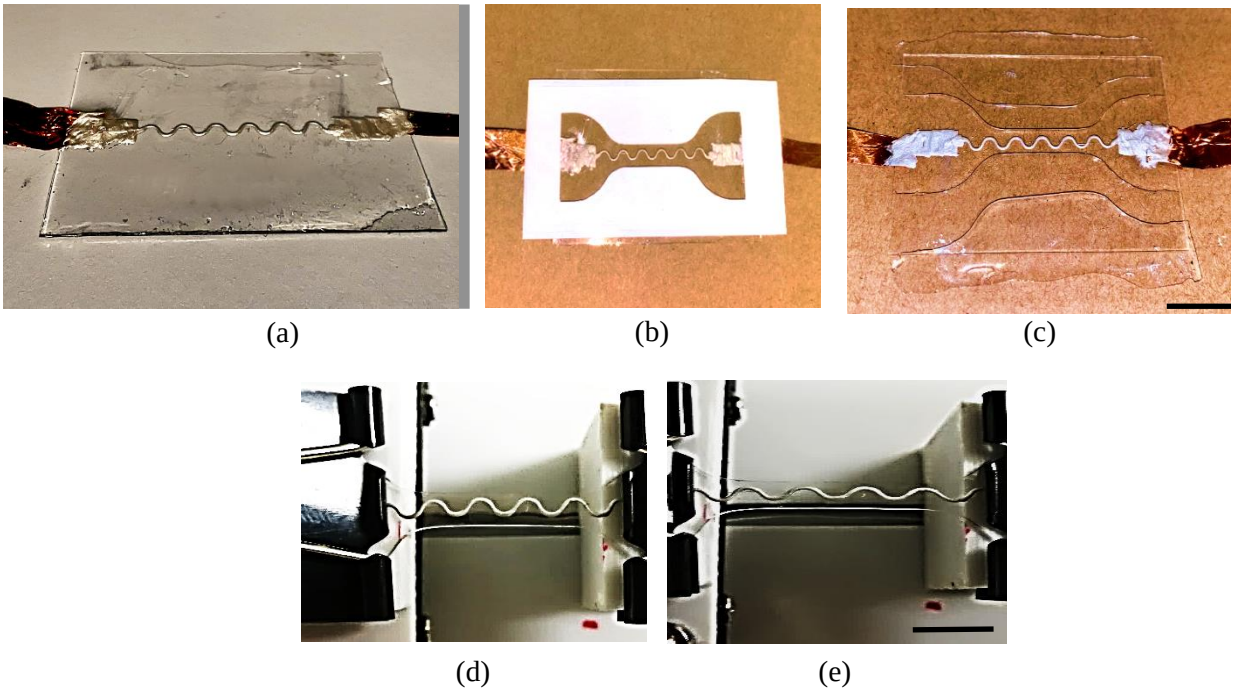

Figure 4-5: (a) Printed serpentines encased with the second PDMS layer. (b) A 3D printed die is placed on the PDMS to cut out the dumbbell shape. (c) The dumbbell-shaped sample in the middle right after cutting. The scale bar represents 15 mm. Typical printed pattern at (d) 10% strain and (e) 50% strain. The scale bar is equivalent to 10 mm.

4.3.1. Characterization of Printed Single Lines

Several serpentine lines were printed and sintered over a range of temperatures, from 30°C to 140°C for 1 hour. Moreover, one single straight line was also sintered at 140°C and stretched with uniaxial direction. The maximum strain this line can endure, before the resistance becomes infinity, is about 5%. However, for the serpentine lines, there is a decay in stretchability, while conductivity increases as the sintering temperature is increased. This is shown in Figure 4-6. From 30°C to 60°C, the conductivity gradually increases from $4.11*10^4$ S/m to $3.02*10^5$ S/m. After that, the conductivity sharply rises to $8.54*10^6$ S/m when the sintering temperature is 85°C. Beyond 85°C, the increase in electrical conductivity is minimal. The maximum conductivity, $9.74*10^6$ S/m, is found at 140°C. Several highly conductive lines are fabricated, and electrical measurements are carried out on each of these lines to find out the statistical variation. The standard deviation is within the 6% of the mentioned value, $9.74*10^6$ S/m. Conversely, the stretchability, the maximum amount of strain a specimen can endure before electrical resistance becomes infinite, exhibits the

opposite trend, declining from 160% to 45%. The sharpest decline also happens at 85°C when the conductivity increases most sharply.

To explain these changes, Scanning Electron Microscopy was performed on both an unsintered line and a line with 90°C sintering for 30 min. Figure 4-7(i) and (ii) show the surface morphology before and after sintering. From Figure 4-7(i), one can see that individual flakes are difficult to discern in the unsintered case as they are embedded in the polyurethane matrix. Conversely, Figure Figure 4-7 (ii) shows that after sintering, the flakes are more clearly visible without matrix material in between. This indicates that the continuity of the polyurethane matrix has disappeared with 90°C sintering, which exposes the silver flakes to their neighboring flakes. This phenomenon explains the dramatic increase in conductivity and decrease in stretchability at 85°C in Figure 4-6.

Moreover, the amount of solvent remained in the partially sintered line does not play a crucial role in stretchability for these lines. Printed lines were partially sintered in a vacuum oven at 40/60°C. We assume that the solvent in the printed ink would be evaporated mostly due to the long-time vacuuming. The stretchability did not change compared to the lines that are sintered at the same temperature but in ambient conditions.

Figure 4-8 shows the effect of one strain-relaxation cycle on both 140°C and 40°C sintered serpentine lines. After straining at 40% of the original length, the 140°C sintered line developed cracks at the peak and trough of the serpentines (see Figure 4-8 (i)). Conversely, even with 100% strain, the low temperature sintered serpentine only elongates in these peak and trough regions of the serpentines instead of breaking. To accommodate this elongated line after release of the strain, the material buckles out-of-plane perpendicular to the PDMS layer.

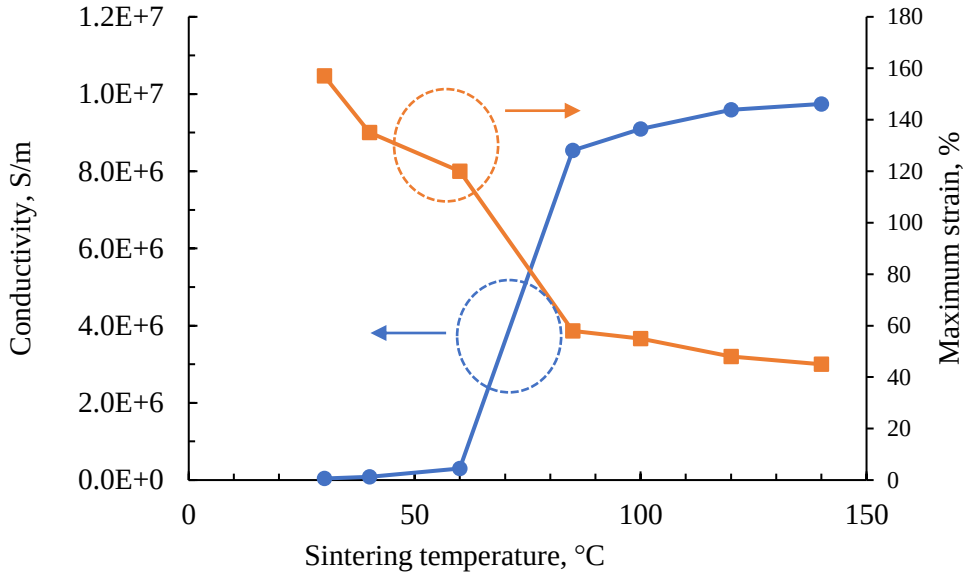

Figure 4-6: Change of electrical conductivity (blue circles) and maximum strain where resistance becomes infinite (orange squares) as a function of sintering temperature. Lines become more prone to develop cracks with increasing sintering temperature and increasing electrical conductivity.

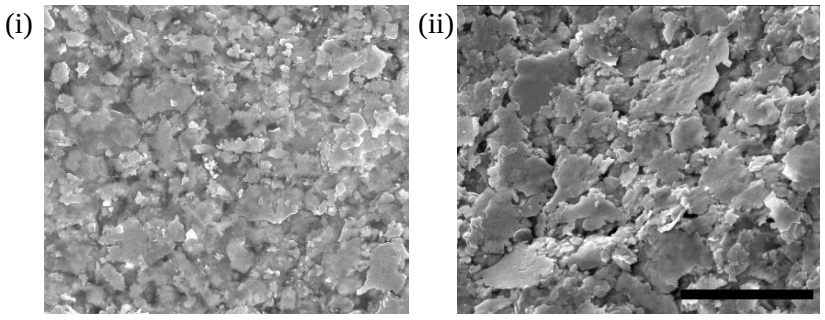

Figure 4-7: Surface morphology SEM images: (i) 40°C sintered line. A continuous matrix without clear boundaries between individual flakes is found. (ii) 90°C sintered line. Clear flakes without a matrix disrupting current paths can be observed. The scale bar indicates 10 µm.

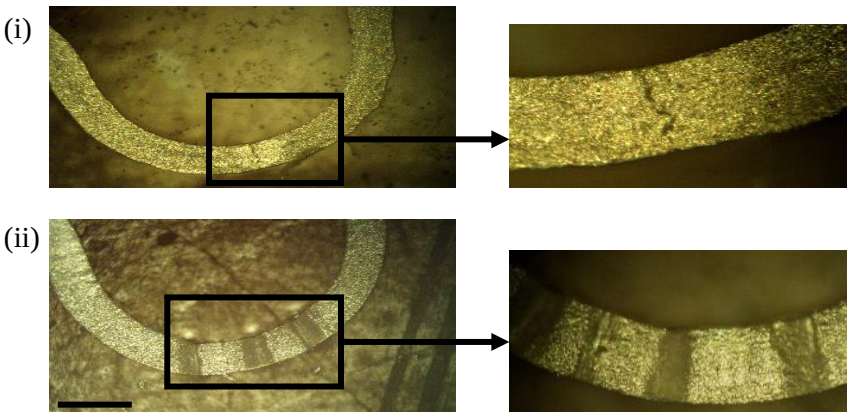

Figure 4-8: Optical micrographs of silver serpentines after stretching: (i) 140°C sintered line developed crack with only 40% strain, zoomed area shows the nature of the crack (ii) 40°C sintered line stretched without cracks to accommodate 100% strain and developed buckling after release, zoomed area shows the upward deformation of the line due to buckling. The scale bar indicates 500 µm.

4.3.2. Characterizations of Hybrid Lines

In order to overcome the trade-off between conductivity and stretchability, we conceived a hybrid pattern by printing two serpentine lines on top of each other. The two lines are sintered at opposite ends of the temperature range studied here. For example, one line is sintered at 140°C, and the other is sintered at 40°C or 60°C. As strain increases, the cracks in the high temperature sintered line will be bridged by the low temperature sintered line, whose conductivity is lower but with higher stretchability than the fully sintered line. In the lower strain region (0-40% strain), the conductivity will be determined by the fully sintered line, whereas the low temperature sintered line will dominate the stretchability in the higher strain range (40%-120%). Figure 4-9 (a) presents resistance normalized by unstrained resistance R_0 as a function of uniaxial strain for single lines sintered at different temperatures as well as hybrid lines. From this figure, hybrid lines with 40°C sintered top face a sharp transition in normalized resistance when the strain reaches around 45%; however, unlike the fully sintered single line, it is not completely broken and can still conduct current. This transition can be explained by the fact that among the two lines in a hybrid feature, the 140°C sintered line exhibits cracks while the line on top of it, the low temperature sintered line, remains intact. During the electrical resistance measurement, the current follows the unbroken top line which is more resistive but works as a bridge to pass over the cracks. The hybrid line with 60°C sintered top exhibits a much less pronounced transition at 45% strain due to its superior

conductivity. In terms of absolute resistance, hybrid lines with both 40°C and 60°C sintered top exhibit resistance close to fully sintered single lines (see Figure 4-9 (b)).

Cracks are generated at the peak of each serpentine's half-cycle for a 140°C sintered line (referring to Figure 4-8(c)). Along the line, these cracks keep adding resistance to the total resistance of the hybrid line, owing to the more resistive top line. We modeled the total resistance of a hybrid serpentine line, which explains the resistance increase during the crack formation. Figure 4-9 (c) shows the top and side view of a hybrid line with the modeled resistance for both lines. We know the conductivity of a single line sintered at different temperatures from Figure 4-9 (a). Knowing the crack length, we can calculate the resistance that is added by the bridge of the 40/60°C sintered line. Other than the cracked part, the resistance of the remaining hybrid line R` is calculated by the parallel combination of the two lines (see equation 4.1). Here, R1 and R2 are the resistance of the 40/60°C sintered line and the sintered line, respectively. The length is that of one half-cycle from one crack to the next crack. We measured the crack length, which is the length of the 40/60°C sintered line bridging the crack and responsible for the extra resistance R``. The total resistance for one crack and one-half cycle is calculated by the series combination of R` and R`` (see equation 4.2).

$$\frac{1}{R'} = \frac{1}{R_1} + \frac{1}{R_2} \qquad \text{Eq-4.1}$$

$$R = R` + R`` \qquad \text{Eq-4.2}$$

The total resistance of the serpentine is calculated by multiplying the total number of half cycle-crack pairs with R (see the result in Figure 4-9 (d)). For the case of a hybrid feature with a 40°C line, a total of 11 cracks add 0.23 Ω, coming from a total of five full cycles of the serpentine. This amounts to an increase in normalized resistance to about 6 at around 45% strain, where the fully sintered line develops cracks. This calculated resistance jump from modeling compares well with the measured resistance jump, and the modeled and measured resistance follow the same trend with strain, although the model somewhat underestimates the final resistance. For the case of a hybrid feature with a 60°C line, these 11 cracks add 0.0238 Ω. This value contributes to the normalized resistance jump to 1.72 at 45% strain, whereas the measured value is 1.71. Hybrid lines with 40°C top fail at 140% strain and 60°C hybrid lines at 120%. Thus, hybrid lines of fully sintered and partially sintered silver flakes can achieve a stretchable conductor combining low

resistance and good stretchability. In terms of total stretchability and conductivity, this novel stretchable conductor is among the highest performance results reported for printed stretchable composites with a special structure that facilitates stretchability and it rivals liquid metals. [25]

There are three strain regimes for such hybrid stretchable conductors: the low strain regime up to the failure point of the fully sintered layer (40%), the medium strain regime up to the failure point of the less sintered layer (120% for 60 °C hybrid), and the high strain regime where both layers have failed, and conduction is lost. The best strain regime to operate in depends on the application. For applications that are very sensitive to the resistance of the conductor, for example, sensitive measurements, it would be advisable to stay within the low strain regime where resistance only increases by 25% over 40% strain for the 60 °C hybrid line. Beyond this strain, resistance undergoes a jump. Such applications likely would not operate in the medium strain regime continuously but may still benefit from the higher ultimate strain offered by the hybrid preventing catastrophic failure in case of large short-term deformations. However, it should be noted that even with this jump, the overall resistance is still very low. For example, a line that is 10 cm long in the unstretched state would remain well below 1 Ω, even at 120% strain. At that strain, the sheet resistance is in the range of 4 milli Ω/sq^{-1}. Therefore, many circuits could be designed such that the resistance of the stretchable conductor is always negligible relative to the resistance of other devices, for example, to drive a light-emitting diode.

Figure 4-10 (a) shows the normalized resistance of the hybrid structure with a 60°C top line for repetitive cycles of 40% strain and a strain rate of 100 μm/s. The resistance gradually increases to about three times of the original resistance over 250 cycles. Notably, the resistance returns to its original level after the release of strain, demonstrating the excellent reversible electromechanical nature of the material. Figure 4-10 (b) shows a few cycles of stretching and releasing cycles with a constant strain of 40%. The red dashed line shows the applied strain cycle. The change of R/R0 generally follows the applied strain but also exhibits time-dependent behavior. Initially, R/R0 increases/decreases fast as strain is ramped up/down, which can be attributed to geometrical changes as well as the increasing distance between neighboring silver flakes as strain increases. As the maximum or minimum strain is approached, the change of R/R0 slows down. The resistance peaks before maximum strain are reached, denoted by point 1. This occurs because of the stress relaxation of the PDMS film and probably also of the mildly cured thermoplastic ink. This stress relaxation helps the flakes to realign, find new percolation networks, and causes the resistance to

decrease from point 1 to 2. Another small peak in resistance can be observed from point 2 to 3 when the strain is released before resistance decreases. Such stress relaxation behavior is common in literature for stretchable conductors on PDMS, and both peaks have been observed before, for example, in [109], [110].

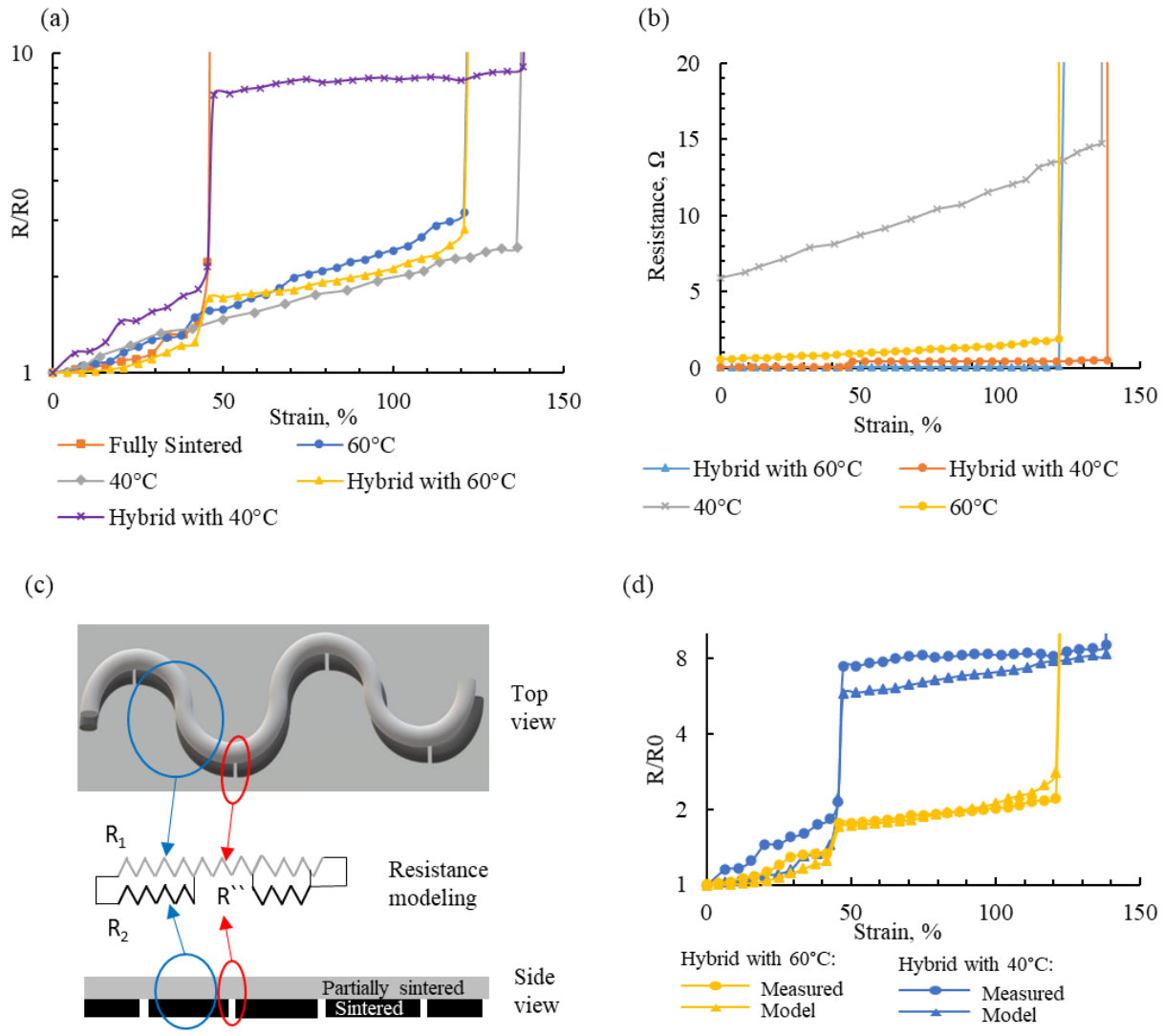

Figure 4-9: (a) Normalized resistance of single and hybrid lines as a function of strain (log scale to visualize differences for small resistance changes). The hybrid lines, especially with 60°C, can endure a much larger strain range with little change in normalized resistance. (b) The absolute resistance of single and hybrid lines. Although 40°C and 60°C single lines are more stretchable, they have higher resistance. Conversely, hybrid lines exhibit resistance close to fully sintered

single lines. (c) Resistance model with top view and side view of the hybrid line. The silver line represents the 40°C/60°C sintered top line, the black line represents the fully sintered bottom line. The blue circled region in both top view and side view corresponds to R_1 and R_2 in the resistance modeling, whereas the red circled region represents the crack corresponding to R``. (d) Comparison of the normalized resistance increase predicted by the model and measured experimentally for hybrid lines with 40°C/60°C sintered top line. The 60°C sintered line exhibits better agreement between model and measurement and a lower resistance increase.

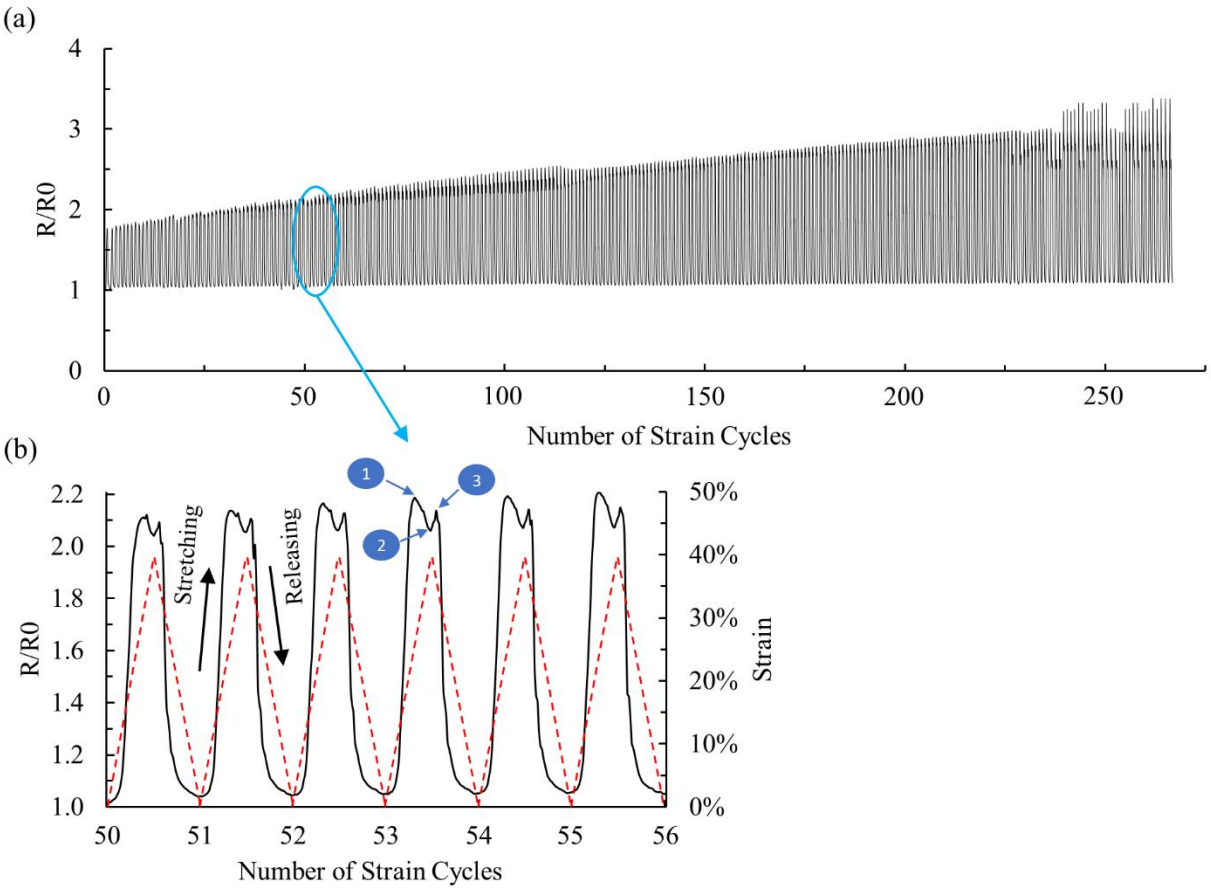

Figure 4-10: (a) Normalized resistance of a hybrid feature with 60°C top line during repetitive strain and relaxation cycles, with a peak strain value of 40%. The peak resistance in each cycle gradually increases, whereas the change in base value is negligible. (b) Normalized resistance for a few cycles of loading and unloading from 0% to 40% strain.

Long term storage test for these hybrid stretchable electrodes is done to see if there is any declination of stretchability with time. Figure 4-11 shows the relation between the storage time and the highest stretchability of hybrid lines with 60°C top line. Within three months, the highest stretchability declined only by 16% of the freshly prepared line.

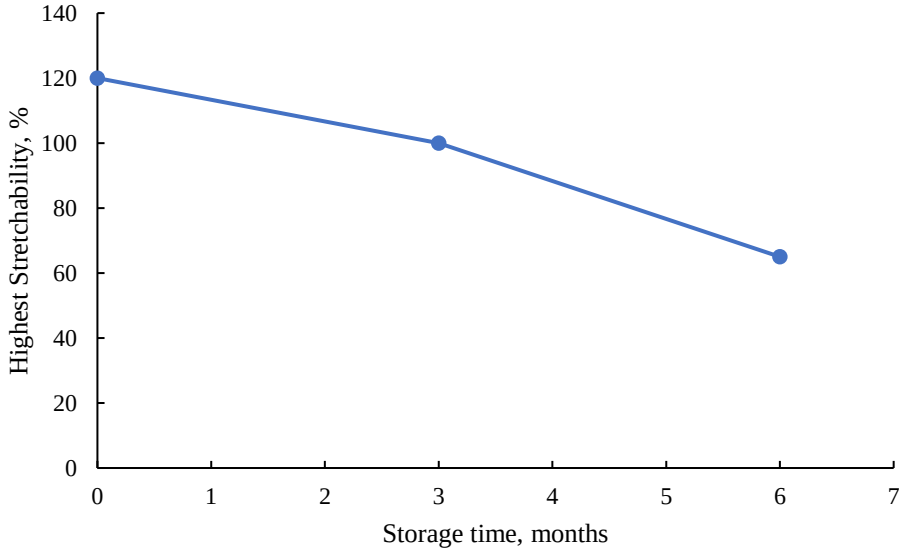

Figure 4-11: Long term storage test vs. highest stretchability of the hybrid samples. Stretchability declines hardly with the timespan of three months.

4.3.3. Tri-layer Modeling

Modeling was done to determine whether adding a third layer with different sintering conditions would further improve the performance of the hybrid structure. Two different cases were modeled, both with a layer sintered at 140°C and one at 40°C and a third layer in between at an intermediate temperature. The results are shown in Figure 4-12. If the third layer is sintered at 100°C, the benefit is very marginal because the 100°C layer is only marginally more stretchable than the 140°C layer (55% vs. 45% strain). Having a mid-layer that is almost sintered only contributes by lowering the resistance in the low strain regime. After 55%, the R/R0 value rises to 10 times the resistance of the unstrained state, which is a bigger relative increase than the two-layer case with 40°C and 140°C because the unstrained resistance is lower with three layers. If the third layer is sintered at 60°C, the benefit would again be marginal. The behavior is very similar to the 60°C-140°C two-layer structure up to the failure point of the 60°C layer (120% strain). Beyond this strain, the 40°C

sintered layer dominates, which means resistance increases sharply, and ultimate strain is increased to the failure point of the 40°C sintered layer of 140%.

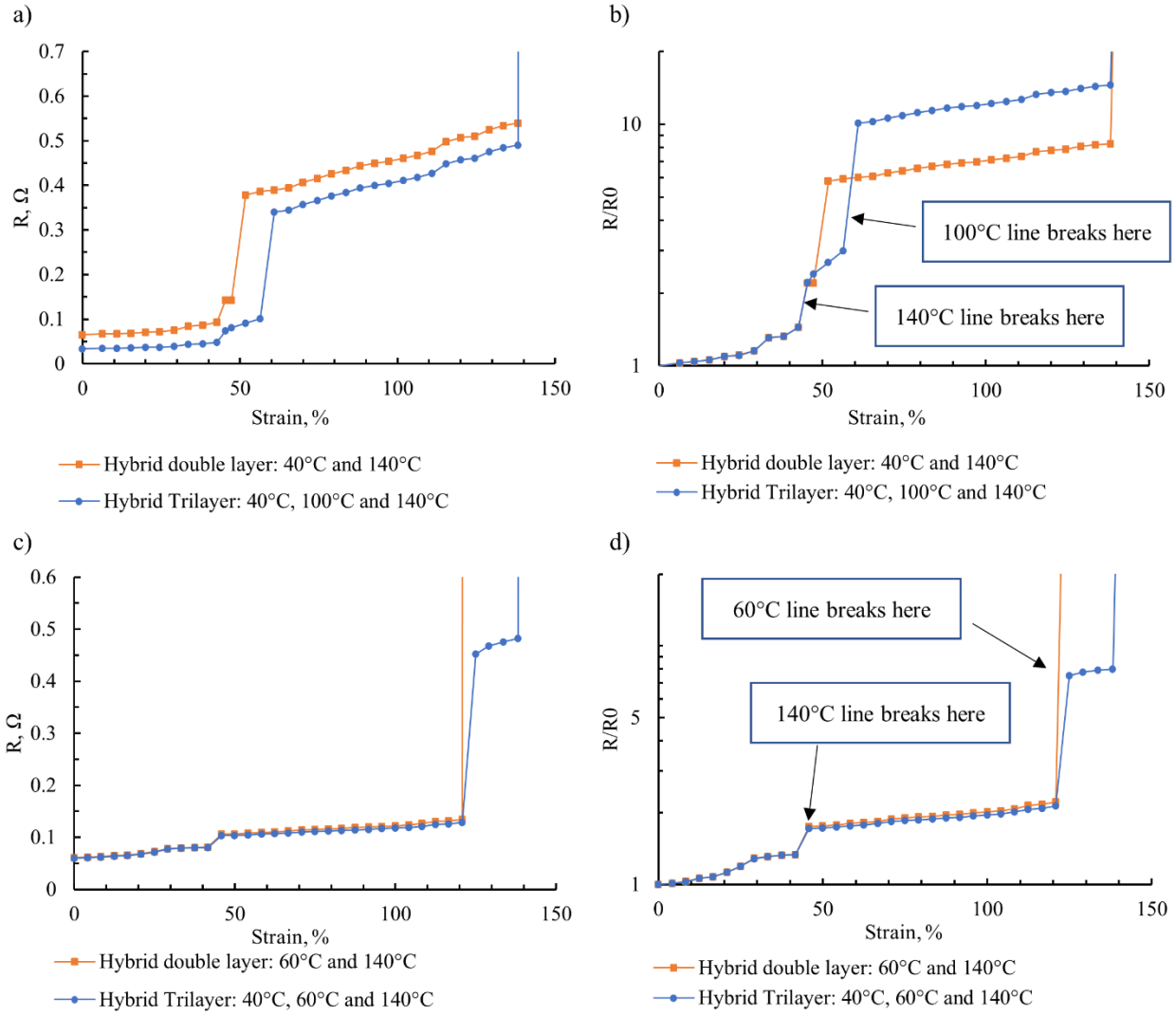

Figure 4-12: Modeled resistance for two different hybrid structures with three layers. Both have a 40ºC and a 140ºC layer. a) Absolute resistance when the third layer is sintered at 100ºC. The structure is only marginally improved over a two-layer structure with a 40ºC and a 140ºC layer. b) Normalized resistance for the same structure as in a). c) Absolute resistance when the third layer is sintered at 60ºC. The structure is only marginally improved over a two-layer structure with a 60ºC and a 140ºC layer. d) Normalized resistance for the same structure as in c).

One could consider further combinations that might be beneficial for a particular application. An experimental challenge would be that sintering the third layer with 40°C or 60°C could affect the

mid-layer, which is also not fully sintered. Further work is needed to study this effect and potentially overcome it with alternative sintering strategies such as photonic annealing.

4.4. Conclusion

In summary, the role of two different parameters, angles between zigzag patterns and sintering conditions for serpentine lines, for stretchability are studied. A new method is presented using sintering optimization to create highly conductive stretchable interconnects. There exists a trade-off between conductivity and stretchability for different sintering temperatures of the silver ink. A hybrid serpentine line is demonstrated here by stacking two lines vertically that are sintered at different temperatures. Due to the difference in sintering, one line has more stretchability with less conductivity while the other line has more conductivity and less stretchability. Their different stretchability-conductivity profiles complement each other's properties under strain. While the fully sintered line provides increased overall conductivity, the less sintered line provides more stretchability to the hybrid feature. With this method, hybrid serpentine lines can conduct even at 120% strain with a relative increase in resistance of 2.8 times compared to the unstrained resistance.

5. Conclusion and Future Work

In this chapter, a summary of all the conclusions from different chapters is provided. Then, future work and an outlook are suggested based on the works in this thesis.

5.1. Conclusions

In this thesis, frequency-domain thermoreflectance (FDTR) is explored as a non-contact method of characterizing and monitoring different sintering stages of printable metal nanoparticle films. Then, a novel method for stretchable electrode fabrication is presented as an application of tailored sintering.

In the second chapter, FDTR is used for measuring the thermal conductivity of solution-processed printable silver nanoparticles films. Unlike the traditional FDTR setup, no additional transducer layer is deposited onto the sample surface, which simplifies the measurement method. Thermal conductivity measured from FDTR agrees well with thermal conductivity measured from electrical conductivity measurements by Wiedemann-Franz law. In the low temperature sintered regime, thermal conductivity is more accurately measured by FDTR than thermal conductivity converted from Wiedemann-Franz law due to the phononic contribution. Therefore, thermal modeling of metal nanoparticles and sintering process optimization for printed electronics could be more accurate if one captures thermal conductivity from FDTR.

Next, the same FDTR setup is integrated into printed electronics processes as a high-speed sintering monitoring tool. Alternative high-speed sintering tools such as laser and intense pulsed light sintering are used for post-processing, and their sintering stages are identified with the aid of FDTR. Furthermore, FDTR is configured to decrease the measurement time to 12 s by choosing a small number of measurement frequencies (six) instead of a full frequency sweep and measuring them simultaneously using six modulators in the lock-in amplifier. Finally, a Monte Carlo simulation was performed to predict the possibility of further reducing measurement time by reducing the integration time of the lock-in amplifier for ultra-fast measurements.

The understanding of the sintering mechanism provides us a way of fabricating stretchable electrodes in a facile way. A metal flake ink’s sintering stages are studied, and it was found that there are different regimes of electromechanical properties depending on the sintering temperature. It is found that the conductivity is increased by increasing sintering temperature at the expense of stretchability. Therefore, two layers, one is low temperature sintered, and another is high

temperature sintered, are used to provide a synergistic improvement of both conductivity and stretchability.

5.2. Future Works

There are several areas to be expanded based on this thesis's conclusions. First of all, FDTR can be used to measure the role of thermal conductivity for different repetition rates of the alternative sintering technologies such as pulsed laser or intense flashlight sintering. Increased repetition rate can decrease the thermal penetration in the Z-axis in such a way that the sintering process affects the heat-vulnerable substrates in a limited manner. These insights could be an effective means to model the heat propagation dynamics in both printed features to substrate and feature to feature cases. Secondly, FDTR measurement time is predicted to decrease down to milliseconds by lowering the integration time. Future work can be undertaken on combining both the shorter integration time and a smaller subset of frequency data points to confirm this prediction.

There is room for future improvement for the stretchable electrode work. Techniques such as thermogravimetric analysis (TGA) combined with X-ray photoelectron spectroscopy (XPS) could be performed on differently sintered material for a mechanistic study of the sintering process of metal flake inks. Especially, how the disruption of the thermoplastic polyurethane matrix creates the percolation network between flakes needs to be studied. More comprehensive modeling of the hybrid lines' resistance change with strain could consider the materials' mechanical properties and could use an in-situ measurement of the deformation. The effect of serpentine line thickness, width, and even the amount of tortuousness on stretchability is one of the crucial areas of investigation for such stretchable electrodes [111] [108]. These studies can be done for this material and novel fabrication scheme as well. Furthermore, our proposed FDTR can be used to optimize the sintering condition for this metal flake in terms of thermal conductivity. Additionally, for conceiving the trilayer as a hybrid layer poses an experimental problem with traditional thermal baking. For a case of one 40°C (top), one 60°C (mid), and one 140°C (bottom) sintered layer, the sintering of the 40°C layer will alter the electromechanical properties of the mid 60°C layer if the heat comes from the bottom hotplate. Therefore, novel sintering tools such as IPL or laser sintering, providing heat only to the top layer, could solve this problem.

References

[1] J. Perelaer *et al.*, "Printed electronics: The challenges involved in printing devices, interconnects, and contacts based on inorganic materials," *J. Mater. Chem.*, vol. 20, no. 39, pp. 8446–8453, 2010.

[2] A. C. Arias, J. D. MacKenzie, I. McCulloch, J. Rivnay, and A. Salleo, "Materials and applications for large area electronics: Solution-based approaches," *Chem. Rev.*, 2010.

[3] P. F. Moonen, I. Yakimets, and J. Huskens, "Fabrication of transistors on flexible substrates: From mass-printing to high-resolution alternative lithography strategies," *Adv. Mater.*, vol. 24, no. 41, pp. 5526–5541, Nov. 2012.

[4] G. Grau, R. Kitsomboonloha, S. L. Swisher, H. Kang, and V. Subramanian, "Printed transistors on paper: Towards smart consumer product packaging," *Adv. Funct. Mater.*, 2014.

[5] C. Wang *et al.*, "High performance thin film transistors based on regioregular poly(3-dodecylthiophene)-sorted large diameter semiconducting single-walled carbon nanotubes," *Nanoscale*, vol. 5, no. 10, pp. 4156–4161, May 2013.

[6] Y. Y. Noh, X. Cheng, H. Sirringhaus, J. I. Sohn, M. E. Welland, and D. J. Kang, "Ink-jet printed ZnO nanowire field effect transistors," *Appl. Phys. Lett.*, vol. 91, no. 4, p. 043109, Jul. 2007.

[7] J. J. Schneider *et al.*, "A printed and flexible field-effect transistor device with nanoscale zinc oxide as active semiconductor material," *Adv. Mater.*, vol. 20, no. 18, pp. 3383–3387, Sep. 2008.

[8] B. J. Worfolk *et al.*, "Ultrahigh electrical conductivity in solution-sheared polymeric transparent films," *Proc. Natl. Acad. Sci. U. S. A.*, vol. 112, no. 46, pp. 14138–14143, Nov. 2015.

[9] M. S. Rahman, M. Rahman, S. Pisana, and G. Grau, "Effect of sintering conditions on the thermal properties of printable metal nanoparticle ink studied by thermoreflectance," 2019, p. 28.

[10] Y. H. Yoon, S.-M. Yi, J.-R. Yim, J.-H. Lee, G. Rozgonyi, and Y.-C. Joo, “Microstructure and electrical properties of high power laser thermal annealing on inkjet-printed Ag films,” *Microelectron. Eng.*, vol. 87, no. 11, pp. 2230–2233, Nov. 2010.

[11] R. Abbel *et al.*, “Photonic flash sintering of silver nanoparticle inks: a fast and convenient method for the preparation of highly conductive structures on foil,” *MRS Commun.*, vol. 2, no. 4, pp. 145–150, Dec. 2012.

[12] P. H. Lau *et al.*, “Fully printed, high performance carbon nanotube thin-film transistors on flexible substrates,” *Nano Lett.*, vol. 13, no. 8, pp. 3864–3869, Aug. 2013.

[13] G. Grau and V. Subramanian, “Dimensional scaling of high-speed printed organic transistors enabling high-frequency operation,” *Flex. Print. Electron.*, vol. 5, no. 1, p. 014013, Mar. 2020.

[14] H. Hannebauer, T. Dullweber, T. Falcon, and R. Brendel, “Fineline printing options for high efficiencies and low Ag paste consumption,” in *Energy Procedia*, 2013, vol. 38, pp. 725–731.

[15] B. Derby, “Inkjet Printing of Functional and Structural Materials: Fluid Property Requirements, Feature Stability, and Resolution,” *Annu. Rev. Mater. Res.*, vol. 40, no. 1, pp. 395–414, Jun. 2010.

[16] D. Jang, D. Kim, and J. Moon, “Influence of fluid physical properties on ink-jet printability,” *Langmuir*, vol. 25, no. 5, pp. 2629–2635, Mar. 2009.

[17] Z. Du, Y. Lin, R. Xing, X. Cao, X. Yu, and Y. Han, “Controlling the polymer ink’s rheological properties and viscoelasticity to suppress satellite droplets,” *Polymer (Guildf).*, vol. 138, pp. 75–82, Feb. 2018.

[18] D. Pesach and A. Marmur, “Marangoni Effects in the Spreading of Liquid Mixtures on a Solid,” *Langmuir*, vol. 3, no. 4, pp. 519–524, Jul. 1987.

[19] R. Abunahla, M. S. Rahman, P. Naderi, and G. Grau, “Improved Inkjet-Printed Pattern Fidelity: Suppressing Bulges by Segmented and Symmetric Drop Placement,” *J. Micro Nano-Manufacturing*, Feb. 2020.

[20] A. Mahajan, C. D. Frisbie, and L. F. Francis, “Optimization of aerosol jet printing for

high-resolution, high-aspect ratio silver lines," *ACS Appl. Mater. Interfaces*, vol. 5, no. 11, pp. 4856–4864, Jun. 2013.

[21] Z. Cui, *Printed electronics : materials, technologies and applications*. .

[22] M. Singh, H. M. Haverinen, P. Dhagat, and G. E. Jabbour, "Inkjet Printing-Process and Its Applications," 2008.

[23] N. J. Wilkinson, M. A. A. Smith, R. W. Kay, and R. A. Harris, "A review of aerosol jet printing—a non-traditional hybrid process for micro-manufacturing," *Int. J. Adv. Manuf. Technol.*, vol. 105, no. 11, pp. 4599–4619, Dec. 2019.

[24] J. U. Park *et al.*, "High-resolution electrohydrodynamic jet printing," *Nat. Mater.*, vol. 6, no. 10, pp. 782–789, Aug. 2007.

[25] D. F. Fernandes, C. Majidi, and M. Tavakoli, "Digitally printed stretchable electronics: A review," *Journal of Materials Chemistry C*, vol. 7, no. 45. Royal Society of Chemistry, pp. 14035–14068, 2019.

[26] Q. Huang and Y. Zhu, "Printing Conductive Nanomaterials for Flexible and Stretchable Electronics: A Review of Materials, Processes, and Applications," *Adv. Mater. Technol.*, vol. 4, no. 5, p. 1800546, May 2019.

[27] B. Y. Ahn *et al.*, "Omnidirectional printing of flexible, stretchable, and spanning silver microelectrodes," *Science (80-.).*, vol. 323, no. 5921, pp. 1590–1593, Mar. 2009.

[28] D. V. Leff, P. C. Ohara, J. R. Heath, and W. M. Gelbart, "Thermodynamic control of gold nanocrystal size: Experiment and theory," *J. Phys. Chem.*, vol. 99, no. 18, pp. 7036–7041, 1995.

[29] S. Magdassi, M. Grouchko, and A. Kamyshny, "Copper Nanoparticles for Printed Electronics: Routes Towards Achieving Oxidation Stability," *Materials (Basel).*, vol. 3, no. 9, pp. 4626–4638, Sep. 2010.

[30] S. Wünscher, R. Abbel, J. Perelaer, and U. S. Schubert, "Progress of alternative sintering approaches of inkjet-printed metal inks and their application for manufacturing of flexible electronic devices," *Journal of Materials Chemistry C*, vol. 2, no. 48. Royal Society of Chemistry, pp. 10232–10261, 28-Dec-2014.

[31] J. Mei, M. R. Lovell, and M. H. Mickle, “Formulation and processing of novel conductive solution inks in continuous inkjet printing of 3-D electric circuits,” *IEEE Trans. Electron. Packag. Manuf.*, vol. 28, no. 3, pp. 265–273, Jul. 2005.

[32] A. Kamyshny, “Metal-based Inkjet Inks for Printed Electronics,” *Open Appl. Phys. J.*, vol. 4, no. 1, pp. 19–36, Mar. 2011.

[33] B. Ingham, T. H. Lim, C. J. Dotzler, A. Henning, M. F. Toney, and R. D. Tilley, “How Nanoparticles Coalesce: An in Situ Study of Au Nanoparticle Aggregation and Grain Growth,” *Chem. Mater.*, vol. 23, no. 14, pp. 3312–3317, Jul. 2011.

[34] S. K. Volkman, S. Yin, T. Bakhishev, K. Puntambekar, V. Subramanian, and M. F. Toney, “Mechanistic Studies on Sintering of Silver Nanoparticles - Chemistry of Materials (ACS Publications),” 2011.

[35] V. N. Richards, N. P. Rath, and W. E. Buhro, “Pathway from a molecular precursor to silver nanoparticles: The prominent role of aggregative growth,” *Chem. Mater.*, vol. 22, no. 11, pp. 3556–3567, Jun. 2010.

[36] Y. Rosen, R. Marrach, V. Gutkin, and S. Magdassi, “Thin Copper Flakes for Conductive Inks Prepared by Decomposition of Copper Formate and Ultrafine Wet Milling,” *Adv. Mater. Technol.*, vol. 4, no. 1, p. 1800426, Jan. 2019.

[37] D. Lu, Q. K. Tong, and C. P. Wong, “A study of lubricants on silver flakes for microelectronics conductive adhesives,” *IEEE Trans. Components Packag. Technol.*, vol. 22, no. 3, pp. 365–371, 1999.

[38] J. Niittynen, R. Abbel, M. Mäntysalo, J. Perelaer, U. S. Schubert, and D. Lupo, “Alternative sintering methods compared to conventional thermal sintering for inkjet printed silver nanoparticle ink,” *Thin Solid Films*, vol. 556, pp. 452–459, Apr. 2014.

[39] J. M. Crowther and J. P. S. Badyal, “Cold Plasma Metallization of Supported Metal Salt Layers,” *Aust. J. Chem.*, vol. 65, no. 8, p. 1139, Sep. 2012.

[40] V. Bromberg, S. Ma, F. D. Egitto, and T. J. Singler, “Highly conductive lines by plasma-induced conversion of inkjet-printed silver nitrate traces,” *J. Mater. Chem. C*, 2013.

[41] K. S. Kim, J. O. Bang, Y. H. Choa, and S. B. Jung, “The characteristics of Cu nanopaste

sintered by atmospheric-pressure plasma," *Microelectron. Eng.*, vol. 107, pp. 121–124, Jul. 2013.

[42] I. Reinhold *et al.*, "Argon plasma sintering of inkjet printed silver tracks on polymer substrates," *J. Mater. Chem.*, vol. 19, no. 21, pp. 3384–3388, May 2009.

[43] S. Ma, V. Bromberg, L. Liu, F. D. Egitto, P. R. Chiarot, and T. J. Singler, "Low temperature plasma sintering of silver nanoparticles," *Appl. Surf. Sci.*, vol. 293, pp. 207–215, Feb. 2014.

[44] A. Denneulin, A. Blayo, C. Neuman, and J. Bras, "Infra-red assisted sintering of inkjet printed silver tracks on paper substrates," *J. Nanoparticle Res.*, vol. 13, no. 9, pp. 3815–3823, Sep. 2011.

[45] M. Cherrington, T. C. Claypole, D. Deganello, I. Mabbett, T. Watson, and D. Worsley, "Ultrafast near-infrared sintering of a slot-die coated nano-silver conducting ink," *J. Mater. Chem.*, vol. 21, no. 21, pp. 7562–7564, Jun. 2011.

[46] R. Abbel *et al.*, "Photonic flash sintering of silver nanoparticle inks: A fast and convenient method for the preparation of highly conductive structures on foil," *MRS Commun.*, vol. 2, no. 4, pp. 145–150, 2012.

[47] R. Lesyuk, W. Jillek, Y. Bobitski, and B. Kotlyarchuk, "Low-energy pulsed laser treatment of silver nanoparticles for interconnects fabrication by ink-jet method," *Microelectron. Eng.*, vol. 88, no. 3, pp. 318–321, Mar. 2011.

[48] J. Yeo *et al.*, "Next Generation Non-Vacuum, Maskless, Low Temperature Nanoparticle Ink Laser Digital Direct Metal Patterning for a Large Area Flexible Electronics," *PLoS One*, vol. 7, no. 8, p. e42315, Aug. 2012.

[49] K. Maekawa *et al.*, "Drop-on-demand laser sintering with silver nanoparticles for electronics packaging," *IEEE Trans. Components, Packag. Manuf. Technol.*, vol. 2, no. 5, pp. 868–877, 2012.

[50] K. A. Schroder, "Mechanisms of photonic curing™: Processing high temperature films on low temperature substrates," in *Technical Proceedings of the 2011 NSTI Nanotechnology Conference and Expo, NSTI-Nanotech 2011*, 2011, vol. 2, pp. 220–223.

[51] T. Falat, B. Platek, J. Felba, A. Mościcki, A. Smolarek, and K. Stojek, “Photonic sintering process of ink-jet printed conductive microstructures,” in *2012 4th Electronic System-Integration Technology Conference, ESTC 2012*, 2012.

[52] H.-J. Hwang, W.-H. Chung, and H.-S. Kim, “*In situ* monitoring of flash-light sintering of copper nanoparticle ink for printed electronics,” *Nanotechnology*, vol. 23, no. 48, p. 485205, Dec. 2012.

[53] Y. R. Jang, C. H. Ryu, Y. T. Hwang, and H. S. Kim, “Optimization of Intense Pulsed Light Sintering Considering Dimensions of Printed Cu Nano/Micro-paste Patterns for Printed Electronics,” *Int. J. Precis. Eng. Manuf. - Green Technol.*, pp. 1–15, Feb. 2020.

[54] M. Randall, *German, Sintering theory and practice*, vol. 8. 1996.

[55] H. Taheri, “Nondestructive evaluation and in-situ monitoring for metal additive manufacturing,” *Grad. Theses Diss.*, Jan. 2018.

[56] Y. Zeng, M. Edwards, R. Stevens, J. J. Bowen, R. S. Donnan, and B. Yang, “Terahertz characterisation of UV offset lithographically printed electronic-ink,” *Org. Electron.*, vol. 48, pp. 382–388, Sep. 2017.

[57] M. Zhuldybina, X. Ropagnol, C. Trudeau, M. Bolduc, R. Zednik, and F. Blanchard, “Contactless In Situ Electrical Characterization Method of Printed Electronic Devices with Terahertz Spectroscopy,” *Sensors*, vol. 19, no. 3, p. 444, Jan. 2019.

[58] M. Zenou, O. Ermak, A. Saar, and Z. Kotler, “Laser sintering of copper nanoparticles,” *J. Phys. D. Appl. Phys.*, vol. 47, no. 2, p. 025501, Jan. 2014.

[59] H. Malekpour and A. A. Balandin, “Raman-based technique for measuring thermal conductivity of graphene and related materials,” *J. Raman Spectrosc.*, vol. 49, no. 1, pp. 106–120, Jan. 2018.

[60] A. F. Goncharov and V. V. Struzhkin, “Raman spectroscopy of metals, high-temperature superconductors and related materials under high pressure,” *J. Raman Spectrosc.*, vol. 34, no. 7–8, pp. 532–548, Jul. 2003.

[61] M. Rahman, M. Shahzadeh, and S. Pisana, “Simultaneous measurement of anisotropic thermal conductivity and thermal boundary conductance of 2-dimensional materials,” *J.*

Appl. Phys., vol. 126, no. 20, p. 205103, Nov. 2019.

[62] D. Zhao, X. Qian, X. Gu, S. A. Jajja, and R. Yang, "Measurement techniques for thermal conductivity and interfacial thermal conductance of bulk and thin film materials," *J. Electron. Packag. Trans. ASME*, vol. 138, no. 4, Dec. 2016.

[63] M. Farzaneh *et al.*, "CCD-based thermoreflectance microscopy: Principles and applications," *J. Phys. D. Appl. Phys.*, 2009.

[64] Y. S. Kim *et al.*, "All-in-One, Wireless, Stretchable Hybrid Electronics for Smart, Connected, and Ambulatory Physiological Monitoring," *Adv. Sci.*, 2019.

[65] J. A. Rogers *et al.*, "Paper-like electronic displays: Large-area rubber-stamped plastic sheets of electronics and microencapsulated electrophoretic inks," *Proc. Natl. Acad. Sci. U. S. A.*, vol. 98, no. 9, pp. 4835–4840, Apr. 2001.

[66] D. J. Lipomi, B. C.-K. Tee, M. Vosgueritchian, and Z. Bao, "Stretchable Organic Solar Cells," *Adv. Mater.*, vol. 23, no. 15, pp. 1771–1775, Apr. 2011.

[67] M. Zirkl *et al.*, "Low-Voltage Organic Thin-Film Transistors with High-k Nanocomposite Gate Dielectrics for Flexible Electronics and Optothermal Sensors," *Adv. Mater.*, vol. 19, no. 17, pp. 2241–2245, Sep. 2007.

[68] J. Kim *et al.*, "Battery-free, stretchable optoelectronic systems for wireless optical characterization of the skin," *Sci. Adv.*, vol. 2, no. 8, Aug. 2016.

[69] T. Vervust, G. Buyle, F. Bossuyt, and J. Vanfleteren, "Integration of stretchable and washable electronic modules for smart textile applications," *J. Text. Inst.*, vol. 103, no. 10, pp. 1127–1138, Oct. 2012.

[70] D.-H. Kim, J. Xiao, J. Song, Y. Huang, and J. A. Rogers, "Stretchable, Curvilinear Electronics Based on Inorganic Materials," *Adv. Mater.*, vol. 22, no. 19, pp. 2108–2124, Jan. 2010.

[71] S. Xu *et al.*, "Assembly of micro/nanomaterials into complex, three-dimensional architectures by compressive buckling," *Science (80-.).*, vol. 347, no. 6218, pp. 154–159, Jan. 2015.

[72] S. Choi, S. I. Han, D. Kim, T. Hyeon, and D. H. Kim, "High-performance stretchable

conductive nanocomposites: Materials, processes, and device applications," *Chemical Society Reviews*, vol. 48, no. 6. Royal Society of Chemistry, pp. 1566–1595, 21-Mar-2019.

[73] Z. Wang, L. Zhang, S. Duan, H. Jiang, J. Shen, and C. Li, "Kirigami-patterned highly stretchable conductors from flexible carbon nanotube-embedded polymer films," *J. Mater. Chem. C*, vol. 5, no. 34, pp. 8714–8722, 2017.

[74] H. L. Filiatrault, R. S. Carmichael, R. A. Boutette, and T. B. Carmichael, "A Self-Assembled, Low-Cost, Microstructured Layer for Extremely Stretchable Gold Films," *ACS Appl. Mater. Interfaces*, vol. 7, no. 37, pp. 20745–20752, Sep. 2015.

[75] J. Lee *et al.*, "Ultra-Wideband Multi-Dye-Sensitized Upconverting Nanoparticles for Information Security Application," *Adv. Mater.*, vol. 29, no. 1, p. 1603169, Jan. 2017.

[76] J.-K. Song *et al.*, "Wearable Force Touch Sensor Array Using a Flexible and Transparent Electrode," *Adv. Funct. Mater.*, vol. 27, no. 6, p. 1605286, Feb. 2017.

[77] J. Song, H. Jiang, Y. Huang, and J. A. Rogers, "Mechanics of stretchable inorganic electronic materials," *J. Vac. Sci. Technol. A Vacuum, Surfaces, Film.*, vol. 27, no. 5, pp. 1107–1125, Sep. 2009.

[78] J. A. Rogers, T. Someya, and Y. Huang, "Materials and Mechanics for Stretchable Electronics," *Science (80-.).*, vol. 327, no. 5973, pp. 1603–1607, Mar. 2010.

[79] W. Dang, V. Vinciguerra, L. Lorenzelli, and R. Dahiya, "Printable stretchable interconnects," *Flexible and Printed Electronics*, vol. 2, no. 1. Institute of Physics Publishing, 01-Mar-2017.

[80] K. Noda, E. Iwase, K. Matsumoto, and I. Shimoyama, "Stretchable liquid tactile sensor for robot-joints," in *Proceedings - IEEE International Conference on Robotics and Automation*, 2010, pp. 4212–4217.

[81] N. Zhao, M. Yang, Q. Zhao, W. Gao, T. Xie, and H. Bai, "Superstretchable Nacre-Mimetic Graphene/Poly(vinyl alcohol) Composite Film Based on Interfacial Architectural Engineering," *ACS Nano*, vol. 11, no. 5, pp. 4777–4784, May 2017.

[82] Y.-Y. Lee *et al.*, "A Strain-Insensitive Stretchable Electronic Conductor:

PEDOT:PSS/Acrylamide Organogels," *Adv. Mater.*, vol. 28, no. 8, pp. 1636–1643, Feb. 2016.

[83] T. Sekitani, Y. Noguchi, K. Hata, T. Fukushima, T. Aida, and T. Someya, "A rubberlike stretchable active matrix using elastic conductors," *Science (80-.).*, 2008.

[84] Y. R. Jeong, H. Park, S. W. Jin, S. Y. Hong, S.-S. Lee, and J. S. Ha, "Highly Stretchable and Sensitive Strain Sensors Using Fragmentized Graphene Foam," *Adv. Funct. Mater.*, vol. 25, no. 27, pp. 4228–4236, Jul. 2015.

[85] Y. G. Seol, T. Q. Trung, O. J. Yoon, I. Y. Sohn, and N. E. Lee, "Nanocomposites of reduced graphene oxide nanosheets and conducting polymer for stretchable transparent conducting electrodes," *J. Mater. Chem.*, vol. 22, no. 45, pp. 23759–23766, Dec. 2012.

[86] J. Park *et al.*, "Electromechanical cardioplasty using a wrapped elasto-conductive epicardial mesh," *Sci. Transl. Med.*, vol. 8, no. 344, Jun. 2016.

[87] M. Shin, J. H. Song, G.-H. Lim, B. Lim, J.-J. Park, and U. Jeong, "Highly Stretchable Polymer Transistors Consisting Entirely of Stretchable Device Components," *Adv. Mater.*, vol. 26, no. 22, pp. 3706–3711, Jun. 2014.

[88] M. Park *et al.*, "Highly stretchable electric circuits from a composite material of silver nanoparticles and elastomeric fibres," *Nat. Nanotechnol.*, vol. 7, no. 12, pp. 803–809, 2012.

[89] A. Tabatabai, A. Fassler, C. Usiak, and C. Majidi, "Liquid-phase gallium-indium alloy electronics with microcontact printing," *Langmuir*, vol. 29, no. 20, pp. 6194–6200, May 2013.

[90] H. J. Kim, C. Son, and B. Ziaie, "A multiaxial stretchable interconnect using liquid-alloy-filled elastomeric microchannels," *Appl. Phys. Lett.*, vol. 92, no. 1, 2008.

[91] Y. Yoon, S. Kim, D. Kim, S. K. Kauh, and J. Lee, "Four Degrees-of-Freedom Direct Writing of Liquid Metal Patterns on Uneven Surfaces," *Adv. Mater. Technol.*, vol. 4, no. 2, p. 1800379, Feb. 2019.

[92] Y. G. Park, H. S. An, J. Y. Kim, and J. U. Park, "High-resolution, reconfigurable printing of liquid metals with three-dimensional structures," *Sci. Adv.*, vol. 5, no. 6, p. eaaw2844,

Jun. 2019.

[93] A. Cook *et al.*, “Shear-Driven Direct-Write Printing of Room-Temperature Gallium-Based Liquid Metal Alloys,” *Adv. Eng. Mater.*, vol. 21, no. 11, p. 1900400, Nov. 2019.

[94] L. Zhou, J. Fu, Q. Gao, P. Zhao, and Y. He, “All-Printed Flexible and Stretchable Electronics with Pressing or Freezing Activatable Liquid-Metal–Silicone Inks,” *Adv. Funct. Mater.*, vol. 30, no. 3, p. 1906683, Jan. 2020.

[95] A. Albrecht *et al.*, “Over-stretching tolerant conductors on rubber films by inkjet-printing silver nanoparticles for wearables,” *Polymers (Basel).*, vol. 10, no. 12, 2018.

[96] J. Lee, S. Chung, H. Song, S. Kim, and Y. Hong, “Lateral-crack-free, buckled, inkjet-printed silver electrodes on highly pre-stretched elastomeric substrates,” *J. Phys. D. Appl. Phys.*, vol. 46, no. 10, p. 105305, Mar. 2013.

[97] D. J. Finn, M. Lotya, and J. N. Coleman, “Inkjet printing of silver nanowire networks,” *ACS Appl. Mater. Interfaces*, vol. 7, no. 17, pp. 9254–9261, May 2015.

[98] Q. Huang, K. N. Al-Milaji, and H. Zhao, “Inkjet Printing of Silver Nanowires for Stretchable Heaters,” *ACS Appl. Nano Mater.*, vol. 1, no. 9, pp. 4528–4536, Sep. 2018.

[99] R. P. Gandhiraman, V. Jayan, J.-W. Han, B. Chen, J. E. Koehne, and M. Meyyappan, “Plasma Jet Printing of Electronic Materials on Flexible and Nonconformal Objects,” *ACS Appl. Mater. Interfaces*, vol. 6, no. 23, pp. 20860–20867, Dec. 2014.

[100] T. Sekitani *et al.*, “Stretchable active-matrix organic light-emitting diode display using printable elastic conductors,” *Nat. Mater.*, vol. 8, no. 6, pp. 494–499, 2009.

[101] E. B. Secor, S. Lim, H. Zhang, C. D. Frisbie, L. F. Francis, and M. C. Hersam, “Gravure Printing of Graphene for Large-area Flexible Electronics,” *Adv. Mater.*, vol. 26, no. 26, pp. 4533–4538, Jul. 2014.

[102] M. S. Lee *et al.*, “High-performance, transparent, and stretchable electrodes using graphene-metal nanowire hybrid structures,” *Nano Lett.*, vol. 13, no. 6, pp. 2814–2821, 2013.

[103] M. Tavakoli *et al.*, “EGaIn-Assisted Room-Temperature Sintering of Silver Nanoparticles for Stretchable, Inkjet-Printed, Thin-Film Electronics,” *Adv. Mater.*, vol. 30, no. 29, Jul.

2018.

[104] J. P. Feser and D. G. Cahill, “Probing anisotropic heat transport using time-domain thermoreflectance with offset laser spots,” in *Review of Scientific Instruments*, 2012.

[105] J. V. Alemán *et al.*, “Definitions of terms relating to the structure and processing of sols, gels, networks, and inorganic-organic hybrid materials (IUPAC Recommendations 2007),” *Pure Appl. Chem.*, vol. 79, no. 10, pp. 1801–1829, Jan. 2007.

[106] F. Meng and J. Huang, “Evolution mechanism of photonically sintered nano-silver conductive patterns,” *Nanomaterials*, vol. 9, no. 2, Feb. 2019.

[107] H. K. Lee, S. Il Chang, and E. Yoon, “A flexible polymer tactile sensor: Fabrication and modular expandability for large area deployment,” *J. Microelectromechanical Syst.*, vol. 15, no. 6, pp. 1681–1686, Dec. 2006.

[108] D. S. Gray, J. Tien, and C. S. Chen, “High-Conductivity Elastomeric Electronics,” *Adv. Mater.*, vol. 16, no. 5, pp. 393–397, Mar. 2004.

[109] D. Birchfield, X. Jackson, T. Pasternak, A. Hanson, and M. Atashbar, “Strain Sensor Fabrication by Means of Laser Carbonization,” in *FLEPS 2019 - IEEE International Conference on Flexible and Printable Sensors and Systems, Proceedings*, 2019.

[110] A. Chhetry, M. Sharifuzzaman, H. Yoon, S. Sharma, X. Xuan, and J. Y. Park, “MoS2-Decorated Laser-Induced Graphene for a Highly Sensitive, Hysteresis-free, and Reliable Piezoresistive Strain Sensor,” *ACS Appl. Mater. Interfaces*, 2019.

[111] D. Brosteaux, F. Axisa, M. Gonzalez, and J. Vanfleteren, “Design and fabrication of elastic interconnections for stretchable electronic circuits,” *IEEE Electron Device Lett.*, 2007.

[112] M. S. Rahman and G. Grau, “Direct writing of stretchable metal flake conductors: improved stretchability and conductivity by combining differently sintered materials,” *Flex. Print. Electron.*, Apr. 2020.